CONTROLLED FORMATION OF OIL-FREE SOFT BIOMATERIALS USING ALL-AQUEOUS FLUID SYSTEMS

by

Morteza Jeyhani

Master of Applied Science in Mechanical Engineering, Concordia University, Canada 2014

Bachelor of Science in Mechanical Engineering, Azad University, Iran, 2011

A dissertation

presented to Ryerson University

in partial fulfillment of the

requirements for the degree of

Doctor of Philosophy

in the program of

Mechanical and Industrial Engineering

Toronto, Ontario, Canada, 2020

AUTHOR'S DECLARATION FOR ELECTRONIC SUBMISSION OF A DISSERTATION

I hereby declare that I am the sole author of this dissertation. This is a true copy of the dissertation, including any required final revisions, as accepted by my examiners.

I authorize Ryerson University to lend this dissertation to other institutions or individuals for the purpose of scholarly research.

I further authorize Ryerson University to reproduce this dissertation by photocopying or by other means, in total or in part, at the request of other institutions or individuals for the purpose of scholarly research.

I understand that my dissertation may be made electronically available to the public.

Controlled Formation of Oil-Free Soft Biomaterials Using All-Aqueous Fluid Systems

Doctor of Philosophy, 2020
Morteza Jeyhani
Mechanical and Industrial Engineering
Ryerson University

Abstract

In this dissertation, I developed microfabrication techniques to produce oil-free soft materials using all-aqueous fluid systems, for biological and biomedical applications. To generate soft-materials in conventional platforms, typically, organic solvents are used, which are not compatible with biological environments and thus require extensive washing steps to remove the toxic phase.

I first demonstrated a technique to fabricate non-spherical hydrogels based on electrohydrodynamic atomization. In this study, I investigated the effect of experimental parameter changes on the morphology of the fabricated particles. Moreover, carboxylated magnetic beads were used to functionalize the particles while the particle shape is preserved. These particles can be used for magnetic separation schemes. I used breast cancer cells (BT-474) to examine the potential of these particles for cell encapsulation.

Aqueous-two phase systems (ATPS) are used as an organic solvent free two-phase system to generate single, double, and triple emulsions. However, most ATPSs have very low interfacial tensions, so conventional microfluidic methods cannot fabricate ATPS emulsions with a reasonable throughput, and in most cases, an external component to perturb the flow is needed to induce droplet formation. In the second half of this dissertation, I have designed and fabricated lithography-based microfluidic devices in which micro-conduits are embedded coaxially inside

the microchannel to isolate the disperse phases from the channel walls, thereby circumventing the surface wetting problems that prevent successful droplet formation. This method benefits from the flexibility of choosing the disperse and continuous phases independently and permits the switching of the phase order to facilitate the formation of aqueous emulsions, regardless of their physical properties such as hydrophobicity. The configuration of this microfluidics platform also enables the focusing of two or three concentric threads of ATPS without channel-wetting problems. This approach facilitates the fabrication of higher order emulsions using already phase separated ATPS in a polydimethylsiloxane (PDMS)-based microfluidic device.

Acknowledgments

Firstly, I would like to express my sincere gratitude to Prof. Scott S.H. Tsai, Department of Mechanical and Industrial Engineering, and Prof. Dae Kun Hwang, Department of Chemical Engineering, Ryerson University, Toronto, Ontario, Canada, my research supervisors, for their patient guidance, enthusiastic encouragement, immense knowledge and useful critiques of this research work.

My sincere thanks to my examining committee chair Prof. Ahmad Ghasempoor, Department of Mechanical and Industrial Engineering, and Prof. Andrew Laursen, Department of Chemistry and Biology, Ryerson University, Toronto, Ontario, Canada and members Profs. Daolun Chen and Ziad Saghir, Department of Mechanical and Industrial Engineering, Ryerson University, Toronto, Ontario, Canada, Prof. Dérick Rousseau, Department of Chemistry and Biology, Ryerson University, Toronto, Ontario, Canada, and Prof. Shuichi Takayama, Wallace H. Coulter Department of Biomedical Engineering, Georgia Institute of Technology, Atlanta, Georgia, USA.

I would like to express my very great appreciation to all the former and present members of the Laboratory of Fields, Flows, and Interfaces and Advanced Materials Research Group. Assistance provided by Dr. Daniel Foster was greatly appreciated. I would like to offer my special thanks to Prof. Michel Labrosse, Department of Mechanical Engineering at the University of Ottawa for all his help and support prior to joining Ryerson University.

Finally, I wish to thank my parents for their support and encouragement throughout my study.

Dedication

This dissertation is dedicated to my wonderful wife Nava, whose unyielding love, support, and encouragement has enriched my soul and inspired me to pursue and complete this research.

Table of Contents

Abstract iii
Acknowledgments v
Dedication vi
List of Tables x
List of Figures xi
Chapter 1: Introduction 1
1.1 Motivation 1
1.2 Background 3
1.2.1 Oil-free two-phase systems 3
1.2.2 Electrohydrodynamic atomization 7
1.2.3 Microfluidics 10
1.3 Objectives and hypothesis 12
1.4 Author's contribution in the context of collaboration 13
Chapter 2: Non-spherical microparticles 15
2.1 Introduction 16
2.2 Experimental methods 18
2.2.1 Chemicals and cells 18
2.2.2 Experimental setup 19
2.3 Results and discussion 20
2.3.1 Controlling the particles' morphology 20
2.3.2 Controlling the aspect ratio of hemispherical microparticles 21
2.3.3 Generating microparticles with curved tails 23
2.3.4 Generating non-spherical magnetizable microparticles 25
2.3.5 Cell encapsulation 26
2.4 Conclusions 26
Chapter 3: All-aqueous single emulsions 28
3.1 Introduction 29
3.2 Experimental methods 31
3.2.1 Chemicals 31

3.2.2 Experimental Setup 32
3.2.3 Device Fabrication 33
3.3 Results and discussion 34
3.3.1 Droplet generation regimes 34
3.3.2 Droplet generation diameters 37
3.3.3 Droplet generation throughput 39
3.3.4 Generating PEG-in-DEX droplets 42
3.4 Conclusions 43
Chapter 4: All-aqueous double and triple emulsions 44
4.1 Introduction 45
4.2 Experimental methods 48
4.2.1 Chemical preparation 48
4.2.2 Device Fabrication 50
4.2.3 Microfluidic setup 52
4.2.4 Preparation of lysozyme 53
4.3 Results and discussion 54
4.3.1 Formation of double emulsions 54
4.3.2 Controlling the shell thickness 57
4.3.3 Controlling the distance between double emulsions 58
4.3.4 Formation of triple emulsions 60
4.3.5 Shrinking and expanding emulsions 61
4.4 Conclusions 63
Chapter 5: Conclusions and future work 64
5.1 Summary of findings 64
5.2 Contributions 65
5.3 Future work 66
Appendix I: Supplementary information for Chapter 2 68
Appendix II: Supplementary information for Chapter 3 73
Appendix III: Supplementary information for Chapter 4 78
Appendix IV: Error analysis 84
Bibliography 85

List of Tables

Table 3.1: List of microfluidics and glass capillary-based techniques developed for generating ATPS droplets, along with their performance parameters. 40

Table 4.1: Concentration of stock solutions and equilibrated PEG-rich and DEX-rich phases..... 49

Table 4.2: Physical properties of three different ATPSs are used in the experiments. 49

List of Figures

Figure 1.1: Plot showing the increase in the number of publications used the keywords “hydrogel”, “droplet”, and “ATPS” since 1950. 2

Figure 1.2: A phase diagram for ATPS with PEG (M_w: 35 kDa) and DEX (M_w: 500 kDa). Selecting initial compositions below the binodal curve leads to a mixture of both phases into a single phase, while the selection of the initial composition above the binodal curve forms a biphasic system [38]. 5

Figure 1.3: Under the effect of a strong electric field, liquid at the positive electrode gains a net positive charge, where the positive ions collect at the apex of the generated cone. The electrostatic repulsion causes the excess surface charge to overcome the surface tension of the liquid, which leads to the generation of a monodisperse spray of positively charged droplets, which accelerate towards the cathode [59]. 8

Figure 1.4: The equilibrium of the electrostatic and surface tension pressures results in the formation of the Taylor cone, with a whole angle of 99º. The apex of the cone experiences the highest intensity of the electric field [60]..... 9

Figure 1.5: Increase in the voltage causes the meniscus to deform to a conical shape, and charged droplets start to form from the jet of liquid [8]. 10

Figure 1.6: Schematic of flow-focusing microfluidic devices under three different regimes [75]. 11

Figure 2.1: Schematic diagram of the electrospray system for alginate particle generation. A high-voltage power supply with low current is used to generate the electric field. The positively charged droplet phase is electrosprayed into a calcium chloride bath through a tapered glass capillary, to generate particles. The distance between the tip of the glass capillary and the ring is fixed at 1 mm. We adjust the distance between the ring and the free-surface of the calcium chloride bath, L_b, to observe its effects on the resulting particle shapes. 19

Figure 2.2: Particle shape controlled by electrospray properties. a) *Tadpole*-like microparticles are generated when the ring-to-bath distance L_b = 3 mm and the calcium chloride concentration C = 1 wt%. b-d) In all other cases in our experiments, where the calcium chloride concentration $C \leq 2.5$ wt%, we obtain *cupcake*-like particles. e-j) *Hemispherical* shaped particles are produced when the calcium chloride concentration $C \geq 5$ wt%. In all of these experiments, the voltage of the electrospray, and the flow rate of the pump are fixed at 5 kV and 0.1 mL/hr, respectively. Scale bar represents 150 μm. Illustrations that more clearly show what we define as k) *tadpole*-like, l) *cupcake*-like, and m) *hemispherical* shape microparticles. 20

Figure 2.3: Different types of alginate microparticles. A phase diagram of the generated calcium-alginate particles illustrates differences in particle shape as a result of changing the calcium chloride concentration C, and the ring-to-

bath distance L_b. We find that the electrospray setup generates hemispherical particles as long as calcium chloride concentrations $C \geq 5$ wt%. When calcium chloride concentration $C < 5$ wt%, we observe tadpole-like particles or cupcake-like particles. 21

Figure 2.4: Hemispherical particle aspect ratio $\Omega = h/b$ controlled by the liquid bath calcium chloride concentration C and the ring-to-bath distance L_b. a) Ω is defined as the ratio between the height h of the hemisphere and its base length b. b) A plot of the resulting hemispherical particle aspect ratio Ω versus the calcium chloride concentration C. Different symbols represents distinct values of the ring-to-bath distance L_b. Increasing the ring-to-bath distance L_b for a particular calcium chloride concentration C results in a nearly monotonic decrease in particle aspect ratio Ω. Increasing the calcium chloride concentration C, while fixing the ring-to-bath distance L_b also results in a nearly monotonic decrease in Ω. Error bars indicate one standard deviation in a sample size of 20 particles (Appendix IV). 23

Figure 2.5: The effect of stirring the liquid bath. We use a magnetic stirrer to create a flow in the liquid bath. Here, the ring-to-bath distance $L_b = 10$ mm, and calcium chloride concentration $C = 10$ wt%. As the magnetic stirrer rotation rate increases from a) 50, b) 250, to c) 500 rpm, the curvature of the resulting particle increases. Scale bar represents 150 μm..... 24

Figure 2.6: Magnetic particles. Fabrication of magnetic microparticles using magnetic beads. The ring-to-bath distance is fixed at $L_b = 20$ mm, and two different calcium chloride concentrations a) $C = 5$ and b) $C = 10$ wt% are used, resulting in different particle aspect ratios Ω. c) A sequence of images showing that an external magnetic field from a moving permanent magnet causes a particle to rotate. Scale bar represents 150 μm..... 25

Figure 2.7: Cell encapsulation. BT-474 breast cancer cells encapsulated in hemispherical microparticles using our electrospray technique. Here, the ring-to-bath distance is fixed at $L_b = 20$ mm, and we use two different calcium chloride concentrations, a) $C = 5$ and b) $C = 7.5$ wt%. Scale bar represents 150 μm. 26

Figure 3.1: (a) Schematic diagram of the experimental setup for a passive ATPS droplet formation. Two plastic syringe tubes filled with each respective phase are connected to the microfluidic chip through the tubing. An adjustable lab jack is used to adjust the effective column heights of the phases to adjust the hydrostatic pressures. (b) Representative schematic diagram of the microfluidic chip. A microneedle is inserted as the inlet of the disperse phase inside the microfluidic chip. The microneedle is accurately located at the center of the channel to leave gaps between the channel walls and the needle, enabling 3D focusing of the disperse phase to the center of the channel. (c & d) Images of the needle device and the needleless device, respectively. 32

Figure 3.2: Experimental images of water-in-water droplet generation using the passive microfluidic platform and comparison between the device with an inserted needle (W/N) and the device without the needle (W/O N), with different, disperse and continuous column heights, P_D and P_P, respectively. (a-e) In the W/N device, a broad range of hydrostatic column heights can be used for generating droplets, due to the 3D flow focusing of the dispersed phase.

(f-j) The same hydrostatic column heights with the W/O N device results in four different regimes of (g) backflow, (h) droplets, (i) ripple-shaped thread, and (j) continuous thread along the channel. Scale bar represents 100 µm. 34

Figure 3.3: Phase diagram for flow regimes in the device W/N and the device W/O N. (a) The W/N device either results in droplet formation, or backflow, and no other regimes are observed in the ranges of hydrostatic heights used. (b) In the device W/O N, we observe four regimes: backflow, droplet formation, ripple-shaped threads, and continuous threads. 35

Figure 3.4: The diameter of droplets formed versus the DEX liquid column pressure, P_D, for three different PEG liquid column pressures, P_P, inside the device W/N. Diamond markers (♦) represent data points for P_P = 2.0 kPa, triangle markers (▲) show data points for P_P = 2.8 kPa, and squares (■) represent data points for P_P = 3.6 kPa. For all three data series, increasing P_D, while fixing P_P, results in the formation of larger droplets. The data points with an asterisk (*) denotes the threshold of the droplet regime for the particular data series, below which backflow occurs. Error bars indicate one standard deviation in a sample size of 30 droplets. 37

Figure 3.5: Log-log plot of dimensionless droplet diameter *a/h* vs the ratio of DEX and PEG inlet conditions. Our data appears to fit reasonably onto the line indicated by $ah = 4PD\mu D/PP\mu P2$..... 38

Figure 3.6: Droplet fabrication rate versus the DEX pressures (P_D) for three different PEG pressures (P_P) inside the device W/N. Diamond markers (♦) represent data points for P_P = 2.0 kPa, triangle markers (▲) shows data points for P_P = 2.8 kPa, and squares (■) indicate data points for P_P = 3.6 kPa. Elevating the column pressure of the dispersed phase flow (DEX), decreases the throughput of droplets for all three PEG heights. Data points with an asterisk (*) denote the threshold of droplet regime for the corresponding data series. 39

Figure 3.7: Experimental images of the microfluidic cross junction in devices (a-c) with the needle (W/N) and (d-f) without needle (W/O N), where a dispersed PEG phase flows in the continuous DEX phase. The dispersed PEG phase forms droplets in the device W/N, but not in the device W/O N, at the same hydrostatic pressures. (g) A schematic cross-sectional view of the device W/N, where the green colour indicates the disperse PEG phase, and the gray colour represents the continuous DEX phase inside the microfluidic channel. The presence of the microneedle causes the dispersed PEG phase to be isolated from the channel walls. (h) The schematic cross-sectional view for the device W/O N, illustrating that the dispersed PEG phase tends to wet the top and bottom walls, which is also evident from the confocal microscopy inset image. Here, the confocal image shows the bottom one-third of the channel height because the confocality of the confocal microscope is 80-100 µm. Scale bars represent 100 µm..... 41

Figure 4.1**:** a) Schematic diagram of the hybrid device, composed of a microneedle in the first inlet and an embedded glass capillary inside the microchannel between the first and second cross-junction, for double emulsions formation. b) First cross-junction in which the inner DEX phase flows through the microneedle and the middle PEG phase flows through the glass capillary. c) The two concentric phases arrive at the second cross-junction from the glass capillary. The outer DEX phase causes the ATPS jet to breakup to double emulsions via a Rayleigh–Plateau instability. d)

Double emulsions form inside the microchannel. e) Emulsions collet in a reservoir downstream the channel. The scale bar represents 300 μm. 50

Figure 4.2: a) Schematic diagram of the hybrid device for producing double emulsions. The inner DEX phase is introduced via the microneedle, and meets the middle PEG phase at the first junction. The co-flowing phases flow into the glass capillary as a thread. The outer DEX phase is introduced at the second cross-junction. Here, the thread formed by co-flowing inner DEX and middle PEG phases breakup into emulsions due to the Rayleigh-Plateau instability. b-f) Experimental images of double emulsion formation in different locations inside the microchannel. g) A phase diagram illustrates the pressure ranges, indicated with solid bars, in which double emulsions form. Here, the constant pressure ratio $P_{PEG\ Mid}$ / $P_{DEX\ In}$ = 12. Higher values of $P_{DEX\ Out}$, above the solid bars, lead to backflow, and lower values result in double emulsions that have two or more droplets encapsulated in a bigger droplet. Further decreases in $P_{DEX\ Out}$ lead to the formation of long threads. h) A plot of inner droplet diameter D_i, outer diameter D_o, and shell thickness t, versus the outer DEX phase pressure, $P_{DEX\ Out}$. Here, inner DEX and middle PEG pressures are $P_{DEX\ In}$ = 20 mbar and $P_{PEG\ Mid}$ = 10 mbar, respectively. All error bars corresponded to ±1 standard deviations in a sample size of ten emulsions (some statistical errors are smaller than the symbol size). See Table III.1, Appendix III for statistical analysis. Scale bar represents 150 μm..... 54

Figure 4.3: Inner and outer droplet diameters, D_i, and D_o, respectively, and shell thickness, t, versus the inner DEX phase pressure, $P_{DEX\ In}$. Here, the outer DEX phase pressure follows a half-wave rectified sinusoidal waveform with amplitude, P_{Max} = 300 mbar and period T = 500 ms. All error bars corresponded to ±1 standard deviations in a sample size of ten emulsions (some statistical errors are smaller than the symbol size). See Table III.2, Appendix III for statistical analysis. 57

Figure 4.4: a) Plot of inner and outer droplet diameter, D_i and D_o, and coefficients of variation of the inner and outer droplet diameters, CV_i and CV_o, versus the period T. Here, inner DEX and middle PEG pressures $P_{DEX\ In}$ = 25 mbar and $P_{PEG\ Mid}$ = 10 mbar, respectively; and the outer DEX phase pressure, $P_{DEX\ Out}$, follows a half-wave rectified sinusoidal waveform with amplitude, P_{Max} = 300 mbar and a range of periods, T = 0.3 – 1.3 seconds. b) Changes of inter-droplet distance, d, versus a range of periods. c-f) Experimental images illustrating the increase of the inter-droplet distance for T = 0.3, 0.6, 0.9, and 1.2 seconds. All error bars corresponded to ±1 standard deviations in a sample size of ten emulsions (some statistical errors are smaller than the symbol size). See Tables III.3 and III.4, Appendix III for statistical analysis. Scale bar represents 150 μm. 58

Figure 4.5: a) Schematic diagram of the hybrid device for generating triple emulsions. The inner DEX phase is introduced through the microneedle, and meets the middle PEG phase at the first junction. Then both phases flow into the first glass capillary as a thread. The middle DEX phase is introduced at the second cross-junction, where the inner DEX and middle PEG phases flow into the second glass capillary as a thread. The outer PEG phase is introduced at the third cross-junction. Here, the thread formed by co-flowing inner DEX phase, middle PEG phase, and middle DEX phase breaks up into triple emulsions due to the Rayleigh-Plateau instability. b-c) Experimental images of triple emulsions formed in different locations, for two different inlet pressure conditions. Scale bar represents 300 μm... 60

Figure 4.6: Shrinking and expanding the volume of double emulsions. a) Schematic of the hybrid device shown from the third cross-junction. Introducing a higher concentration phase, DEX 2, as the outer DEX phase triggers a non-equilibrium which ultimately, results in water transfer from the PEG phase to its surrounding phase. b) Time-series images of a double-emulsion flowing downstream in the channel and shrinking with time. c) Schematic of the setup for expanding the volume of the double emulsion. Introducing a lower concentration of the outer DEX phase, DEX 3, leads to a water exchange between the PEG phase and the surrounding DEX phase and ultimately results in water transfer from the continuous phase to the PEG phase. d) Time-series of images of a double emulsion growing downstream in the channel. Scale bars represent 150 μm..... 61

Chapter 1: Introduction

1.1 Motivation

Scientists have extensively investigated, both in theory and experiments, the fabrication of soft biomaterials such as particles, hydrogels, and emulsions. Over the past decades, with the growth of interdisciplinary fields of research, such as biotechnology development, the demand for soft biomaterials technology has increased. In biotechnology, soft biomaterials have been used for a broad range of applications such as tissue engineering [1], [2], cell encapsulation [3], cell transplantation and immune protection [4], single-cell analysis [5], and delivery systems [6], [7].

The importance of these biomaterials can be understood by examining a historical count of articles on the topic. Figure 1.1 shows the results of searching the words “hydrogel” and “droplet” on Scopus. There has been an exponential increase in the number of articles investigating such biomaterials. In this figure, the number of articles published on the topic of aqueous two-phase systems (ATPS) since 1950, is shown as well. This data demonstrates the interest in such materials by the scientific community.

Soft biomaterials provide unique features that in turn make them suitable for delivery applications. For instance, their small-scale nature has enabled higher efficacy drug delivery with greater stability, solubility, and the administration of lower drug doses [8]. The monodispersity—uniformity in size—of these carriers can be advantageous toward the prediction of drug release time in the pharmaceutical industry [8]. These carriers can be functionalized to control drug release by triggering disruption of the capsule vehicle using various remote stimuli such as temperature, pH, magnetization [9]–[12], optics [13]–[18], and ultrasound [19] for delivery.

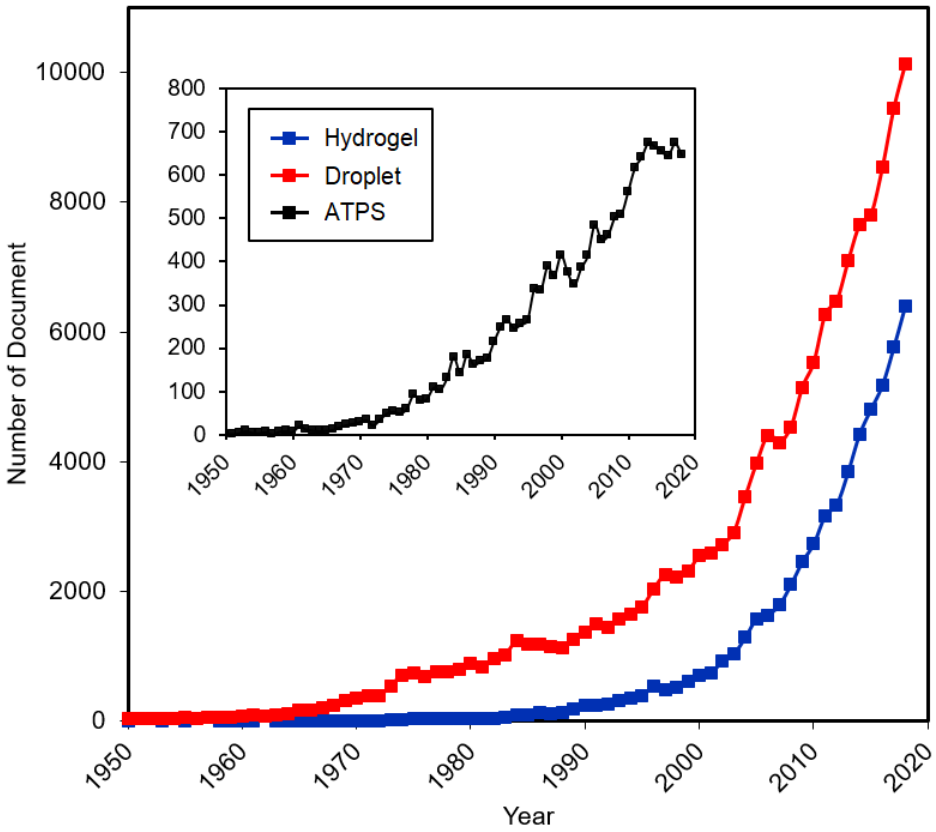

Figure 1.1: Plot showing the increase in the number of publications used the keywords "hydrogel", "droplet", and "ATPS" since 1950.

However, the application of these techniques is relatively expensive and complicated, imposing barriers for their commercialization. The development of these advanced methods has improved the function of drug vehicles, but there are still more improvements to be made.

Recent studies of drug delivery particles emphasize how their morphology dictates the release mechanism in drug delivery [20], [21]. Morphological changes affect the delivery mechanism inside the body. Moreover, particle morphology can affect the particles' transportation and circulation throughout the body [22], [23]; for example, non-spherical particles exhibit better delivery dynamics in the body compared to spherical particles [20]. Lastly, it has been shown that morphology impacts drug release pharmacokinetics [24], and the targeting ability of drug-carrying particles [20]. These properties are all vital factors that impact the efficacy of drug delivery.

In order to use hydrogels and emulsions in biological applications, all the solutions need to be low toxicity and biocompatible, and biodegradable. Existing techniques are coupled with at least one biologically-incompatible agent that requires additional steps to reduce its harmful effects. For

emulsions in particular, one of the phases is selected to be oil to increase the interfacial tension between the phases and induce droplet breakup. Since most oil phases are not biocompatible, the oil phases must be removed before *in vivo* use. To achieve complete removal of oil from the system, it requires post-processing washing steps [25] which are labour intensive and time-consuming [26].

For these reasons, using biocompatible and biodegradable materials for drug delivery systems can be beneficial to the pharmaceutical industry. This could also reduce the required time to obtain approval from health authorities such as Health Canada and the U.S. Food and Drug Administration (FDA) in both pre-clinical and clinical stages.

In addition to improving the functionality and efficacy of drug vehicles, the affordability of existing techniques for mass production also needs to be considered. The low throughput of many developed techniques prevents their transition to a clinical setting. Improving the production rate of these techniques would help to implement them more efficiently.

The research presented in this dissertation demonstrates novel techniques for generating oil-free particles using all-aqueous systems with improved throughput. Since these hydrogels and emulsions are oil-free and generated using all-aqueous systems, they may be able to address biomedicine and biological needs, such as those in drug delivery applications, single-cell encapsulation and analysis, immunoisolating cells for cellular transplantation, and three-dimensionally (3D) cell culture.

1.2 Background

In this section, some basic theoretical concepts of the tools and techniques used in this research are introduced.

1.2.1 Oil-free two-phase systems

Soft biomaterials can be defined as a mixture of two phases that are typically immiscible. Emulsions are colloids with a stable suspension of one immiscible liquid in the form of droplets within another. The fluid forming the emulsions is known as the dispersed phase. The fluid containing this dispersed phase is known as the continuous phase. A classic example of one such system is a mixture of vinegar and olive oil. The same concept is used for the fabrication of soft

biomaterials whether they are hydrogels or droplets. Traditionally, in order to control the particle fabrication process, an oil-based phase along with an aqueous-based phase are used because of their high interfacial tension.

In biomedical investigations, the use of oil or surfactant may lead to cytocompatibility issues and compromise the viability of the biological cargo [27]. In addition to the biocompatibility issues that arise from using an oil phase in droplet microfluidics, the use of oil may hinder the size reduction of the droplets due to the high interfacial tension between the oil and aqueous phases [28], [29]. In order to reduce the interfacial tension, in conventional systems, a powerful surfactant is required in the system that may have a negative effect on the biological materials. For biological applications, circumventing problems linked to the presence of oil requires a cumbersome washing step to complete oil removal [30]. These washing steps are highly time- and labour-consuming [26].

ATPSs are biologically acceptable alternatives for traditional oil-water biphasic systems. ATPS was accidentally discovered by Martinus Willem Beijerinck in 1896 while he was working with a mixture of agar and starch or gelatine [31], and later Per-Åke Albertsson investigated its applications in biotechnology [32], [33]. These systems are composed of a mixture of two incompatible polymers, or a polymer and a salt, mixed in an aqueous medium that spontaneously phase separates into two phases [34]. ATPSs have a complex nature of molecular interactions that make each system relatively unique [35]. To characterize each ATPS individually, a phase diagram is required. A sample phase diagram of ATPS with poly(ethylene) glycol (PEG) and dextran (DEX) is presented in Figure 1.2. The binodal curve divides the plot into two regions: polymer concentrations below the binodal curve result in a single liquid phase, and concentrations above the binodal curve results in phase separation.

Phase separation in polymer-polymer aqueous systems is a very common but sophisticated phenomenon that is dependant on various parameters and characteristics of the system. The main reason that phase separation is a spontaneous phenomenon is due to the high molecular weight of the polymers and their resulting low entropy of mixing [36]. This means that if the interaction between different polymer segments is repulsive and energetically unfavourable, then phase separation occurs [37].

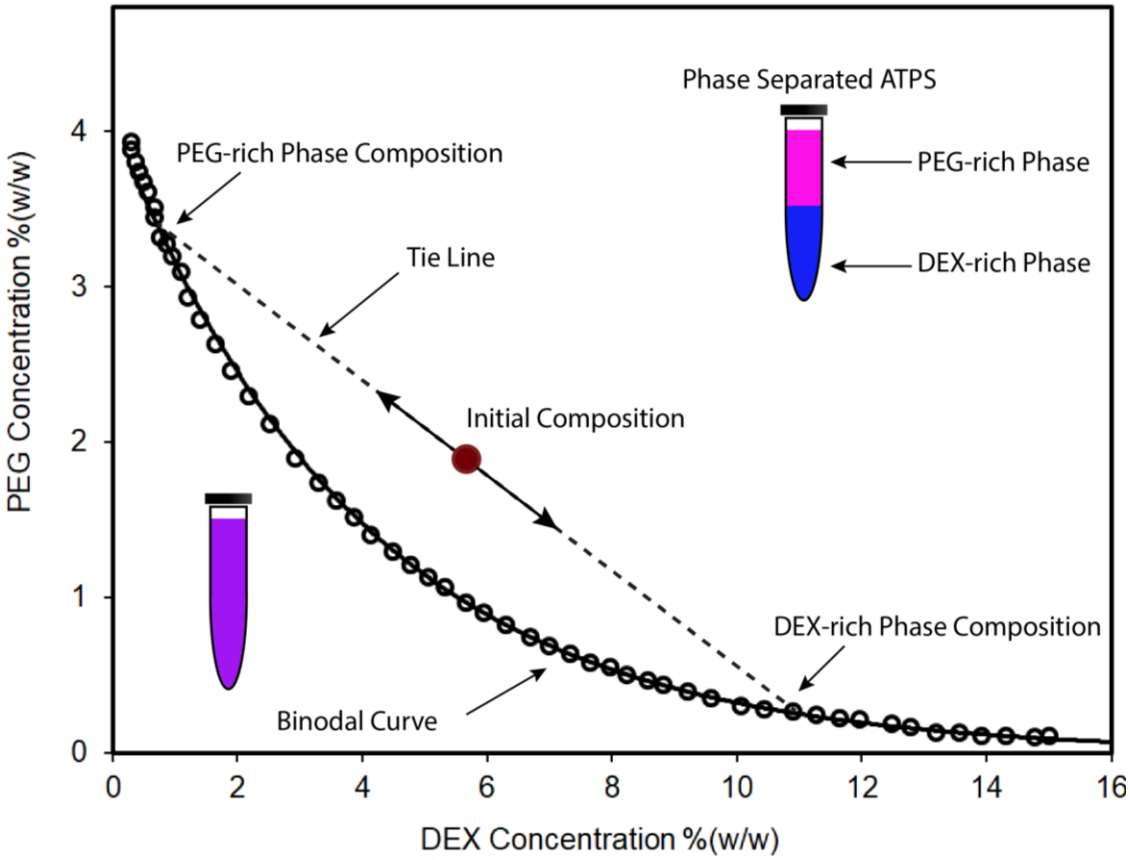

Figure 1.2: A phase diagram for ATPS with PEG (M_w: 35 kDa) and DEX (M_w: 500 kDa). Selecting initial compositions below the binodal curve leads to a mixture of both phases into a single phase, while the selection of the initial composition above the binodal curve forms a biphasic system [38].

Upon the mixing of the polymers at sufficiently high concentrations, one phase separates into the disperse phase, and the other phase separates into the continuous phase. In general, the dispersed droplets experience three forces, and the balance between these forces determine the movement of the aforementioned droplets [39]. These three forces are gravitational, flotational, and frictional, in which the gravitational component scales with the disperse phase density, the frictional part is a function of the continuous phase viscosity, and always impedes drop movement, while the flotational component depends on flow properties [40]. These three forces, combined with interfacial tension, determine the coalescence of the disperse phase [41] and lead to phase separation.

Albertsson suggested a model consisting of six different factors in the logarithmic term that each has a different effect on the partitioning [32], as follow:

$$\text{Ln } K = \text{Ln } K_{elec} + \text{Ln } K_{hfob} + \text{Ln } K_{affinity} + \text{Ln } K_{size} + \text{Ln } K_{conf} + \text{Ln } K^0 \qquad (1.1)$$

Wherein K_{elec}, represents electrostatic effects; K_{hfob}, denotes hydrophobic partitioning term; $K_{affinity}$, stands for affinity interaction in the system; K_{size}, denotes proteins and polymer size; K_{conf}, represents molecules' conformational effects; and K^0 considers other factors that may influence phase separation and partitioning in ATPS [42].

Partitioning and phase separation in ATPS should ideally be based on chemical interactions of the system's components [42] and this process, thermodynamically, is explained by Boltzmann equation [43]:

$$K = e^{-\frac{\Delta E}{kT}} \tag{1.2}$$

where K represents the partition coefficient, $k = 1.381\times10^{-27}$ [J/K] is Boltzmann's constant, T [K] is absolute temperature, and ΔE [J] is the energy needed to move molecules to another state that is determined by the surface free energy between solutions.

To calculate the free energy to determine ΔE [J], Flory-Huggins theory can be used:

$$\Delta G = \Delta H - \mathrm{T}\Delta S \tag{1.3}$$

where ΔG [J] is the change in the free energy, ΔH [J] is the change in enthalpy, and $T\Delta S$ [KJ/K] is the change in entropy.

In general, the maximal phase separation occurs for higher values of the partition coefficient, K. As mentioned, there are different factors influencing the phase separation including physical conditions of ATPS such as temperature. In order to understand the effect of temperature on ATPS phase separation quantitatively, based on Boltzmann equation, increasing the temperature leads to an increase in the value of K, which results in better phase separation. Increasing the temperature, also, increase the internal energy of the system and this could be misinterpreted that the increased energy could counteract with the phase separation; however, it worth to mention that the changes in enthalpy of the system are constant.

This scenario is consistent for many of ATPSs based on polymer-salt systems [44]–[46], however, the influence of the temperature on ATPS systems comprised of PEG and DEX is different [47]. Better phase separation is obtained at a lower temperature for polymer-polymer ATPS systems [48]. Based on the model offered by Albertsson in equation (1.1), partition behaviour is dictated based on the six factors, and the influence of some of these factors could dominate the overall

behaviour of the system [49]. In ATPS systems comprised of PEG and DEX, K_{hfob} and K_{conf}, dominate the partitioning behaviour. The hydrophobicity of PEG increases by increasing the temperature [50] and this is related to the changes of PEG conformations in aqueous solution in different temperatures with different dipole and energies [51]. This suggests that at lower temperatures there is a low-energy polar conformation in PEG that results in aqueous solubility and the polymer is less hydrophobic, while higher temperature makes it more hydrophobic and change the PEG-water interaction that leads to migration of water molecules from PEG-rich phase into the DEX-rich phase [47].

ATPS has the advantage of being mild toward biological particles [52]. Due to this biocompatibility of ATPS, these biphasic systems are used in different biotechnological applications such as in partitioning of biomolecules [53], protein purification [54], and cell patterning [55].

The interfacial tension between the phases of an ATPS is generally very low, ranging from 10^{-6} to 10^{-4} N/m [56] (about 400-fold less than for water-oil systems). Low interfacial tension could be beneficial to applying less stress on biomolecules during partitioning, however, for the fabrication of soft biomaterials such as droplets, it is problematic.

In chapters 3 and 4, I develop novel technologies to overcome the ultralow interfacial tensions of ATPS and generate aqueous-based single, double, and triple emulsions. In conventional microfluidic devices, the disperse phase enters into a flow focusing junction while in contact with the top and bottom of channel walls. This complicates the droplet breakup process, and hindered the generation of ATPS emulsions. The platforms in this dissertation help to isolate the disperse phase(s) from the microchannel walls, and therefore, improve droplet production.

1.2.2 Electrohydrodynamic atomization

Electrohydrodynamic atomization (EHDA) facilitates the fabrication of microscale soft materials with a high production rate— up to 4×10^5 particles per second [57]. This technique is based on an electrical potential that is applied to a jet of fluid flowing out through a nozzle. The electrical force applied on the liquid jet forces the stream to break down into smaller droplets, a process called atomization. In this process, an electrical potential is generated between the positively

charged nozzle and a negatively charged metallic counter-electrode located underneath the emitter. The liquid jet is stripped of electrons, gaining a positive charge.

Electrochemical reactions in EHDA

Due to the effect of a high electric field, the liquid jet experiences an electrophoretic charge separation. This force drives positive ions in the fluid to move toward the meniscus and negative ions to migrate to the surface of the nozzle. The electrophoretic charge separation leads to charges on the liquid capacitor that impedes direct flow through the electric circuit of the system. This causes the oxidation of positive ions, and the reduction of the negative ions occur, and lead to the accumulation of charges on the jet of liquid. The excess surface charge on the fluid jet undergoes repulsion between droplets as they are all positively charged. Under specific conditions in which the electrostatic repulsion overcomes the surface tension force between air and the jet of liquid, charged droplets disperse uniformly from the tip of the liquid jet, forming a cone. The electrons in the positive ions of the droplets are neutralized when they contact the surface of the cathode of the high voltage power supply (Figure 1.3) [58].

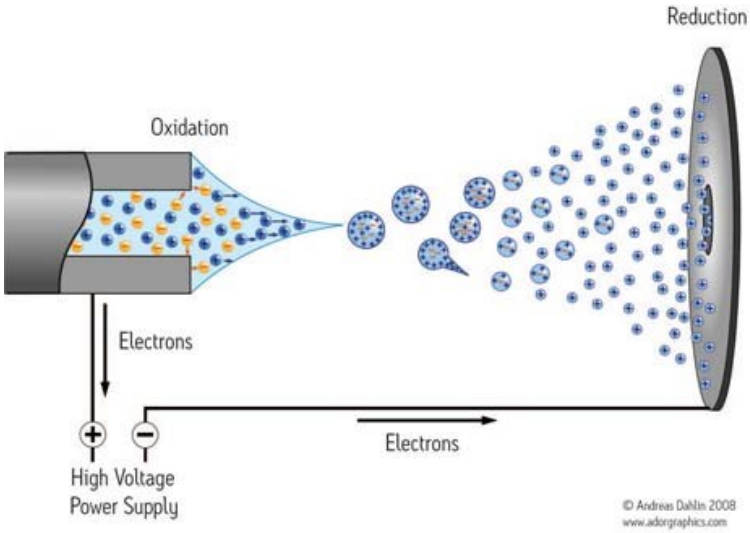

Figure 1.3: Under the effect of a strong electric field, liquid at the positive electrode gains a net positive charge, where the positive ions collect at the apex of the generated cone. The electrostatic repulsion causes the excess surface charge to overcome the surface tension of the liquid, which leads to the generation of a monodisperse spray of positively charged droplets, which accelerate towards the cathode [59].

Spraying modes

The droplet generation in EHDA can occur in various spraying modes in which each mode is dependent on different parameters, such as the strength of the electric stress, its effect on the surface tension, and kinetic energy of the liquid jet that is spraying from the nozzle [8].

The surface charge created by the electric field determines the meniscus shape at the tip of the nozzle. As the charge increases in the liquid, the shape of the protruding liquid becomes conical. This shape is mainly attributed to a competition between the dominance of electrostatic pressure (P_E) and surface tension pressure (P_γ). P_E is a repulsive force that is acting normal to the liquid surface in an outward direction and P_γ is the surface tension force between the interface of air and liquid jet acting in the opposite direction of the electrostatic repulsive force to minimize the surface area [60]. When these two pressures are balanced, a cone with an angle of 99º is formed, also known as a Taylor cone [61] (Figure 1.4).

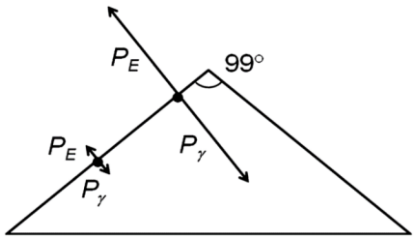

Figure 1.4: The equilibrium of the electrostatic and surface tension pressures results in the formation of the Taylor cone, with a whole angle of 99º. The apex of the cone experiences the highest intensity of the electric field [60].

Increasing the charge at the apex of the cone causes the electrostatic pressure to overcome the surface tension pressure and elongate the cone, then finally charged droplets start to form flowing towards the cathode (Figure 1.5).

Figure 1.5: Increase in the voltage causes the meniscus to deform to a conical shape, and charged droplets start to form from the jet of liquid [8].

The surface tension induces a pressure P_γ, which is equal to the product of the surface tension of the liquid γ and curvature of the nozzle's tip $\kappa = (1/r)$ [62].

$$P_\gamma = \gamma\, \kappa \tag{1.4}$$

The electrostatic pressure, P_E, is proportional to E^2, where E represents the electric field, and ε_0, which is the vacuum permittivity of the liquid [62].

$$P_E = 0.5\varepsilon_0 E^2\, \kappa \tag{1.5}$$

In order to form the Taylor cone, a critical voltage value, V_c, is needed. This voltage is proportional to the root of the product of the surface tension, γ, and distance from the tip of the nozzle to the counter electrode (cathode), L_t. Increasing the voltage beyond V_c results in an increase in electrostatic pressure P_E, and as a result, the Taylor cone elongates and droplets start to form [62]. The critical voltage V_c is calculated as:

$$V_c = 0.863 \sqrt{\left(\frac{\gamma Lt}{\varepsilon_0}\right)} \tag{1.6}$$

As the charged liquid start to form droplets—beyond V_c—the excess charge in the liquid at the tip of the nozzle decreases. This sudden loss of charge causes the system to stop spraying droplets and is followed by electrochemical reactions, which produce excess charge resulting in the generation of charged droplets. These cyclic reactions continue, and produce a successful spray of the liquid [60].

EHDA is a well-established, simple, and high-throughput technique that can be used in a range of different applications. These applications include the fabrication of micro- and nanoparticles and polymeric structures [63]–[65], encapsulation [66], [67], microbubble generation [68]–[70], preparation of multilayered polymeric structures [63], and food products [71].

1.2.3 Microfluidics

Microfluidics is another approach commonly used for the fabrication of soft-materials for biomedical applications. Microfluidics is the science of fluid behaviour in micro- and nano-scale

[72]. In these systems, since the fluid is geometrically constrained to a small scale, the fluid exhibits unique physical phenomena compared to that on a macroscopic scale. These phenomena include the dominance of capillary forces for mass transport, the presence of laminar flow, and negligible gravity due to the small size of the system.

Droplet microfluidics

Droplet microfluidics is a subcategory of microfluidics, focused on making discrete droplets inside a microchannel through immiscible multiphase flows [73] with low Reynolds number and laminar flow [74]. Droplet microfluidics makes it possible to conveniently handle small volumes of a liquid from microliters to femtoliters. Droplets in microchannels are generated by using two immiscible fluids. Of the phases formed, the one that forms droplets in a confining phase is referred to as the droplet phase, while the phase containing the droplets is referred to as the continuous phase. Droplets are mainly generated in three different channel geometries: coaxial, T-junction, and flow-focusing. In chapters 3 and 4, flow-focusing geometries are used. In these geometries, the disperse phase flows through a junction where the two phases meet. Then, the viscous forces applied by the continuous phase tends to extend and stretch the interface between the phases while the interfacial tension tends to reduce the interfacial area. The interaction of these forces leads to the formation of a dripping, jetting, or stable co-flow regime [75]. A schematic diagram of these three different regimes is illustrated in Figure 1.6.

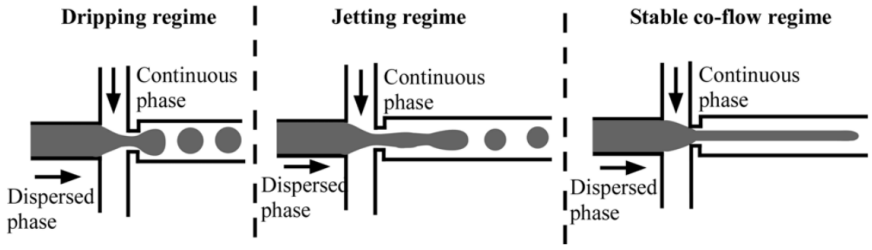

Figure 1.6: Schematic of flow-focusing microfluidic devices under three different regimes [75].

The aforementioned balance between the viscous force and the interfacial tension force is studied using a dimensionless number known as the capillary number, *Ca*, where,

$$Ca = \frac{\mu U}{\gamma}. \tag{1.7}$$

Here, μ is the dynamic viscosity of the continuous phase, U is the average velocity of the fluid inside the channel, and γ is the interfacial tension between the disperse and continuous phases. At

lower *Ca* the interfacial tension dominates, and the disperse phase forms spherical droplets under the dripping regime. In this scenario, the generated droplets are generally monodisperse.

However, for immiscible fluids with lower values of interfacial tension, the capillary number is higher, and droplet generation tends to occur in a jetting regime. The generated droplets in this regime have a higher size variation.

Ca is the most important non-dimensional number for droplet formation in the field of microfluidics. In droplet generation microfluidic systems, oil-water systems have $Ca = 10^{-3}$ to 10^{+1} [75]. Droplet generation in microfluidics using ATPS occurs in the same range, however the interfacial tension in this system is about three to five orders of magnitude lower than that in oil-water systems [56]. Consequently, to maintain the *Ca* within the range of possible droplet formation, the average velocity of the fluid inside the microchannel needs to be decreased. Without such a reduction in velocity, the system will generate a stable thread inside the channel (see above Figure 1.6). Lowering the average velocity this way also diminishes the throughput. Therefore, ATPS droplet microfluidics usually have much lower throughput, compared to generation using water-oil systems.

1.3 Objectives and hypothesis

The main objective of my research in this dissertation is the controlled generation of soft biomaterials using all-aqueous systems. These soft biomaterials can be used in biomedical and biomedicine applications without any washing steps after their synthesis. These systems also help to maintain the viability of the biological cargo including encapsulated cells since there is no organic solvent phase involved. The main objective of this research is to achieve by accomplishing the following secondary objectives:

The controlled fabrication of non-spherical biocompatible and biodegradable microparticles using aqueous fluids. Recent studies have revealed that the morphology and shape of drug-carrier particles affect the release mechanism of drug delivery [20], [21]. Utilizing EHDA could be beneficial towards the fabrication of non-spherical particles using all-aqueous systems. I hypothesize that there are three main parameters that could define the shape of fabricated particles. First, increasing the distance between the nozzle and the collection bath increases the impacting energy of the droplets to the bath surface and causes to spread the droplet on the free surface before

polymerization occurs. Second, increasing the polymerization initiator concentration in the liquid bath causes to increase the polymerization rate of the alginate-calcium particles and freezes the impacted particles faster. And thirdly, increasing the magnitude of the shear stresses exerted on the microparticles inside the collecting bath by the flowing of the liquid of the bath using a magnetic stirrer causes a curvature in the tails of the microparticles (Chapter 2).

Development of a microfluidic device to fabricate all-aqueous microdroplets using ATPS in a higher production rate compared with existing techniques. This platform is required to be able to generate droplets of both ATPS phases, either one containing the other. In the current ATPS droplet microfluidic platforms, introducing the disperse phase to a flow focusing junction while in contact with the top and bottom channel walls. This contact prevents a facile production of the droplets and is just as valid for the cases of the more hydrophilic disperse phase, DEX. I hypothesize that inserting a microneedle into the centre of the channel would help to isolate the disperse phase from top and bottom walls and facilitate a higher production rate. Moreover, with this configuration, the fabrication of PEG droplets is possible (Chapter 3).

Development of a novel microfluidic platform to generate double and triple emulsions using ATPS system where the phase separation is concurrent. The production of higher order ATPS emulsion in microfluidics is achievable by flowing non-equilibrium ATPS phases inside the microfluidic device and higher order emulsion drops are then induced by a spontaneous phase separation within the ATPS [76]. This type of system requires an accurate selection of the initial ATPS composition. Moreover, the formation of emulsions relying the phase separation highly depends on the kinetics of the phase separation that could affect the generation mechanism. I believe my previous hypothesis is also valid for the generation of higher order emulsion. Consequently, I hypothesize that using a conventional flow focusing device coupled with a coaxial microneedle and one or two glass capillaries embedded inside the microfluidic device could facilitate the breakup of the higher order ATPS emulsions (Chapter 4).

1.4 Author's contribution in the context of collaboration

The platforms presented in this dissertation are designed and developed by the author. The author is responsible for designing, prototyping, testing, validating, and assembling the platforms.

The platform presented in Chapter 2 to generate non-spherical microparticles was developed from existing technology for electrohydrodynamic atomization, to control the fabrication of non-spherical calcium-alginate microparticles. The ideas presented within this chapter were developed in collaboration with a visiting student, Sze Yi Mak, from the Department of Mechanical Engineering of the University of Hong Kong. We also conducted preliminary experiments together. I outlined the experimental plan, analyzed the collected data and performed most of the experiments after the preliminary work. An undergraduate research assistant, Stephen Sammut, helped to perform the experiments and collect data for some of the experiments.

The microfluidic platform presented in Chapter 3, was inspired by the design work of a previous graduate student, Vaskar Gnyawali, as a part of his Ph.D. dissertation. The idea of using this design to generate single ATPS emulsions was conceived mostly on my own, and in consultations with Niki Abbasi, a previous masters student. I conducted the device fabrication, designed the experimental setup, executed the experiments, analysed the data, and wrote the paper with my coauthors.

Niki Abbasi and I generated the concept of the precise microfluidic platform to generate double and triple emulsions, presented in Chapter 4. The microfluidic device was designed, fabricated and developed solely on my own. I outlined the experimental plan and performed most of the experiments. Data was analyzed solely by myself under supervision of my advisors. An undergraduate research assistant, Risavarshni Theyakumaran, helped to perform some of the experiments.

Chapter 2: Non-spherical microparticles

The work presented in this chapter is based on the following article published in a peer-reviewed journal *ChemPhysChem.*

Jeyhani, M., Mak, S. Y., Sammut, S., Shum, H. C., Hwang, D. K. and Tsai, S. S. H., "Controlled electrospray generation of non-spherical alginate microparticles." *ChemPhysChem*. 1-7 (2018). https://doi.org/10.1002/cphc.201701094

Author's contribution

The ideas of this chapter were developed in collaboration with a visiting student, Sze Yi Mak, from the Department of Mechanical Engineering of the University of Hong Kong. We also conducted preliminary experiments together. I outlined the experimental plan, analyzed the collected data, and performed most of the experiments after the preliminary work. An undergraduate research assistant, Stephen Sammut, helped to perform the experiments, and collect data for some of the experiments.

2.1 Introduction

Microparticles have found applications in a variety of different fields, including applications in pharmaceutical, food, pesticides, and cosmetic industries, as well as in biotechnological applications, for instance cell encapsulation for three-dimensional cell culturing for tissue engineering purposes [77]–[80]. Specifically, biodegradable and biocompatible microparticles are useful for drug delivery applications because of their unique features such as their small size, drug encapsulation ability, bioavailability, reduced toxicity, and minimized adverse health effects in comparison to conventional drug delivery methods [81]. These polymer drug carriers are often made with various biodegradable polymers [82], such as alginate. As a polysaccharide, alginate is one of the most used materials in applications such as the encapsulation of drugs, proteins, insulin, and cells in particles [21], [83], [84], in regenerative medicine [85], 3D culture [86]–[89], and tissue engineering [90].

The vast majority of research on drug delivery particles only use particles that are spherical [84],[91]–[93]. However, recent evidence in the literature suggests the emergence of the morphology of drug carrying particles as an important parameter controlling the mechanism of drug delivery [21], [81]. Namely, the shape of non-spherical particles affects the movement of particles in the presence of flow [81], and particle morphology impacts the drug release's pharmacokinetics [24], the mechanics of the drug carrier's transportation and circulation inside the body [22], [23], and the targeting ability of the particles as drug delivery vehicles [81].

Despite the fact that the morphology of alginate-based particles significantly affects the drug delivery mechanism, there are only a handful of manufacturing methods developed to tune the shape of alginate microparticles. The generation of non-spherical microparticles is possible using synthetic techniques such as lithography [94]–[97], photopolymerization [94]–[96], [98], and microfluidics [94]–[96]. However, barriers to generating shape-controllable alginate microparticles still persist. For example, combining microfluidics and photopolymerization is a well-developed technique to make highly tunable non-spherical particles [94]–[96], [98]–[100]. However, it is difficult to apply this method to generate non-spherical alginate microparticles because alginates need to be modified to be photocrosslinkable [101]. Gravity-driven droplet impact into calcium chloride baths is used to make non-spherical alginate microparticles, and it is known that the impact energy, fluid viscosity, and surface tension all contribute to determining the

final size and the shape of fabricated particles [102]–[104]. Other methods that make non-spherical microparticles are challenged by low throughput (for example, O(1-100) particles per second) [105], [106] and some cannot create microparticles that are less than hundreds of microns in diameter [104].

Here, we describe a new method, based on electrospraying, to manufacture non-spherical alginate microparticles. Electrosprays are able to generate microparticles at rates up to 4×10^5 particles per second[57], so this new method should overcome the low-throughput challenges associated with current techniques used to make non-spherical microparticles[106]. Our technique achieves alginate microparticles with tunable shapes, by adjusting several electrospray experimental parameters. Namely, we adjust the chemical initiator concentration of the liquid bath, and the distance from the metallic ring of the electrospray system to the free-surface of the liquid bath below. We note that the liquid-air surface tension and liquid viscosities should also play a role in controlling the resulting particle shape [103]. However, these variables are kept constant in our experiments (The values of these variables are provided in Tables I.1 and I.2 in Appendix I).

In this chapter, we first report our experimental observation of the different alginate microparticle morphologies achievable with our electrospray setup. We build a phase diagram of the possible particle shapes by systematically changing two experimental parameters: the chemical initiator concentration in the liquid bath and the distance from the metallic ring to the free surface of the bath. We also show that, for hemispherical shape microparticles, the particle aspect ratio—the particle height divided by its base—is controllable by the two experimental parameters. We further demonstrate that the action of stirring the liquid bath enables an additional interesting morphology—microparticles that have tail-like features whose curvature changes with the liquid stir rate. Finally, we demonstrate that the technique can be applied to make magnetizable non-spherical particles, and cell encapsulating non-spherical microcapsules. We anticipate that this approach to make non-spherical alginate microparticles will be able to address biomedical needs, including improving the efficacy of drug delivery, and enabling cell encapsulation and 3D cell culturing.

2.2 Experimental methods

2.2.1 Chemicals and cells

We prepare the alginate droplet phase solution as 2 wt% alginic acid sodium salt (Sigma-Aldrich Corp., St. Louis, MO, USA) in deionized (DI) water. The liquid bath phase is made with either 1 wt%, 2.5 wt%, 5 wt%, 7.5 wt%, or 10 wt% calcium chloride dihydrate (Sigma-Aldrich Corp., St. Louis, MO, USA) in DI water. We pass the alginate solution through a syringe filter that has 0.45 μm size pores (Corning Inc., NY, USA) prior to use, to remove particulates and impurities from the droplet phase. We use 0.945 μm diameter Sera-Mag carboxylate-modified magnetic speed-beads (Thermo Scientific, Waltham, MA, USA) in experiments that generate magnetizable non-spherical microparticles. We centrifuge 2 ml of the magnetic bead solution until form a cluster at the bottom. Then, we remove the liquid content of the magnetic bead solution, add the alginate solution, and suspend the magnetic beads by mixing the solution. We prepare the magnetic alginate solution this way so that the alginate concentration is unaltered upon addition of the magnetic beads.

In cell encapsulation experiments, we use BT-474 breast cancer cells (ATCC, Manassas, VA, USA), cultured using Dulbecco's modified eagle's medium (DMEM) with 10% fetal bovine serum (FBS). We incubate the cells at 37 °C with 5% CO_2 in a T-25 flask. We measure the concentration of cells by transferring 10 μL of the cell sample to a hemocytometer (Hausser Scientific, Horsham, PA, USA). The calculated number of cells is approximately 2.8×10^6 cells per mL. We centrifuge the cells in to remove the growth medium, and subsequently, we wash the cells with PBS to remove all the remaining DMEM. Then, we transfer the cells to a 1 mL alginate solution.

2.2.2 Experimental setup

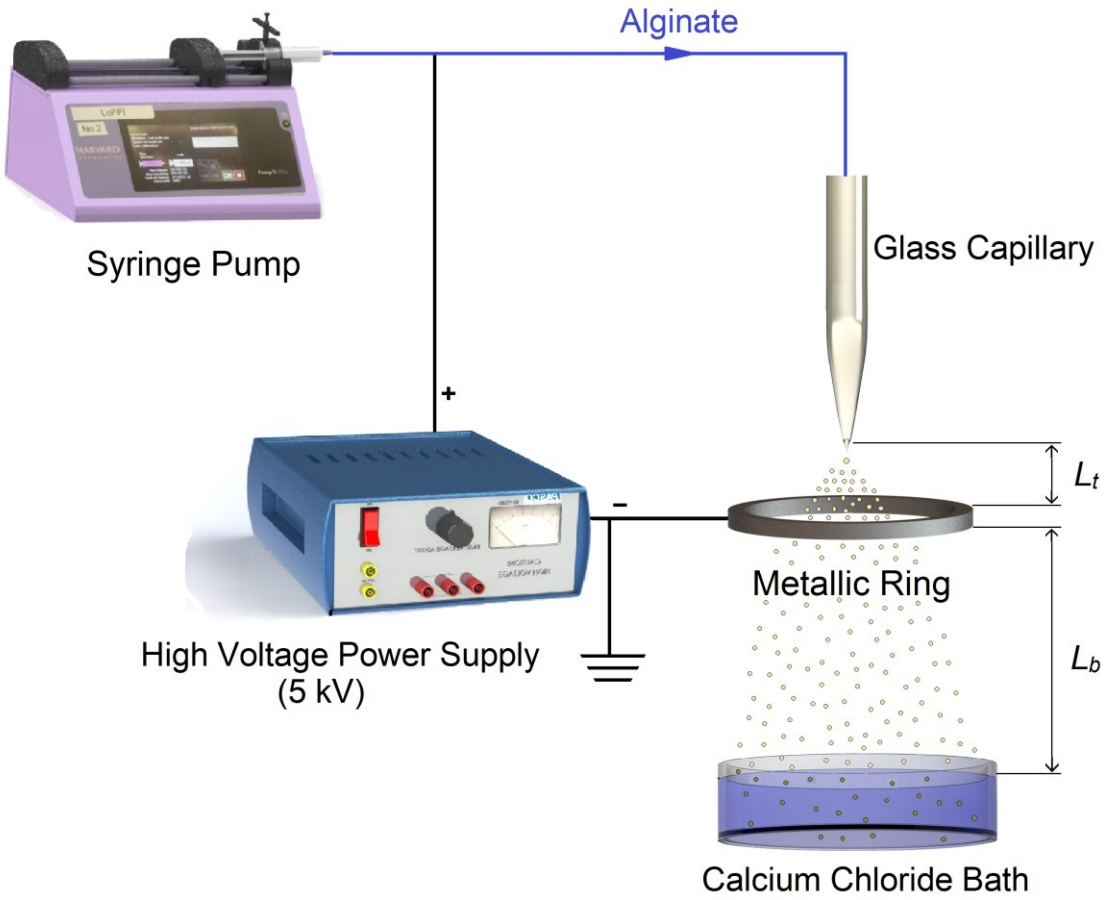

Figure 2.1: Schematic diagram of the electrospray system for alginate particle generation. A high-voltage power supply with low current is used to generate the electric field. The positively charged droplet phase is electrosprayed into a calcium chloride bath through a tapered glass capillary, to generate particles. The distance between the tip of the glass capillary and the ring is fixed at 1 mm. We adjust the distance between the ring and the free-surface of the calcium chloride bath, L_b, to observe its effects on the resulting particle shapes.

Figure 2.1 shows a schematic diagram of the experimental setup. We use a high-voltage power supply (Pasco Scientific, Roseville, CA, USA), with a constant voltage of 5 kV, to generate an electric field. The power supply is connected to a metallic needle on the dispensing syringe through a wire to positively charge the droplet phase. A metallic ring is also connected to the power supply, which is negatively charged. We use a constant flow rate syringe pump (Harvard Apparatus, Holliston, MA, USA), set at a flow rate of 0.1 mL/hr, to pump the droplet phase through tubing (Saint-Gobain Corp., Malvern, PA, USA) to a borosilicate glass capillary (O.D. = 1 mm and I.D. = 0.25 mm; A-M System Inc., Sequim, WA, USA). The tip of the glass capillary is tapered, using a micropipette puller (Model P-97, Sutter Instruments, Novato, CA, USA), so that the tip has a

diameter of 50 µm (± 5 µm). The internal and external surfaces of the glass capillary are coated with triethoxy(octyl)silane (Sigma-Aldrich Corp., St. Louis, MO, USA) to make the surfaces hydrophobic, which prevents wetting of the glass capillary and achieves smoother and more monodisperse dispensing.

Dispensed droplets pass through the negatively charged metallic ring under the effect of the electric field. As Scheme 1 shows, the distance between the glass capillary tip and the metallic ring, L_t = 1 mm. In our experiments, we investigate the effects on the formation and morphology of the particles by adjusting two variables: the liquid bath calcium chloride concentration, C, and the metallic ring to liquid bath surface distance, L_b (Figure 2.1). After the particles are formed, we image the morphology and structure of the particles using an inverted Zeiss optical microscope (Carl Zeiss, Oberkochen, Germany).

2.3 Results and discussion

2.3.1 Controlling the particles' morphology

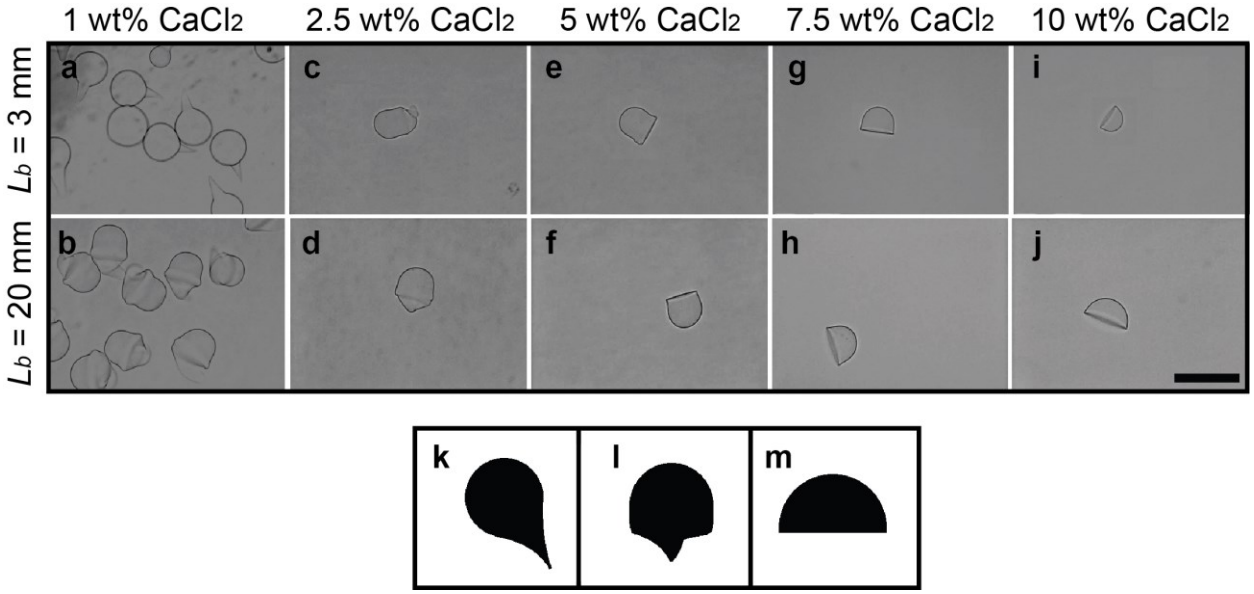

Figure 2.2: Particle shape controlled by electrospray properties. a) *Tadpole*-like microparticles are generated when the ring-to-bath distance L_b = 3 mm and the calcium chloride concentration C = 1 wt%. b-d) In all other cases in our experiments, where the calcium chloride concentration $C \leq 2.5$ wt%, we obtain *cupcake*-like particles. e-j) *Hemispherical* shaped particles are produced when the calcium chloride concentration $C \geq 5$ wt%. In all of these experiments, the voltage of the electrospray, and the flow rate of the pump are fixed at 5 kV and 0.1 mL/hr, respectively. Scale bar represents 150 µm. Illustrations that more clearly show what we define as k) *tadpole*-like, l) *cupcake*-like, and m) *hemispherical* shape microparticles.

The morphology of microparticles is important in controlling the efficacy of drug delivery and 3D cell culturing [21]. Figure 2.2a-2.2j shows microscopic images of microparticles formed using our electrospray setup, with corresponding values of the ring-to-bath distance, L_b, and liquid bath calcium chloride concentration, C. We observe tadpole-like (Figure 2.2k), cupcake-like (Figure 2.2l), and hemispherical shape (Figure 2.2m) microparticles, depending on our experimental values of the ring-to-bath distance, L_b, and liquid bath calcium chloride concentration, C.

Notably, the tadpole-like and cupcake-like microparticles only form when the calcium chloride concentration $C < 5$ wt%. Tadpole-like shape particles occur when the ring-to-bath distance L_b is low. When L_b is high, cupcake-like particles form.

2.3.2 Controlling the aspect ratio of hemispherical microparticles

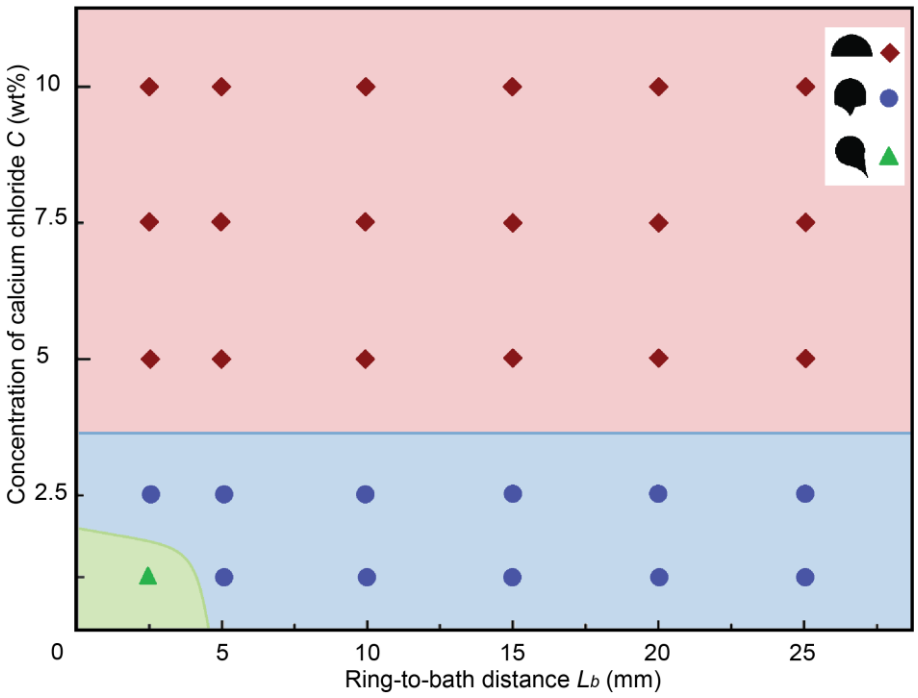

Figure 2.3: Different types of alginate microparticles. A phase diagram of the generated calcium-alginate particles illustrates differences in particle shape as a result of changing the calcium chloride concentration C, and the ring-to-bath distance L_b. We find that the electrospray setup generates hemispherical particles as long as calcium chloride concentrations $C \geq 5$ wt%. When calcium chloride concentration $C < 5$ wt%, we observe tadpole-like particles or cupcake-like particles.

The phase diagram in Figure 2.3 shows that when the liquid bath calcium chloride concentration $C \geq 5$ wt%, our system produces only hemispherical microparticles. Our hypothesis is that increasing the chemical initiator concentration, C, of the liquid bath, increases the alginate-calcium

gelation rate. Therefore, when the alginate droplets from the electrospray impact the free surface of the bath, they deform such that the bottom side of the droplets flatten, and the immediate gelation of the alginate droplets "freezes" the droplets' hemispherical shapes (Figure 2.2e – 2.2j). (Further details of our hypothesis on the formation mechanism of hemispherical particles is discussed in Appendix I, and shown in Figure I.1.) In this regime, we define the particle aspect ratio $\Omega = h/b$, where h and b are the height and base length of the hemisphere, respectively (Figure 2.4a).

In order to distinguish between different microparticle shape regimes, we define a Shape Index $SI = (h - d) / (h + d)$, where d is the effective diameter of the microparticle. When $SI < 0$, the fabricated microparticles are defined to be of hemispherical shape. For $SI > 0$, we observe both tadpole-like and cupcake-like particles. To differentiate between tadpole-like and cupcake-like particles, we further define a Normalized Tail-Length $TL = w/d$, where w is the width of the tail. When $TL < 0.5$, tadpole-like microparticles are formed, and when $TL > 0.5$, cupcake-like microparticles are produced. (Further details of how the shapes are defined are discussed in Appendix I.)

Figure 2.4b shows that increasing the calcium chloride concentration C results in decreasing aspect ratio Ω. There is also a nearly monotonic decrease of the aspect ratio Ω with increasing ring-to-bath distance L_b. The decrease in aspect ratio Ω indicates that the hemispheres are flatter. Larger ring-to-bath distances L_b also result in more repeatable control of particle shape, as indicated by the aspect ratio Ω's smaller error bars.

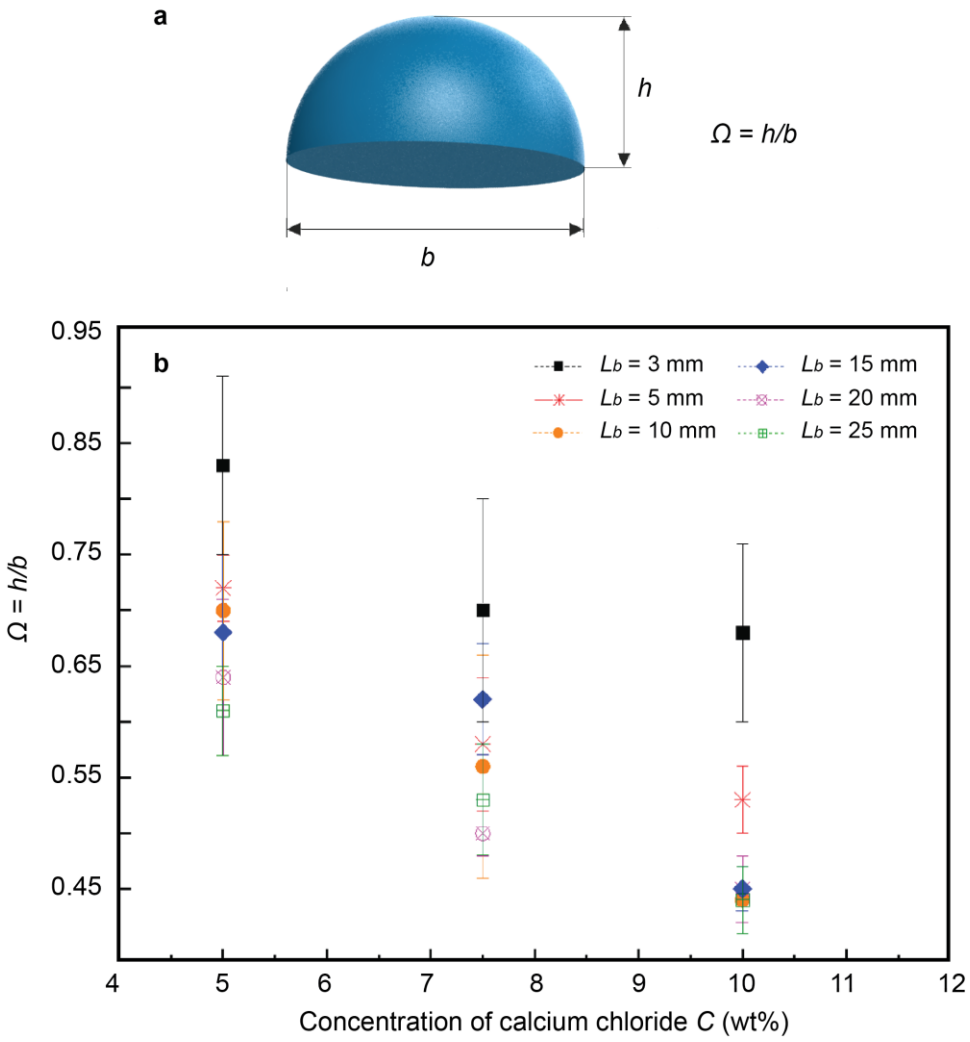

Figure 2.4: Hemispherical particle aspect ratio $\Omega = h/b$ controlled by the liquid bath calcium chloride concentration C and the ring-to-bath distance L_b. a) Ω is defined as the ratio between the height h of the hemisphere and its base length b. b) A plot of the resulting hemispherical particle aspect ratio Ω versus the calcium chloride concentration C. Different symbols represents distinct values of the ring-to-bath distance L_b. Increasing the ring-to-bath distance L_b for a particular calcium chloride concentration C results in a nearly monotonic decrease in particle aspect ratio Ω. Increasing the calcium chloride concentration C, while fixing the ring-to-bath distance L_b also results in a nearly monotonic decrease in Ω. Error bars indicate one standard deviation in a sample size of 20 particles (Appendix IV).

2.3.3 Generating microparticles with curved tails

An additional parameter that we can adjust in our electrospray setup is the flow of the liquid in the calcium chloride bath. In normal conditions, the liquid bath is static, however, we can simply use a magnetic stirrer to controllably create a flow in the liquid bath. As a proof-of-concept demonstration, we conduct an experiment using a ring-to-bath distance $L_b = 10$ mm, and a calcium

chloride concentration C = 10 wt%, while stirring the bath. We generate different degrees of flow in the liquid bath by tuning the rotational rate of the magnetic stirrer in the bath at 50, 250, and 500 rpm.

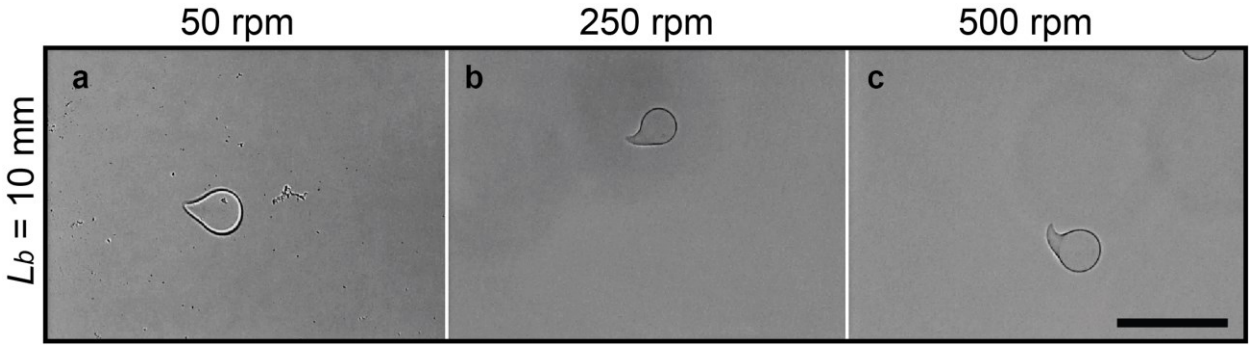

Figure 2.5: The effect of stirring the liquid bath. We use a magnetic stirrer to create a flow in the liquid bath. Here, the ring-to-bath distance L_b = 10 mm, and calcium chloride concentration C = 10 wt%. As the magnetic stirrer rotation rate increases from a) 50, b) 250, to c) 500 rpm, the curvature of the resulting particle increases. Scale bar represents 150 μm.

Interestingly, we observe that the liquid bath flow results in the production of tear-shaped particles (Figure 2.5). When we increase the fluid flow by increasing the magnetic stirrer's rotational rate, we observe qualitatively, that the microparticle tails' curvature increases. We hypothesize that this curvature is influenced by the magnitude of shear stresses exerted on the microparticle, by the flow in the bath.

2.3.4 Generating non-spherical magnetizable microparticles

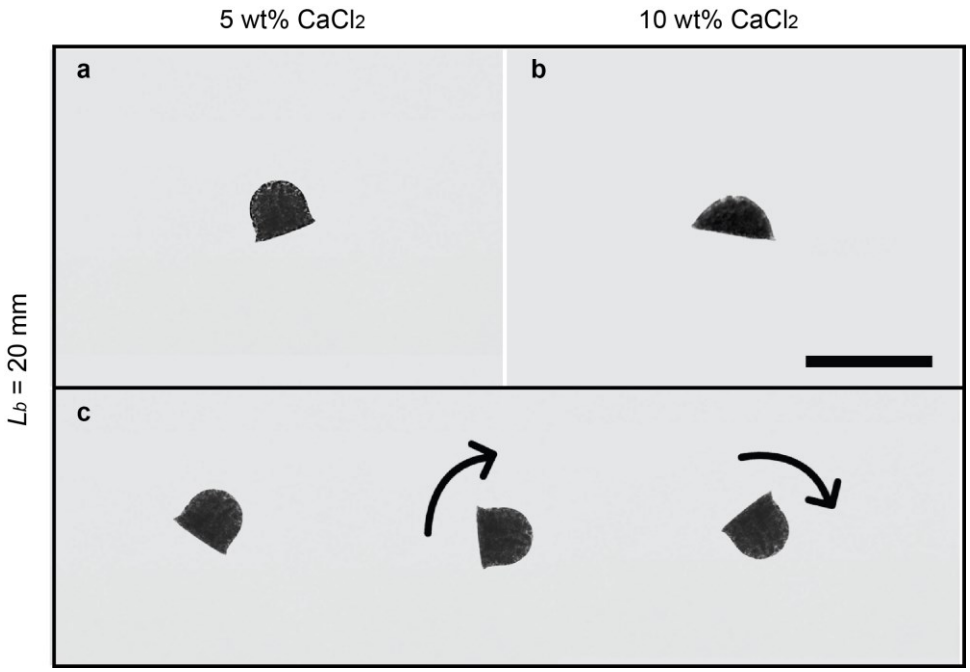

Figure 2.6: Magnetic particles. Fabrication of magnetic microparticles using magnetic beads. The ring-to-bath distance is fixed at L_b = 20 mm, and two different calcium chloride concentrations a) C = 5 and b) C = 10 wt% are used, resulting in different particle aspect ratios Ω. c) A sequence of images showing that an external magnetic field from a moving permanent magnet causes a particle to rotate. Scale bar represents 150 μm.

Our technique can also be adapted to create microparticles that have the added functionality of magnetizability. Figure 2.6 shows the magnetized non-spherical microparticles fabricated using our electrospray technique. Here, we add carboxylate-modified magnetic beads to the alginate precursor solution. As a proof-of-concept, we perform two sets of experiments with calcium chloride concentrations C = 5 and 10 wt%, and a ring-to-bath distance L_b = 20 mm, while keeping all other parameters constant.

The fabricated magnetic microparticles are able to preserve the non-spherical shape of microparticles without magnetic function (Figure 2.6). These particles are magnetizable, and rotate in the presence of a moving magnetic field (see Figure 2.6 and also Appendix I, Video 1 and 2). This electrospray technique is therefore applicable to manufacturing magnetizable non-spherical particles at high throughput, for magnetic separation schemes [107].

2.3.5 Cell encapsulation

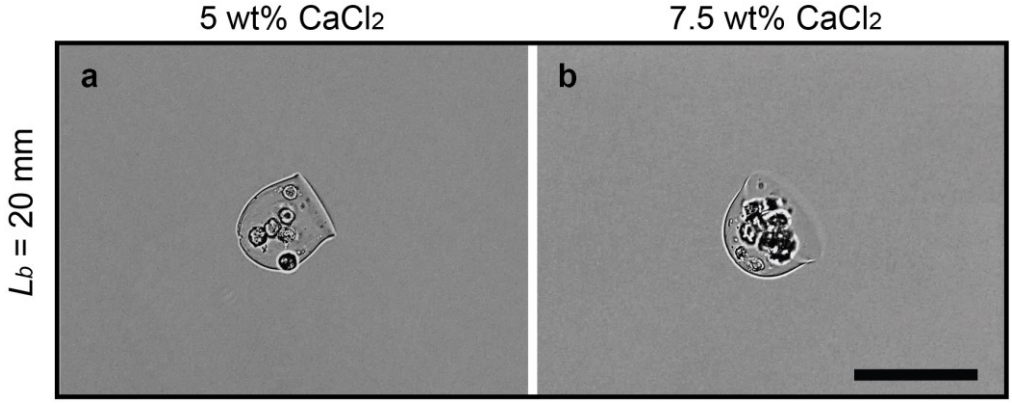

Figure 2.7: Cell encapsulation. BT-474 breast cancer cells encapsulated in hemispherical microparticles using our electrospray technique. Here, the ring-to-bath distance is fixed at L_b = 20 mm, and we use two different calcium chloride concentrations, a) C = 5 and b) C = 7.5 wt%. Scale bar represents 150 μm.

Figure 2.7 illustrates the encapsulation of breast cancer cells in non-spherical microparticles. The suspension of cells in alginate is sprayed into the bath, using our electrospray technique, and upon gelation of the particle, cells are encapsulated. Cell encapsulation in non-spherical microparticles, such as the ones shown here, maybe desirable for immunoisolation of cells [108]–[110]. This platform has the potential to achieve mass production of encapsulated cells while providing control on the size and the shape of the cell encapsulating vehicles.

2.4 Conclusions

Even though microparticle shape is an important parameter in determining the effectiveness of drug delivery and 3D cell culturing, there are very few established methods to generate non-spherical biocompatible microparticles in a high throughput manner. The electrospray-based technique for producing non-spherical alginate microparticles, which we describe, provides precise control over the shape of biocompatible microparticles produced, by simply tuning the experimental parameters of the system.

We demonstrate that the setup's ring-to-bath distance L_b and the calcium chloride concentration C can both be used to control the final shape of the microparticles. We show the proof-of-concept production of particles that have tunable curvature tails, by magnetically stirring the liquid calcium chloride bath. We also show that the technique can be applied to generate magnetizable and cell encapsulating non-spherical alginate microparticles. Since electrospray is a method that generates

particles at high throughput [57], [111], we anticipate that this new non-spherical particle generation method will find utility in biomedical applications that benefit from shape-controlled biocompatible microparticles, such as cell encapsulation, drug delivery, and 3D cell culturing.

Chapter 3: All-aqueous single emulsions

The work presented in this chapter is based on the following article published in a peer-reviewed journal *Journal of Colloid and Interface Science.*

Jeyhani, M., Gnyawali, V., Abbasi, N., Kun Hwang, D. & Tsai, S. S. H. "Microneedle-assisted microfluidic flow focusing for versatile and high throughput water-in-water droplet generation." *J. Colloid Interface Sci.* **553**, 382–389 (2019). https://doi.org/10.1016/j.jcis.2019.05.100

Author's contribution

The microfluidic device in this paper was inspired by a designed of a previous graduate student, Vaskar Gnyawali, as a part of his dissertation. The idea of using this design to generate single ATPS emulsions developed collaboratively between me and a previous graduate student, Niki Abbasi. I conducted the device fabrication, experimental setup design, execution of the planned experiments, data analysis, and writing of the paper.

3.1 Introduction

Droplet-based microfluidics platforms allow for the generation of highly monodispersed droplets, ranging from picoliters to nanoliters in volume. Microdroplets in microfluidics have been used for various applications such as molecular detection [112], drug delivery [113], [114], imaging [115], [116], diagnostics [117], single-cell analysis [118]–[121], evolution of biomolecules [119], [122], cell encapsulation and cultivation [123]–[126], and for generating food-grade emulsions [127].

Droplet microfluidics platforms mostly utilize immiscible liquids to either make water-in-oil or oil-in-water emulsions. For many biotechnological applications, the oil phase needs to be removed once droplets are formed because of the oil's non-biocompatible nature. However, the complete removal of oil from the system is highly time- and labour-consuming [26]. Thus, ATPS based water-in-water droplet microfluidics platforms have emerged in recent years as a possible alternative [128], [129].

ATPS was accidentally discovered in 1896 by Martinus Willem Beijerinck [31], and later its applications in biotechnology were realized by Per-Åke Albertsson [32], [33]. These aqueous biphasic systems are composed of a mixture of two incompatible polymers in an aqueous medium that separates into two distinct phases. A highly studied ATPS is a mixture of polyethylene glycol and dextran [130].

Due to their biocompatibility, ATPSs have been used in a variety of different biotechnological applications, such as the fractionation of cells into subpopulations [131]–[135], biomolecule partitioning [136]–[141], cell patterning [55], [142], and protein purification and extraction [54], [143]–[146]. The biocompatible nature of ATPS also makes it a viable alternative to conventional water-in-oil systems, for producing microdroplets, eliminating the need for post-processing washing steps.

In flow focusing microfluidic platforms, droplet generation is driven by the balance between surface tension and viscous forces. Surface tension tends to minimize the interfacial area between interacting liquids, while viscous forces tend to stretch the interface [75], [147]–[149]. Since ATPS generally have very low interfacial tensions, ranging from 10^{-6} to 10^{-4} N/m [56]—albeit, some ATPS, such as those based on PEG-inorganic salts, can have interfacial tensions exceeding 1 mN/m—it is challenging to generate discrete droplets with ATPS in current flow focusing

droplet microfluidics geometries. Indeed, it is often observed that, when trying to generate droplets with ATPS, viscous forces dominate the system and result in very long threads inside the channel [150].

Alternative microfluidic approaches, namely with active perturbation inside microchannels, have been successfully utilized to generate water-in-water droplets. Some examples of such active perturbation include using a piezoelectric disc to oscillate channel walls [151], [152], using a mechanical vibration table to oscillate the flow [153]–[155], and pulsating the inlet pressure of the dispersed phase fluid [128]. The main drawback of active droplet formation techniques is that they require external components to perturb the flow controllably, which often involve complicated experimental setup.

Recently, Moon *et al.* developed a passive microfluidic platform for generating monodisperse water-in-water droplets [129]. This platform requires neither pumps nor external components to form droplets. Instead, with pipette tips filled with ATPS solutions, the hydrostatic pressure of the fluid columns drives the flow of fluids into the chip and form droplets. Although this passive droplet generation scheme is very simple and easily adapted for various applications, this approach suffers from droplet size-selectivity and throughput.

Additionally, like all of the other existing microfluidic platforms that generate water-in-water droplets based in DEX and PEG polymers, only DEX-in-PEG droplets are producible [25], [128], [129], [151], [153]–[158], due to the PEG phase's stronger interactions with PDMS and glass channel walls [159].

In this chapter, we describe an approach whereby we make a simple modification to the conventional flow focusing microfluidic geometry and achieve both high throughput production of water-in-water droplets, and the ability to make both DEX-in-PEG *and* PEG-in-DEX droplets. Namely, we integrate a microneedle into a conventional flow focusing PDMS microfluidic channel to 3D focus the disperse phase flow into the continuous phase. This 3D flow focusing helps to prevent the interaction between the dispersed phase and the channel walls, removing wetting effects of the disperse phase, and facilitating more robust droplet generation.

3D focusing approaches have been reported previously, including methods that use concentric cylinders made from glass capillaries [160]–[162], and by microfabrication of circular cross-

section orifices that lead to a flow focusing junction [163]. The 3D focusing in our approach is similar to that observed in some glass capillary-based microfluidic systems. However, embedding a microneedle in a PDMS microchannel, as seen in this study, has several advantages. Namely, the tapered glass capillaries used in microfluidics are fragile, and it is challenging to consistently taper the capillaries with high precision. In contrast, all of the dimensions—from the size of the commercially available microneedle to the PDMS channel made with soft lithography—in our platform are fixed, and the materials that we use are robust.

We first compare water-in-water droplet generation results from microneedle-embedded and needleless microfluidic devices and produce phase diagrams that elucidate droplet-producing regimes. We next investigate the effects of changing the pressures of the two phases on the resulting droplet diameters, a, and production throughput. Finally, we demonstrate the successful generation of PEG-in-DEX droplets, which has to date not been achievable microfluidically, by using 3D flow focusing to isolate the disperse PEG phase from the microchannel walls. We anticipate that this simple addition—insertion of a microneedle—to existing passive water-in-water droplet microfluidic systems, as demonstrated in this study, and the resulting increase in throughput and versatility in droplet production, will be useful in the development of biotechnological applications, such as in creating microparticle drug delivery capsules, encapsulating cells for single cell analysis, and immunoisolating cells for cellular transplantation.

3.2 Experimental methods

3.2.1 Chemicals

We prepare ATPS solutions by phase separating a mixture of an aqueous solution of 10% (w/v) poly(ethylene) glycol (PEG, M_w: 35 kDa, Sigma-Aldrich, St. Louis, MI, USA) and an aqueous solution of 20% (w/v) dextran (DEX, M_w: 500 kDa, Pharmacosmos, Holbaek, Denmark) by centrifuging (Sorvall Legend RT, Germany) at 1,400 RPM for 1.5 hours. Once equilibrated, we use a serological pipette to extract PEG-rich and DEX-rich phases using a pipette controller. We use a glass viscometer to measure the viscosity of the solutions. The DEX-rich phase viscosity, μ_D = 153.3 mPa s, and the PEG-rich phase viscosity, μ_P = 28 mPa s. From the measurements of Atefi *et al.* [38], we find that the ATPS used in this experimental study has interfacial tension, γ = 0.150 mN/m. We measure the densities of PEG-rich and DEX-rich phases, ρ_P = 1.014 g/cm^3 and ρ_D =

1.075 g/cm^3, respectively. All the measurements and experiment conducted at ambient temperature of 24 ± 1 °C. To visualize the dispersed phase flow's profile using confocal microscopy, we add 1% (w/v) fluorescein (Sigma-Aldrich, St. Louis, MI, USA) to the PEG solution.

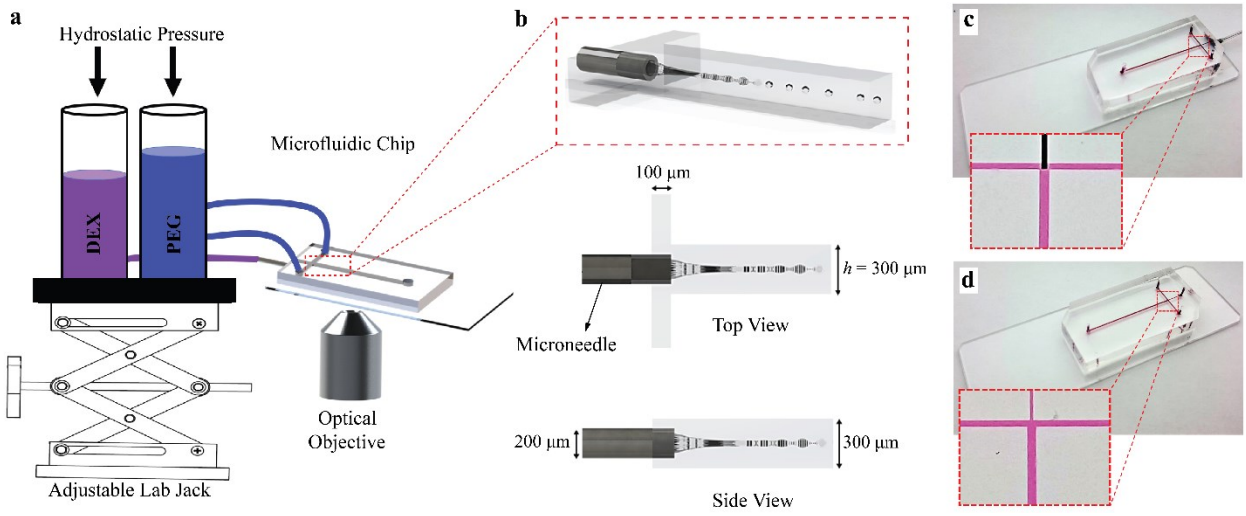

Figure 3.1: (a) Schematic diagram of the experimental setup for a passive ATPS droplet formation. Two plastic syringe tubes filled with each respective phase are connected to the microfluidic chip through the tubing. An adjustable lab jack is used to adjust the effective column heights of the phases to adjust the hydrostatic pressures. (b) Representative schematic diagram of the microfluidic chip. A microneedle is inserted as the inlet of the disperse phase inside the microfluidic chip. The microneedle is accurately located at the center of the channel to leave gaps between the channel walls and the needle, enabling 3D focusing of the disperse phase to the center of the channel. (c & d) Images of the needle device and the needleless device, respectively.

3.2.2 Experimental Setup

Figure 3.1a shows a schematic diagram of the experimental setup. We control the hydrostatic pressure from the liquid columns using an adjustable lab jack to change the effective liquid column heights inside 60 mL plastic BD syringe tubes (Becton, Dickinson and Company, Franklin Lakes, New Jersey, USA) assembled over a plastic test tube rack. The plastic syringe tubes used in this study have wide inner diameters to maintain nearly constant pressures over several hours. We note that our system is also compatible with both commercially available pressure-controlled pumps, such as the Fluigent LineUP or Flow EZ.

The effective column heights are measured from the liquid level in syringe tubes to the glass slide of the microfluidic chip. We also control the pressure of the liquids by adding/removing solutions using a pipette controller. Hydrostatic pressure drives the flows into the channels through the tubing, allowing the generation of ATPS droplets. The DEX and PEG solutions form disperse and continuous phases, respectively, unless otherwise stated.

Experimental images and videos are captured using a high-speed camera (Miro M110, Vision Research, Wayne, NJ, USA) connected to an inverted brightfield optical microscope (Axio Observer A1, Carl Zeiss, Oberkochen, Germany). A confocal microscope (LSM700, Carl Zeiss, Oberkochen, Germany) is used for confocal imaging. We use ImageJ software to post-process captured videos and images.

3.2.3 Device Fabrication

We fabricate the device based on the standard soft lithography method [164]. As seen in Figure 3.1b, the microfluidic device is comprised of two inlets for the continuous flow, one inlet for the dispersed phase, and one outlet. The continuous and disperse phase flow channels are 200 and 100 μm wide, respectively, and converge at a flow focusing junction. The width of the channel downstream of the cross-junction is h = 300 μm (Figure 3.1b), and the height of all channels is 300 μm. The microfabrication procedure to construct the feature of the mould is explained in Appendix II under Device Fabrication.

To complete the device fabrication, we modify the chip to focus the flow in 3D, by the insertion of a microneedle [165], [166]. Namely, we cut the PDMS slab at the disperse phase inlet and manually insert a metallic microneedle (34G; I.D. = 100 μm, O.D. = 200 μm; Japan Bio Products, Tokyo, Japan) through the inlet channel to reach to the cross-junction (Figure 3.1b). To ensure proper alignment of the microneedle, we inspect it under a stereomicroscope (E-Zoom 6 V, Edmund Optics Inc., Barrington, NJ, USA). To position the microneedle vertically in the z-direction, we stick two layers of tape (3M, St. Paul, MN, USA) underneath the needle to elevate the microneedle to obtain a 40 μm gap between the needle and the bottom of the channel. The microneedle is bonded to the cover glass slide and PDMS to seal the channel using two-component epoxy glue (Henkel Canada Corporation, Mississauga, ON, Canada). Lastly, the microneedle is connected to tubing (Saint-Gobian, Malvern, PA, USA) using the same epoxy glue.

3.3 Results and discussion

ATPS mixtures have very low interfacial tensions, and as a result, have much slower interfacial dynamics [150], which has made making water-in-water droplets microfluidically unattainable without active perturbation of the fluids. The complexity of active perturbation methods has hindered the exploitation of ATPS in microfluidics for droplet generation.

3.3.1 Droplet generation regimes

Recently, our group pioneered a passive hydrostatics-based microfluidic approach to generate water-in-water droplets, without the complexity of active methods [129]. While this passive droplet generation scheme is simple and easily adapted for various applications, this approach is limited in the size range of droplets produced and has a low throughput of $O(10)$ Hz. Here, we make a simple change to our previous microfluidic geometry, by the insertion of a microneedle to the disperse phase inlet, to isolate the disperse phase from the PDMS and glass channel walls (Figure 3.1b). As Figure 3.2 shows, this modification of our existing geometry facilitates the generation of microdroplets with a wide range of sizes.

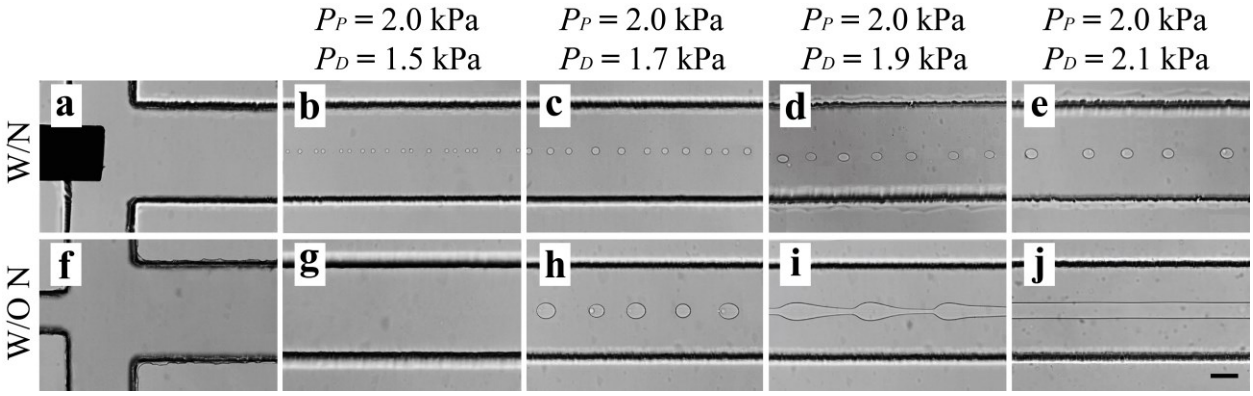

Figure 3.2: Experimental images of water-in-water droplet generation using the passive microfluidic platform and comparison between the device with an inserted needle (W/N) and the device without the needle (W/O N), with different, disperse and continuous column heights, P_D and P_P, respectively. (a-e) In the W/N device, a broad range of hydrostatic column heights can be used for generating droplets, due to the 3D flow focusing of the dispersed phase. (f-j) The same hydrostatic column heights with the W/O N device results in four different regimes of (g) backflow, (h) droplets, (i) ripple-shaped thread, and (j) continuous thread along the channel. Scale bar represents 100 μm.

Figures 3.2a and 3.2f show the cross junction of the devices with the needle (W/N) and without the needle (W/O N), respectively. Figure 3.2b-e show the generation of DEX droplets in the W/N device using a constant PEG column pressure P_P = 2.0 kPa, and various DEX column pressures

P_D = 1.5 - 2.1 kPa. Water-in-water droplets form within the W/N device through the entire range of PEG column pressures, P_P (Figure 3.2b-e). The W/O N device only generates droplets for the case where P_D = 1.7 kPa (Figure 3.2h). At the other column pressures that we investigated, the W/O N device shows three regimes: no droplet formation (Figure 3.2f), backflow (Figure 3.2g), ripple-shaped thread (Figure 3.2i), and long thread (Figure 3.2j).

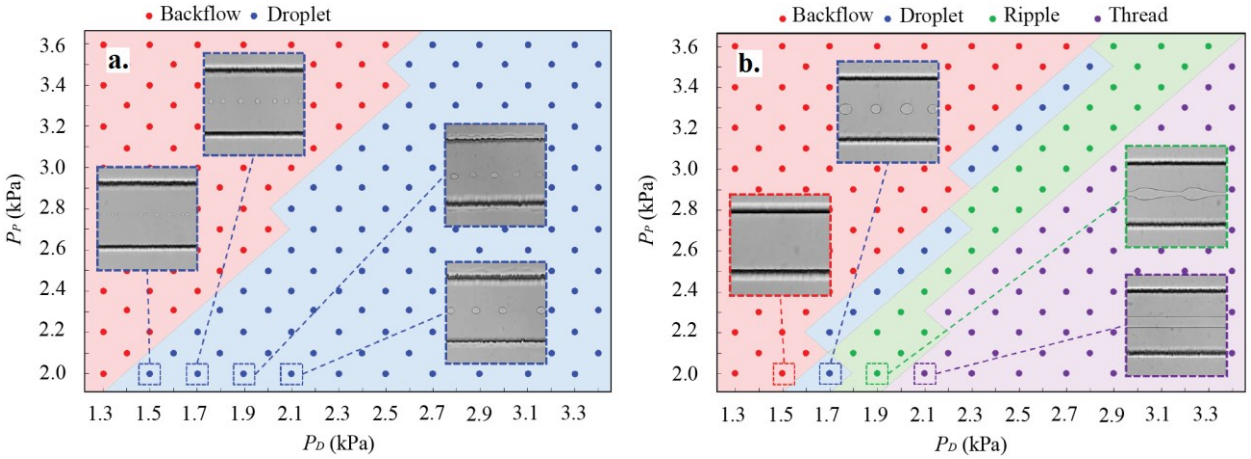

Figure 3.3: Phase diagram for flow regimes in the device W/N and the device W/O N. (a) The W/N device either results in droplet formation, or backflow, and no other regimes are observed in the ranges of hydrostatic heights used. (b) In the device W/O N, we observe four regimes: backflow, droplet formation, ripple-shaped threads, and continuous threads.

We further investigate the effect of changing PEG and DEX liquid column pressures on droplet generation for the devices W/N and W/O N. For the device W/N, we find that the system either produces droplets, or backflow, with a broad range of P_D and P_P values resulting in droplet formation (Figure 3.3a). However, in the device W/O N, in the same ranges of P_D and P_P, we observe four regimes: backflow, droplet formation, ripple-shaped threads, and continuous threads.

Notably, the range column pressures resulting in the droplet generation regime in the device W/O N is very small compared to that of the device W/N. We hypothesize that, in the device W/N, the dispersed phase flow is focused from all directions, preventing the dispersed phase from wetting the walls of the device, thereby facilitating droplet formation. In the device W/O N, the top and bottom walls of the channel are wetted by the dispersed phase, and the sheath flow only focuses the dispersed phase laterally. We anticipate that the wetting of top and bottom walls by the dispersed phase in the device W/O N makes it more challenging for droplets to detach from the disperse phase thread. Therefore, the simple modification of inserting a microneedle to the disperse

phase inlet enables droplet formation over a wide range of hydrostatic pressures, P_D and P_P, that is unattainable in a device without the microneedle.

In microfluidics, droplets form due to a competition between viscous stresses and capillary pressure, which is defined by the dimensionless Capillary number, $Ca = \frac{\mu_C U}{\gamma}$, where U is the average velocity of the fluid flowing inside the channel and μ_C is the viscosity of the continuous phase. The Capillary number, Ca, is used in the droplet microfluidics literature to characterize the droplet formation regime, for example, whether the system is in the dripping or jetting mode, and predict the resulting droplet size [147]. In our experiments, and in other passive droplet microfluidic systems that use ATPS, the Capillary number, Ca, is typically high. This is due to the very low interfacial tension of most ATPS. In our experiments, we find that the range of Capillary number, $Ca = 2.3 – 4$, is associated with successful droplet generation for devices W/O N. Outside of this range, we observe backflow, ripples, and thread formation. In devices W/N, the droplet generation Capillary number range, $Ca = 0.8 – 4.5$. These ranges are of the same order-of-magnitude as those reported for water-in-oil or oil-in-water systems [147]. We note further, that the Capillary number range is significantly larger in devices W/N, which reinforces our assertion that integrating the microneedle helps enable droplet formation in a wider range of experimental conditions.

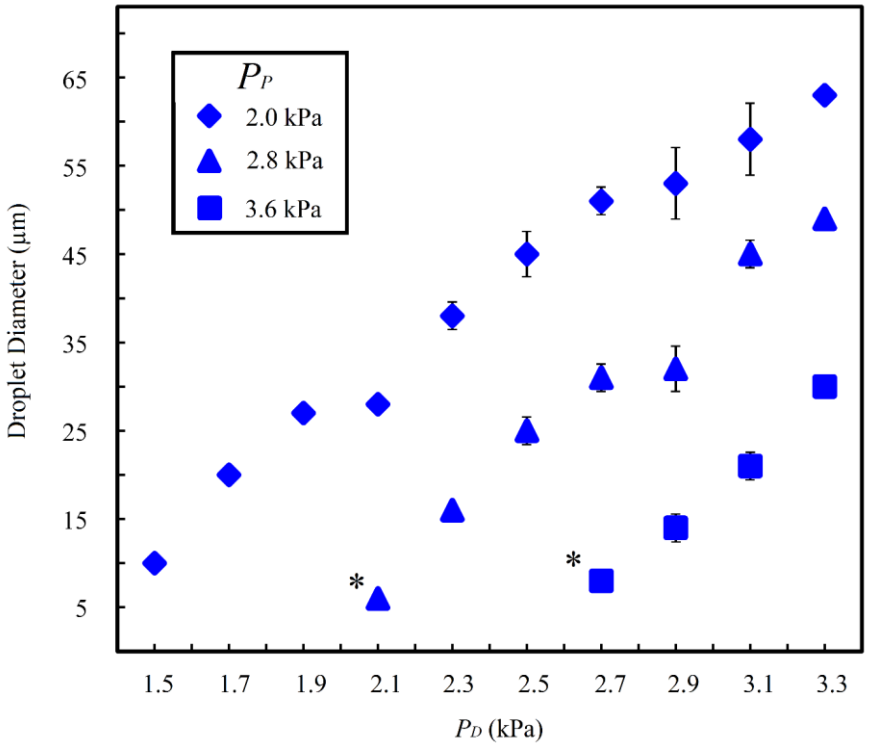

Figure 3.4: The diameter of droplets formed versus the DEX liquid column pressure, P_D, for three different PEG liquid column pressures, P_P, inside the device W/N. Diamond markers (♦) represent data points for P_P = 2.0 kPa, triangle markers (▲) show data points for P_P = 2.8 kPa, and squares (■) represent data points for P_P = 3.6 kPa. For all three data series, increasing P_D, while fixing P_P, results in the formation of larger droplets. The data points with an asterisk (*) denotes the threshold of the droplet regime for the particular data series, below which backflow occurs. Error bars indicate one standard deviation in a sample size of 30 droplets.

3.3.2 Droplet generation diameters

Using the device W/N, we study the effects of changing the dispersed DEX phase liquid pressures, P_D, while the PEG liquid column pressure, P_P, is constant. As shown in Figure 3.4, we find that increasing the DEX column pressure, P_D, results in an increase of the DEX droplet diameter, and this effect is observed for three different PEG liquid column pressures, P_P. We also note that increasing the column pressure, P_P, for the continuous PEG phase, from P_P = 2.0 – 3.6 kPa, results in a decrease of droplet diameter.

Figure 3.5 shows a log-log plot of the normalized droplet diameter a/h versus a dimensionless ratio of DEX and PEG phase inlet pressures and fluid viscosities, $(P_D/\mu_D)/(P_P/\mu_P)$. Here, we observe an empirical relationship for the droplet diameter, $a/h \propto ((P_D/\mu_D)/(P_P/\mu_P))^2$, and a constant of proportionality of approximately 4. We note that this empirical power-law relationship is

consistent with our previous observations for water-in-water droplet formation using rectangular microchannels without an inserted microneedle [129], and also consistent with results from the water-in-oil droplet microfluidics systems [167].

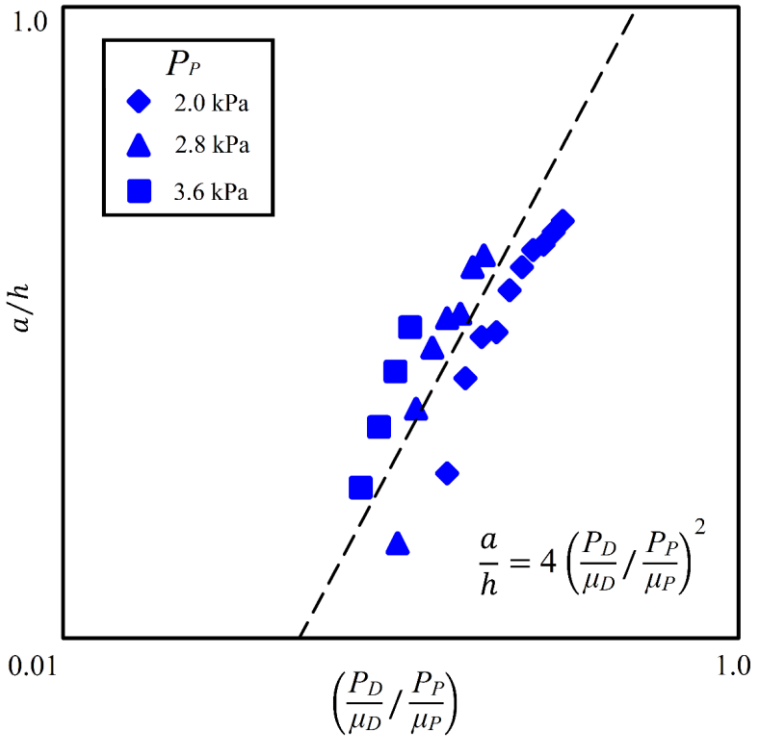

Figure 3.5: Log-log plot of dimensionless droplet diameter *a/h* vs the ratio of DEX and PEG inlet conditions. Our data appears to fit reasonably onto the line indicated by $\frac{a}{h} = 4\left(\frac{P_D}{\mu_D} / \frac{P_P}{\mu_P}\right)^2$.

Since droplet generation in our microfluidic device occurs in the jetting regime, to the system produces droplet diameters that have a larger coefficient of variation (CV) [129]. (Further details related to CV is discussed in Appendix IV). In our experiments, the droplet diameters have CV ~10 %, which is in the range of CV reported for ATPS droplet generation in the jetting regime [129]. The advantage of this system is that it produces a wide range of the droplet diameters, from 5 to 65 µm, for the column pressures used in our experiments.

Since it is difficult to precisely position microneedle in the channel for manual fabrication, we conduct a set of experiments to test the device sensitivity to the microneedle location. In these experiments, we tested three different positions of the microneedle with ~100% change of the microneedle's location and measured resultant DEX droplets' diameters. We found that this platform is insensitive to the position of the microneedle. The diameters of DEX droplets resulting

from three microneedle positions show an average percent change of ~16%. The results of these experiments are illustrated in Figure II.1 in Appendix II.

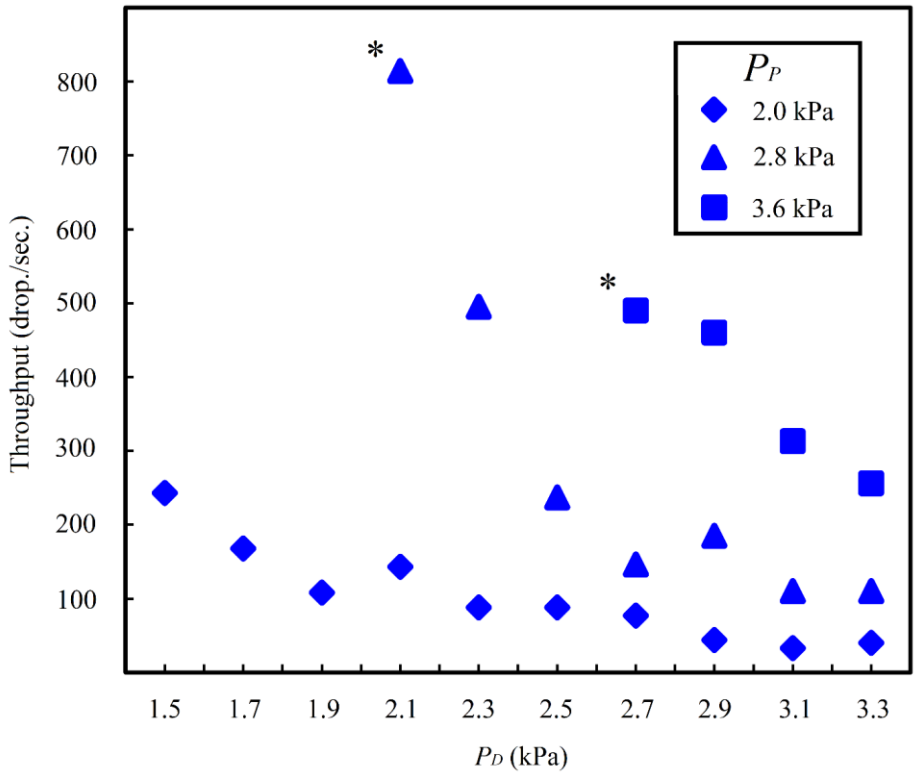

Figure 3.6: Droplet fabrication rate versus the DEX pressures (P_D) for three different PEG pressures (P_P) inside the device W/N. Diamond markers (♦) represent data points for P_P = 2.0 kPa, triangle markers (▲) shows data points for P_P = 2.8 kPa, and squares (■) indicate data points for P_P = 3.6 kPa. Elevating the column pressure of the dispersed phase flow (DEX), decreases the throughput of droplets for all three PEG heights. Data points with an asterisk (*) denote the threshold of droplet regime for the corresponding data series.

3.3.3 Droplet generation throughput

In addition to controlling the size of the droplets, we can tune the production rate of the droplets using our passive microfluidic approach. Figure 3.6 shows the throughput of the system versus the dispersed DEX phase liquid pressure, P_D, for three values of continuous PEG phase liquid pressure, P_P = 2.0, 2.8, and 3.6 kPa. Generally, the droplet generation throughput increases with decreasing P_D, and with increasing P_P. Importantly, this passive microfluidic platform, which only involves a simple modification of our previous geometry, by the insertion of a microneedle, is capable of producing water-in-water droplets up to 850 Hz.

Table 3.1: List of microfluidics and glass capillary-based techniques developed for generating ATPS droplets, along with their performance parameters.

Technique	Approach	Diameter range (µm)	Production rate (Hz)	ATPS solution
Oscillation using piezoelectric disc [151]	Active	30 to 60	~50	10% (w/v) PEG 35kDa 20% (w/v) DEX 110kDa
Mechanical vibration	Active [153]	~15	~1,000	10% (w/v) PEG 8kDa 6% (w/v) Na_2Co_3
	Active [154]	100 to 200	~10	17% (w/v) PEG 8kDa 15% (w/v) DEX 500kDa
	Active [155]	70 to 110	~20	1% (w/v) PEG 8kDa 5% (w/v) DEX 500kDa
	Active [168]	100 to 350	< 100	16% (w/v) PEG 8kDa 10% (w/v) K_3PO_4
	Active [158]	~40	~20	17% (w/v) PEG 8kDa 16% (w/v) DEX 500kDa
Pulsating inlet pressure [128]	Active	40 to 360	< 10	10% (w/v) PEG 8kDa 5% (w/v) DEX 100kDa
Pneumatic valve [169]	Active	~ 52 to 96	~13	17% & 10% (w/v) PEG 20kDa 5% & 15% (w/v) DEX 500kDa
Gravity-driven hydrostatic flow [129]	Passive	10 to 110	~15	5% (w/v) PEG 35kDa 16% (w/v) DEX 500kDa
Oil droplet choppers using syringe pumps [25]	Passive	10 to 360	~2,100	15% (w/v) PEG 8kDa 25% (w/v) DEX 40kDa
Pressure controller [170]	Passive	15 to 30	~300	10% (w/v) PEG 35kDa 16% (w/v) DEX 500kDa
Needle-assisted flow focusing (in this study)	Passive	5 to 65	850	10% (w/v) PEG 35kDa 20% (w/v) DEX 500kDa

Table 3.1 lists several active and passive techniques reported in the literature for producing water-in-water droplets, based on either microfluidic chips or glass capillary systems. For additional reference, Table II.1 in Appendix II shows a list of other active microfluidic flow focusing platforms that are used to generate water-in-oil or oil-in-water droplets. To the best of our knowledge, the throughput in our needle-assisted flow focusing technique is the highest to date,

for passive oil-free microfluidic water-in-water droplet generation (see Table 3.1). This approach is also capable of producing droplets with a wide range of droplet diameters. While the oil droplet chopper approach achieves higher throughput, it relies on the usage of an oil phase, meaning that post-processing washing processing steps are necessary for many biological applications [25]. Additionally, our needle-assisted flow focusing technique can produce small droplets down to 5 µm diameter, which could be useful for various applications, including in the biotechnology and cosmetics industries.

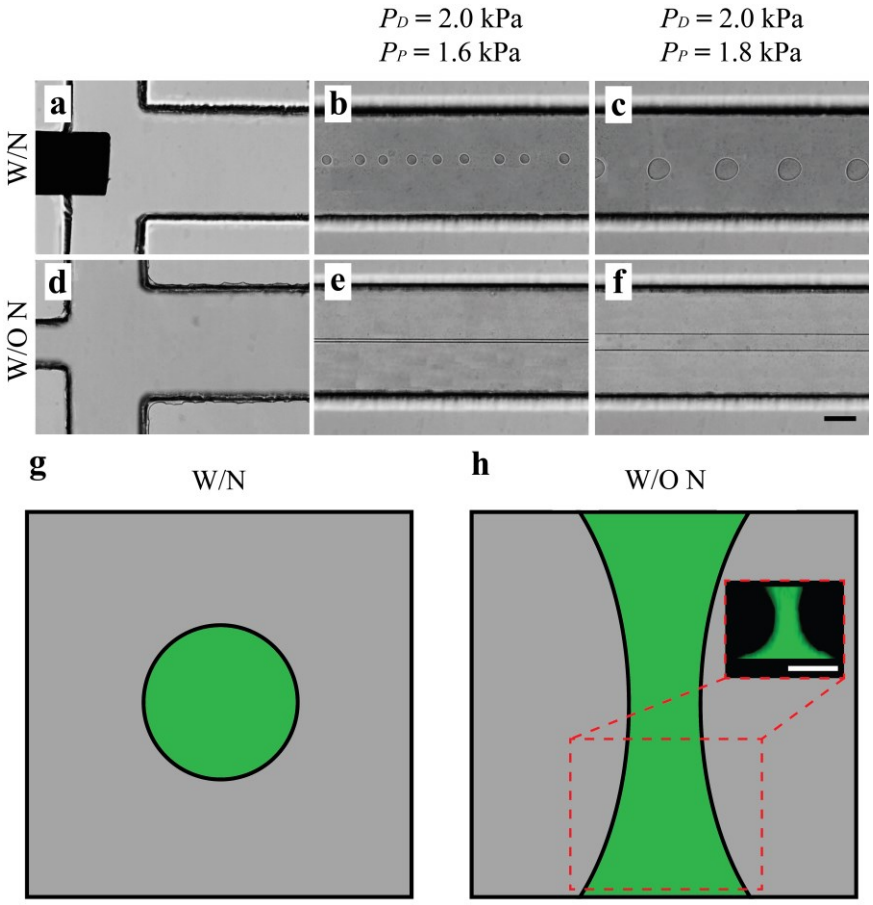

Figure 3.7: Experimental images of the microfluidic cross junction in devices (a-c) with the needle (W/N) and (d-f) without needle (W/O N), where a dispersed PEG phase flows in the continuous DEX phase. The dispersed PEG phase forms droplets in the device W/N, but not in the device W/O N, at the same hydrostatic pressures. (g) A schematic cross-sectional view of the device W/N, where the green colour indicates the disperse PEG phase, and the gray colour represents the continuous DEX phase inside the microfluidic channel. The presence of the microneedle causes the dispersed PEG phase to be isolated from the channel walls. (h) The schematic cross-sectional view for the device W/O N, illustrating that the dispersed PEG phase tends to wet the top and bottom walls, which is also evident from the

confocal microscopy inset image. Here, the confocal image shows the bottom one-third of the channel height because the confocality of the confocal microscope is 80-100 μm. Scale bars represent 100 μm.

3.3.4 Generating PEG-in-DEX droplets

Finally, it is known in the literature that in an ATPS of DEX and PEG, PEG displays stronger wetting to a glass surface than DEX [159]. This characteristic of PEG has limited the development of techniques to generate PEG droplets in a DEX continuous phase. PEG-in-DEX droplet systems may have applications where target cells or biomolecules have a higher affinity to PEG, for example in immunoaffinity of ATPS for stem cells recovery and purification [171]. A few active methods demonstrate the generation of PEG-in-DEX-in-PEG double emulsions, such as, by applying acoustic manipulations [152] and using a nozzle [172] coupled with a microfluidic chip. However, there are no reports of PEG-in-DEX droplets in microfluidics, ostensibly due to the preferential wetting of PEG to the channel walls [159], and the fact that in most geometries the disperse phase enters the microfluidic flow focusing junction in contact with the ceiling and floor of the microchannel. We thus hypothesize that our proposed approach—with the insertion of a needle that isolates the disperse phase from channel walls—can resolve this issue and generate PEG-in-DEX droplets.

Figure 3.7a and 7d illustrate the cross-junction of the devices W/N and W/O N, respectively. Figure 3.7a-c show the generation of PEG droplets in the device W/N using a constant DEX pressure P_D = 2.0 kPa, and two PEG column pressures P_P = 1.6 kPa and 1.8 kPa. Since the W/N device isolates the dispersed phase from the channel walls and 3D focuses the flow, the generation of PEG droplets in continuous DEX phase is feasible. In contrast to the device W/N, within W/O N device, the disperse phase is in contact with PDMS and the glass channel walls, and a long continuous thread of PEG forms. Figure 3.7d-f show the formation of a long continuous thread of PEG for the same column pressures in DEX continuous phase in the device W/O N. Figure 3.7g shows a representative schematic cross-sectional view of the device W/N, downstream of the cross junction. We hypothesize that the disperse PEG phase leaving the microneedle tip forms a circular cross-section, and this helps prevent the disperse phase from touching the walls—making PEG droplet generation possible. However, in the W/O N device, the dispersed PEG phase enters the cross junction and wets the top and bottom walls immediately (as shown in the schematic diagram in Figure 3.7h). The DEX flow constrains the PEG thread only from the sides. The inset of Figure

3.7h shows an experimental confocal image of the PEG phase in a device W/O N, downstream of the cross junction, and shows that the PEG phase indeed wets the floor and ceiling of the microchannel. We believe that this is the main difference between devices W/O N and W/N, which results in the ability of devices W/N to generate PEG-in-DEX droplets.

3.4 Conclusions

In this study, we present a passive microfluidic platform for water-in-water droplet generation. Our platform consists of a conventional flow focusing microfluidic device utilizing a microneedle inserted into the inlet of the disperse phase. The microneedle in our system helps prevent the disperse phase flow from touching the channel walls by confining the flow towards the center of the channel. This leads to the elimination of wetting issues between the disperse phase and the channel walls, and thus, helps the disperse phase thread break up via the Rayleigh-Plateau instability. This approach also increases the generation throughput of ATPS droplets to up to 850 Hz, which is significantly higher than that of other devices [129]. Our system is capable of producing ATPS droplets over a wide range of diameters (i.e. 4 μm to ~65 μm), with CV of about 10%, which is in line with the CV of previously reported water-in-water droplet generation methods that form droplets in a jetting regime [129].

Finally, we conduct a proof-of-concept demonstration of generating PEG droplets in a DEX continuous phase. Using PEG as the disperse phase to generate passive PEG-in-DEX droplets in a microfluidic device is challenging because PEG contacts the walls prior to the cross junction, and has a higher tendency to wet the channel walls than DEX. Our platform produces PEG-in-DEX droplets by isolating the disperse phase from contacting the channel walls. To the best of our knowledge, such passive water-in-water microfluidic generation of PEG-in-DEX droplets has not been demonstrated before.

ATPS droplet microfluidics platforms can produce droplets that have improved biological environments for cargo, like cells, compared to water-in-oil droplet systems. Therefore, this needle-assisted microfluidic ATPS droplet generation platform may be used for a variety of different biotechnological applications, such as single cell analysis and encapsulation [5], drug encapsulation and release [173], and the production of functional microparticles [174].

Chapter 4: All-aqueous double and triple emulsions

The work presented in this chapter is based on the following article published in a peer-reviewed journal *Journal of Colloid and Interface Science.*

Jeyhani, M., Theyakumaran, R., Abbasi, N., Hwang, D. K. and Tsai, S., "Microfluidic generation of all-aqueous double and triple emulsions." *Small* (2020).

Author's contribution

Niki Abbasi, a former graduate student of Prof. Tsai's lab, worked with me to conceive the idea. The microfluidic device was designed, fabricated and developed solely by me. I outlined the experimental plan and performed most of the experiments. Data analysis was done solely by me. An undergraduate research assistant, Risavarshni Theyakumaran, helped to perform some of the experiments.

4.1 Introduction

Higher order soft colloidal complex systems are widely used to generate multicompartment hydrogels, functional particles, and capsules [175]–[179]. For example, double emulsions are used for a broad range of applications in the pharmaceutical setting, such as for controlled drug release [180]–[182], and encapsulation of active ingredients such as drugs and other molecules [183], [184]. These systems are also used in cosmetics [185] and in the food industry, for encapsulation of vitamins and additives [186]–[188].

Conventional methods, such as bulk emulsification techniques [189], produce emulsions which are polydisperse. However, in many of the aforementioned applications—especially pharmaceutical applications—a narrower size distribution is required to control the function of the microcarriers [190], [191]. Microfluidic platforms enable the generation of higher-order emulsions, and engineering of complex structures within emulsions in a controllable and monodisperse fashion. Generally, two preferable types of microfluidic platforms are used to generate higher-order emulsions. One is soft lithography-based poly(dimethylsiloxane) (PDMS) microfluidic devices [192] that facilitate the fabrication of complex device layouts for advanced applications and mitigate issues for large-scale production. The other type is glass capillary systems [75] which are being used extensively to generate monodisperse double emulsions [192].

The formation of double emulsions in microfluidics requires flows of two or three immiscible fluids in precisely designed microchannels. The break-up of the droplets, in microfluidic systems, is dominated by a balance of two forces: the viscous force of the continuous phase that stretches the dispersed phase into the channel and the surface tension of the interacting fluids that tends to minimize the interfacial area [147]. In conventional double-emulsion platforms, fluids are selected to have a higher interfacial tension to assure the break-up of the droplets, and as a result, one or two of the phases are typically organic-based and the rest are aqueous [193]. In many biotechnological applications, the presence of the organic phase can be harmful due to their non-biocompatible nature. Therefore, an organic solvent-free method is desired to fabricate nontoxic emulsions for biotechnological applications.

To address the need for a biocompatible alternative, some researchers propose utilizing ATPS, to generate all-aqueous biocompatible emulsions in microfluidics [129], [152], [157]. ATPS is

formed by mixing two incompatible polymer solutions, or salt and polymer solutions, that separate into two distinct immiscible phases. Systems based on DEX and PEG are highly studied in the literature. Traditionally, these systems are used for different biotechnological applications, such as partitioning of biomolecules [140], and cell patterning [142], [194]. In recent years, techniques for microfluidically generating of water-in-water droplets are emerging using both active [128], [151], [153] and passive [34], [129] approaches. Despite these advances in generating single water-in-water droplets, there is very little work done in making higher order all-aqueous biocompatible emulsions, where one or more intermediate phases separate the innermost core from the continuous phase. Such higher order all-aqueous emulsions may facilitate the controlled release of encapsulated substances [195], and avoid cross-contamination of the phases [196]–[198]. Thus, there is a need for methods that fabricate higher order monodisperse all-aqueous emulsions.

Higher order ATPS emulsion formation is currently only achievable in microfluidics by exploiting the non-equilibrium driven phase separation inside droplets that are first generated as a single phase [152], [155]. For example, Chao *et al.* [76], generate droplets of a ternary mixture of aqueous-based solute, which are initially out-of-equilibrium. The mixture inside the droplets then phase separate to form two, three or four sub-droplets inside the main droplet. This system generates higher order ATPS emulsions, but requires an accurate selection of the initial composition of the fluid system. In addition, emulsion formation by phase separation is highly dependent on the kinetics of phase separation, which may be affected by the generation mechanism and depends upon the time-scale of phase separation. A more controllable approach may be to generate higher order emulsions using already phase separated ATPS. Yet to date, there are no published reports of microfluidically generating higher order ATPS emulsions using already phase separated ATPS.

In this manuscript, we describe a platform that overcomes the aforementioned challenges, to produce higher order emulsions based on phase separated ATPS. We show, for the first time, a PDMS-based microfluidic device, which we call a hybrid device, that can generate multiple emulsions by injecting phase separated aqueous phases using pressure pumps. We use a microneedle-assisted flow-focusing design [34] with a coaxially embedded glass capillary that is positioned downstream of the flow inlets, inside the channel, at the second flow-focusing junction. This approach facilitates the isolation of the dispersed phases from the channel walls, which

prevents wetting issues from occurring within the PDMS-based microfluidic channel, without any chemical surface treatment procedures [199]. In systems comprised of PEG and DEX phases, it is known that PEG is more hydrophobic, compared to DEX [159]. As well, in PDMS-glass based microfluidic devices that are not surface treated, the PDMS walls are more hydrophobic than glass. The surface properties of microfluidic devices can be tuned via plasma [200] or chemical treatment [201]. In conventional PDMS-glass based devices, the sheath flow may not be able to prevent contact between the dispersed phase and the channel walls. Upon contact, if the dispersed phase has a lower surface energy when in contact with the walls, compared to the sheath flow, then the dispersed phase tends to wet the walls of the device. As a result of this effect, a stable flow of dispersed phase, surrounded by the sheath flow, cannot be observed. These issues hinder the breakup of dispersed phases in the channels. Therefore, in conventional PDMS-glass devices, since both PDMS walls and PEG phase are relatively hydrophobic, the PEG phase tends to wet the walls. It is therefore challenging to form PEG droplets in a continuous phase of DEX, in conventional PDMS-glass microfluidic devices.

In our system, the dispersed phase flow is focused from all directions and isolated from the channel walls, so that the dispersed phase does not wet the walls. This approach enables the generation of PEG droplets surrounded by a continuous DEX phase, which has not been demonstrated using other microfluidic methods.

Since our approach is based on a platform made with photolithography, as opposed to fully glass capillary systems that require capillary tapering and careful alignment, our approach features better channel dimension consistency and integration for more complex layout designs in lab-on-a-chip applications, and easier parallelization [164]. The configuration of this device facilitates a controllable approach to generate higher order all-aqueous emulsions using already phase separated ATPS. Moreover, is versatile for the generation of both DEX droplets in PEG, and PEG droplets in DEX. Fabrication of PEG droplets within a DEX continuous phase may find applications for encapsulation of target cells and biomolecules that have a higher affinity to PEG, such as for immunoaffinity of ATPS for stem cells recovery and purification [171].

We first describe the design of the hybrid device, and then characterize the system by analyzing the inlet pressures which result in the formation of double emulsions. Solely adjusting the pressure imposed by the outermost phase allows for controlled tuning of the diameter and the shell thickness

of the double emulsions. We investigate the effect of applying a sinusoidal pressure wave function on the outermost phase and observe the changes in diameter and shell thickness of the double emulsions for various wave amplitudes. In addition, we study the effect of constant amplitude waves, with various periods, on the diameter and shell thickness of the double emulsions, as well as their inter-droplet distances. Then, we demonstrate that the volume of the fabricated double emulsions can be tuned by disrupting the system's equilibrium. Finally, we show that this technique can be applied to generate triple emulsions. We anticipate that this platform will be useful in various biotechnological applications, such as the delivery of bioactive agents [186], [202], cell transplantation [203], and for modeling cellular processes such as cellular phase separation [204], [205].

4.2 Experimental methods

4.2.1 Chemical preparation

The ATPS solutions we use is composed of a mixture of PEG (M_w: 35 kDa, Sigma-Aldrich, St. Louis, MI, USA) and DEX (M_w: 500 kDa, Pharmacosmos, Holbaek, Denmark). To prepare the ATPS solutions, we follow the protocol in the literature [38]. We prepare three different sets of ATPSs (Table 4.1) by centrifuging (Sorvall Legend RT, Germany) the mixture of DEX and PEG phases at 1,400 RPM for 1.5 hours. Then PEG-rich and DEX-rich phases are separated extracted by using a serological pipette.

Table 4.1**:** Concentration of stock solutions and equilibrated PEG-rich and DEX-rich phases.

ATPS	Stock Solution		PEG-rich Phase		DEX-rich Phase	
	PEG % (w/v)	DEX % (w/v)	PEG % (w/w)	DEX % (w/w)	PEG % (w/w)	DEX % (w/w)
1	10	12.8	7.489	0.817	0.001	16.106
2	20	25.6	14.857	1.573	0.001	29.943
3	**5**	6.4	3.158	1.570	0.724	7.139

* *Note*: Interfacial tensions adopted from Atefi *et al*., 2014[38]

Physical properties of all five sets of ATPS illustrated in Table 4.2. The viscosity of each of the phase-separated solutions of DEX and PEG is found at ambient temperature of 23 ± 1 °C using a stress controlled rheometer (Physica MCR 301, Anton Paar, Graz, Austria) equipped with double-gap measuring system (Standard measuring system DG26.7/T200/AL), as a function of shear rate. To carry out the viscosity measurements, about 8 ml of each solution is used and the viscosity is monitored with changes in shear rate (see Figure III.1, Appendix III for more details). For shrinking and expanding the double emulsions, we select two different ATPSs, ATPS 2, and ATPS 3 from Table 4.1, respectively and DEX-rich phase of each system extracted to be used for each experiment, as the outer most continuous phase. We filter all the phases prior to use by passing through a PTFE syringe filter with pore size of 3 μm (Tisch Scientific, OH, USA) to remove particulates and impurities.

Table 4.2: Physical properties of three different ATPSs are used in the experiments.

ATPS	Viscosity, μ (mPa.s)		Density, ρ (g/cm^3)		Interfacial Tension, γ (mN/m)
	PEG-rich Phase	DEX-rich Phase	PEG-rich Phase	DEX-rich Phase	
1	14.70 ± 0.02	85.06 ± 1.60	1.01	1.06	0.082 ± 0.001*
2	83.61 ± 0.10	696.21 ± 5.30	1.03	1.13	0.381 ± 0.006*
3	4.99 ± 0.04	14.35 ± 0.07	1.01	1.03	0.012 ± 0.001*

* *Note*: Interfacial tensions adopted from Atefi *et al*., 2014[38]

4.2.2 Device Fabrication

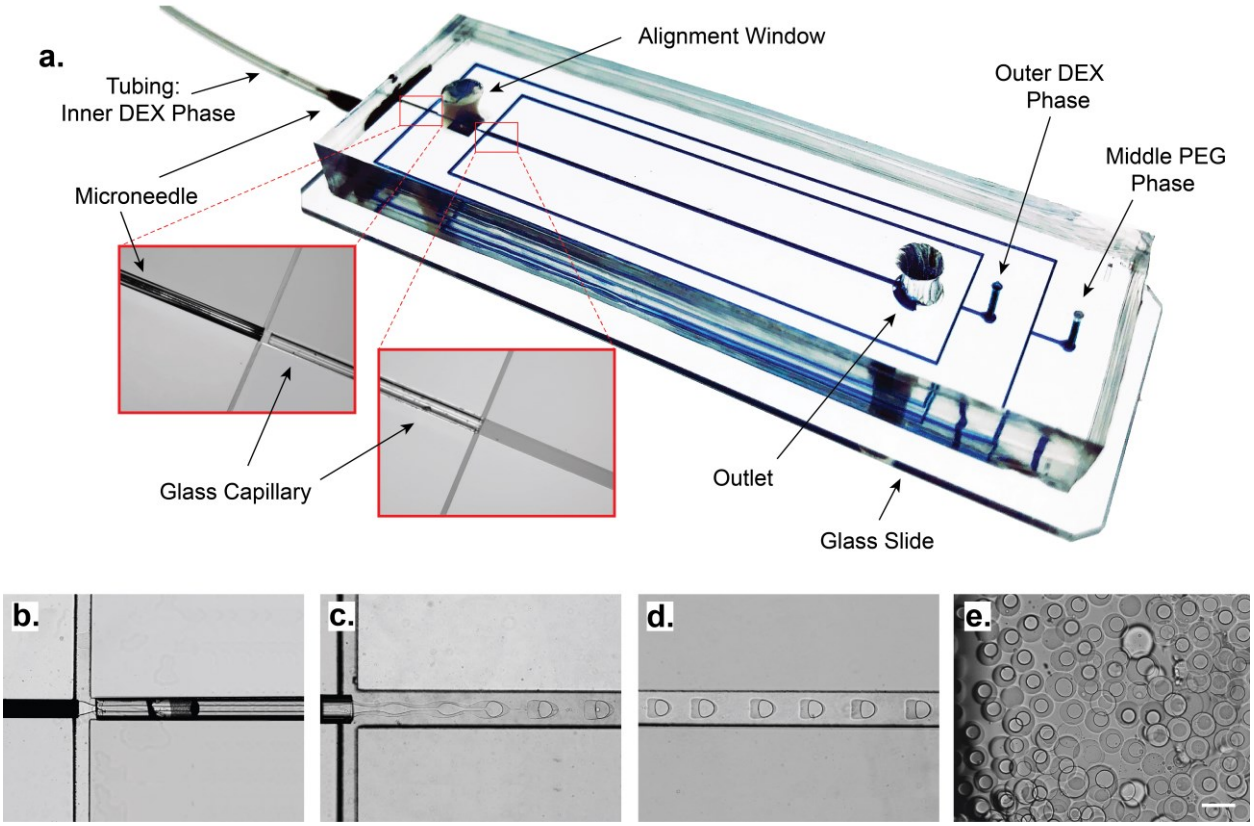

Figure 4.1: a) Schematic diagram of the hybrid device, composed of a microneedle in the first inlet and an embedded glass capillary inside the microchannel between the first and second cross-junction, for double emulsions formation. b) First cross-junction in which the inner DEX phase flows through the microneedle and the middle PEG phase flows through the glass capillary. c) The two concentric phases arrive at the second cross-junction from the glass capillary. The outer DEX phase causes the ATPS jet to breakup to double emulsions via a Rayleigh–Plateau instability. d) Double emulsions form inside the microchannel. e) Emulsions collet in a reservoir downstream the channel. The scale bar represents 300 µm.

Microfluidic devices are fabricated based on the standard soft lithography method [164]. As seen in Figure 4.1a, the microfluidic device for double emulsion formation is a flow-focusing device with two junctions. It is comprised of three inlets for the dispersed phase, continuous phase, and outermost continuous phase, and one outlet. The widths of the channels for the dispersed phase and two continuous phases are 100 and 150 µm, respectively. The width of the channel leaving the first cross-junction to the second cross-junction is 200 µm, and the width of the channel downstream after the second cross-junction is 300 µm. The height of all channels is 400 µm.

In order to fabricate triple emulsions, and shrink and expand double emulsions, we fabricate another device identical to the device for double emulsion formation, but with four inlets and three cross-junctions. The width of the channel downstream of the last cross-junction is 450 μm, and the remainder of the dimensions are similar to those of the double emulsion device.

We design the layout of microchannels using SolidWorks 2016 (Dassault Systèmes, Waltham, MA, USA) and print a photomask on a transparency sheet (25400 dpi, CAD/Art Services Inc., Bandon, OR, USA). Then, we construct the channel features on a 4-inch diameter silicon wafer (UniversityWafer Inc., Boston, MA, USA). After spin-coating SU-8 2150 photoresist (MicroChem, Newton, MA, USA) on the wafer, we expose the wafer to UV light through the photomask. Finally, we dissolve the wafer in a developer solution (MicroChem, Newton, MA, USA) to remove the unexposed photoresist.

We prepare the microfluidic chip by pouring a 10:1 ratio mixture of PDMS resin to curing agent (Sylgard 184, Dow Corning, Midland, MI, USA) onto the silicon master mold and leave it in an oven for 2 hours to cure, at 70°C. Then, the PDMS slab is removed from the wafer, and using a 1-mm diameter biopsy puncher (Integra Miltex, Inc., Rietheim-Weilheim, Germany) all the inlets are made. After that, we use a 4-mm biopsy puncher to punch a hole for the outlet and another hole as the alignment window (Figure 4.1a) to adjust the glass capillary vertically, within the channel.

To fabricate the hybrid device, we modify the chip to coaxially focus the flows in a three-dimensional configuration and isolate dispersed phases from the channel walls [34]. To do so, we first cut a a cylindrical glass capillary (I.D. = 150 μm, O.D. = 250 μm; Whale Apparatus, Hellertown, PA, USA) to a length of 7 mm, using a ceramic tile (Shutter Instrument Co., Novato, CA, USA). The glass capillary is manually inserted inside the channel between two cross-junctions. In order to generate triple emulsions, we use the device with four inlets and insert another glass capillary (I.D. = 300 μm, O.D. = 400 μm; Whale Apparatus, Hellertown, PA, USA) with the same length of the first one between the second and third cross-junctions. For the shrinking and expanding experiments, we use the same device with four inlets, but we insert the glass capillary with I.D. = 150 μm and O.D. = 250 μm between the first and the second cross-junction.

After cleaning a glass slide (VWR International 76 × 26 mm Plain Microscope Slides, PA, USA), we stick three layers of tape (3M, St. Paul, MN, USA) on it and cut a frame of the same size as the

alignment window on the tape, and peel off the reminder of the tape and leave the small frame. This allows us to adjust the position of the glass capillary vertically to the center of the channel by elevating the glass capillary for 60 μm from the bottom of the channel. We use oxygen plasma treatment (Harrick Plasma, Ithaca, NY, USA) to bond the PDMS slab and the glass slide irreversibly. After the bonding the PDMS and glass slide, we insert the glass capillary, through the alignment window, to sit over the layers of the tape and properly align it and filled the window with silicone sealant (General Electric, Boston, MA, USA). After that, we cut the PDMS slab at the dispersed phase inlet and stick four layers of tape underneath the microneedle to elevate it and obtain an 80 μm gap between the needle and the glass slide. Finally, we insert a metallic microneedle (34G; I.D. = 100 μm, O.D. = 200 μm; Japan Bio Products, Tokyo, Japan) through the channel to reach the first cross-junction. We inspect proper alignment of the glass capillary and the microneedle under a stereomicroscope (E-Zoom 6 V, Edmund Optics Inc., Barrington, NJ, USA). To secure the microneedle in the place and seal it, we bond it to the glass slide and the PDMS slab using two-component epoxy glue (ALUMFAST®, HY-POXY® Systems, Inc., SC, USA) and connect a tubing (Saint-Gobain, Malvern, PA, USA) to the needle using the same epoxy glue.

In our device, we choose to use a metallic microneedle as the first conduit, followed by a glass capillary as the second conduit. Here, part of the first conduit is outside of the main device, so the metallic microneedle is used because of its resistance to breaking. A glass capillary is used as the second conduit because of the ease of cutting glass capillaries into desired sizes.

4.2.3 Microfluidic setup

All the flows are injected into the microfluidic device through PEEK tubing (O.D. = 1/16”, I.D. = 0.020”; IDEX Health and Science), using a microfluidic flow control system (FLOW EZ™, Fluigent, Paris, France), and are controlled by a Microfluidic Automation Tool software (Fluigent, Paris, France). Experimental images and videos are captured using a high-speed camera (Miro M110, Vision Research, Wayne, NJ, USA) connected to an inverted brightfield optical microscope (Axio Observer A1, Carl Zeiss, Oberkochen, Germany).

4.2.4 Preparation of lysozyme

The ultralow interfacial tension of ATPS limits the adsorption of surface-active species at the interface and this adsorbtion effect is strongly depreciated which lowers the free energy of the interface, and hinders the practical stabilization of ATPS emulsions [206]. In order to stabilize the double emulsions collected in the outlet (Figure 4.1e), we follow a protocol in ref. [206]. that successfully stabilizes ATPS emulsions. In this protocol protein fibrils used with strong interface affinity and high aspect ratio to have higher surface coverage. The protein fibrils used in this protocol have strong interface affinity and they prepared

Using this method, to prevent coalescence of double emulsions we add 2 % (v/v) lysozyme from hen egg whites (Sigma Aldrich, St. Louis, MO, USA) to all ATPS phases. To prepare the stock solution of lysozyme, we mix 0.1 % (w/v) lysozyme in deionized water and mix the solution using a vortex mixer. Then the solution is left in an oven at 70 °C for 5 days.

4.3 Results and discussion

4.3.1 Formation of double emulsions

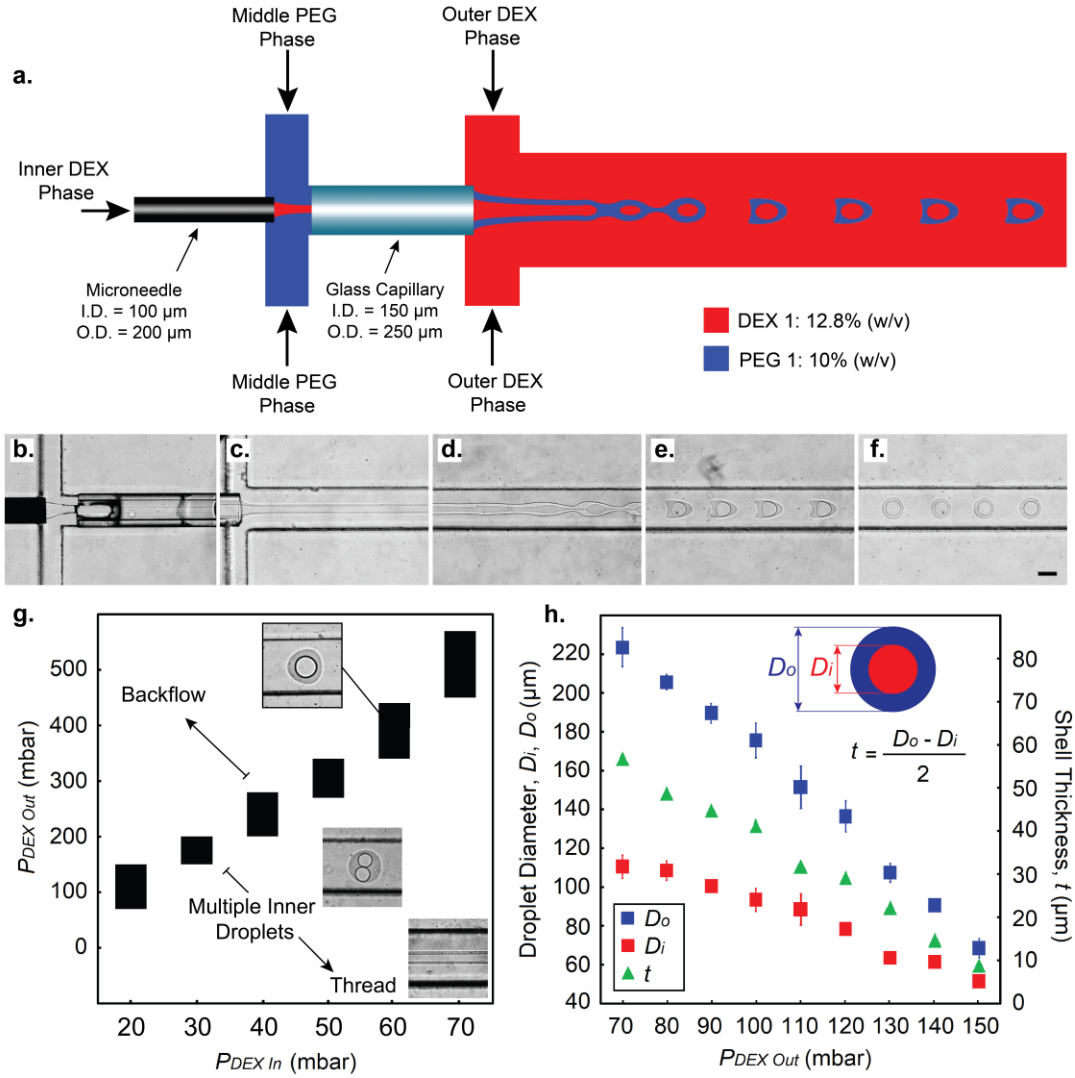

Figure 4.2: a) Schematic diagram of the hybrid device for producing double emulsions. The inner DEX phase is introduced via the microneedle, and meets the middle PEG phase at the first junction. The co-flowing phases flow into the glass capillary as a thread. The outer DEX phase is introduced at the second cross-junction. Here, the thread formed by co-flowing inner DEX and middle PEG phases breakup into emulsions due to the Rayleigh-Plateau instability. b-f) Experimental images of double emulsion formation in different locations inside the microchannel. g) A phase diagram illustrates the pressure ranges, indicated with solid bars, in which double emulsions form. Here, the constant pressure ratio $P_{PEG\ Mid} / P_{DEX\ In} = 1/2$. Higher values of $P_{DEX\ Out}$, above the solid bars, lead to backflow, and lower values result in double emulsions that have two or more droplets encapsulated in a bigger droplet. Further decreases in $P_{DEX\ Out}$ lead to the formation of long threads. h) A plot of inner droplet diameter D_i, outer diameter D_o,

and shell thickness t, versus the outer DEX phase pressure, $P_{DEX\ Out}$. Here, inner DEX and middle PEG pressures are $P_{DEX\ In}$ = 20 mbar and $P_{PEG\ Mid}$ = 10 mbar, respectively. All error bars corresponded to ±1 standard deviations in a sample size of ten emulsions (some statistical errors are smaller than the symbol size). See Table III.1, Appendix III for statistical analysis. Scale bar represents 150 μm.

Figure 4.2a shows a schematic diagram of the hybrid microfluidic device, and the polymer phases introduced through the inlets to form double emulsions. In this experiment, the working fluid is ATPS 1 from Table 4.1, which phase separates into the PEG-rich phase, PEG 1, and the DEX-rich phase, DEX 1, with equilibrium concentration values indicated in Table 4.1. We introduce DEX 1, PEG 1, and DEX 1 through the Inner DEX Phase, Middle PEG Phase, and Outer DEX Phase inlets, respectively, to form double emulsions (shown in Figure 4.2a).

The breakup of liquid threads, including in microfluidic systems, is typically described by the Rayleigh-Plateau instability [152], [205] Qualitatively speaking, increasing the continuous phase pressure, for example the outer DEX phase pressure for our double emulsion generation experiments, reduces the unperturbed radius of the thread coming out of the flow focusing junction. Therefore, if the other two pressures, $P_{DEX\ In}$ and $P_{PEG\ Mid}$, are constant, this reduction of the unperturbed thread radius leads to earlier thread breakup into emulsions. This qualitative explanation is consistent with our experimental observations that higher continuous phase pressure leads to emulsion generation, and lower continuous phase pressure results in thread formation (Figure 4.2g). Figures 4.2b-4.2f show experimental microscope images of our double emulsion generation experiment in different stages. Figure 4.2b shows the first cross-junction, where the inner DEX phase, DEX 1, flows out of the microneedle and is flow focused by the middle PEG phase, PEG 1, to form a thread. The DEX 1 thread, cladded by PEG 1, flows through the glass capillary, and enters the second junction where it is cladded by the outer DEX phase flow, DEX 1. Downstream of the second junction, the outer DEX phase co-flows with the concentric cylindrical threads of the inner and middle phases (Figure 4.2c). Further downstream, the interfaces of the inner and middle phase threads begin to exhibit perturbations (Figure 4.2d). This finally leads to the pinch-off of the concentric cylindrical threads into bullet-like shape double emulsions (Figure 4.2e). We note that the double emulsions only appear bullet-like in the microfluidic flow, due to shear stresses imposed by the flow. Once the flow is stopped, the double emulsions relax to a spherical shape (Figure 4.2f). We define experimental results as thread

formation (see for example, Figure 4.2g) when breakup occurs beyond 4 mm past the second flow focusing junction. We regard breakup before 4 mm to be results of emulsion generation.

Figure 4.2g represents a phase diagram that indicates when double emulsions are generated under different inner DEX phase pressure, $P_{DEX\,In}$, and outer DEX phase pressure, $P_{DEX\,Out}$. Here, we fix the ratio of the middle PEG phase pressure, $P_{PEG\,Mid}$, to the inner DEX phase pressure, $P_{DEX\,In}$, such that $P_{PEG\,Mid} / P_{DEX\,In} = 1/2$. We observed experimentaly that for this ratio we are able to explore the widest range of double emulsion formation within our time constraints. We find that high values of $P_{DEX\,Out}$ lead to backflow of the inner and middle phases. At low values of $P_{DEX\,Out}$, double emulsions with two or more inner droplets form. Lowering $P_{DEX\,Out}$ further results in the formation of a long thread inside the channel. In the pressure ranges indicated by solid bars in Figure 4.2g, the breakup of the threads leads to emulsion suspensions with more than 95 % being double emulsions. (images from other experimental conditions in Figure III.2). The size of the emulsions appears to depend on the magnitude of the shearing force supplied by the sheath flow. Increasing the sheath flow pressure causes the thread to have a smaller radius before breakup as described in the paragraph above, and thus decreases the size of the generated droplets. For double emulsion generation, the size of the shell PEG layer, and the core DEX droplet, can be tuned by controlling the pressure of the outer DEX phase, $P_{DEX\,Out}$. Increasing $P_{DEX\,Out}$ similarly results in a higher shear force, and the formation of smaller PEG compartments with smaller DEX droplets within (see Figure 4.2h). The same explanation could be extended to the case of triple emulsion generation. In this approach, we use pressure pumps as the infusion mechanism. Constant flow rate syringe pumps, which control the flow velocity, can also be used. We describe the relationship between pressure and flow velocity in Appendix III.

We also investigate how the inner and outer diameter, D_i and D_o, respectively, of the double emulsions, change with varying values of $P_{DEX\,Out}$ while $P_{DEX\,In}$ and $P_{PEG\,Mid}$ are kept constant. We report the resulting shell thickness, $t = \frac{Do-Di}{2}$. Namely, Figure 4.2h illustrates the effect of changing $P_{DEX\,Out}$ for constant inner DEX and middle PEG pressures, $P_{DEX\,In}$ = 20 mbar and $P_{PEG\,Mid}$ = 10 mbar, respectively. We note that increasing $P_{DEX\,Out}$ increases the viscous shear force applied on the thread, resulting in decreases of the size of the concentric flows and ultimately, leads to the formation of smaller droplets, and lower values of the shell thickness, t. The double

emulsions are produced in a jetting regime, with an average inner droplet diameter coefficient of variation, CV_i = 5 %, and outer droplet diameter coefficient of variation, CV_o = 6 %.

4.3.2 Controlling the shell thickness

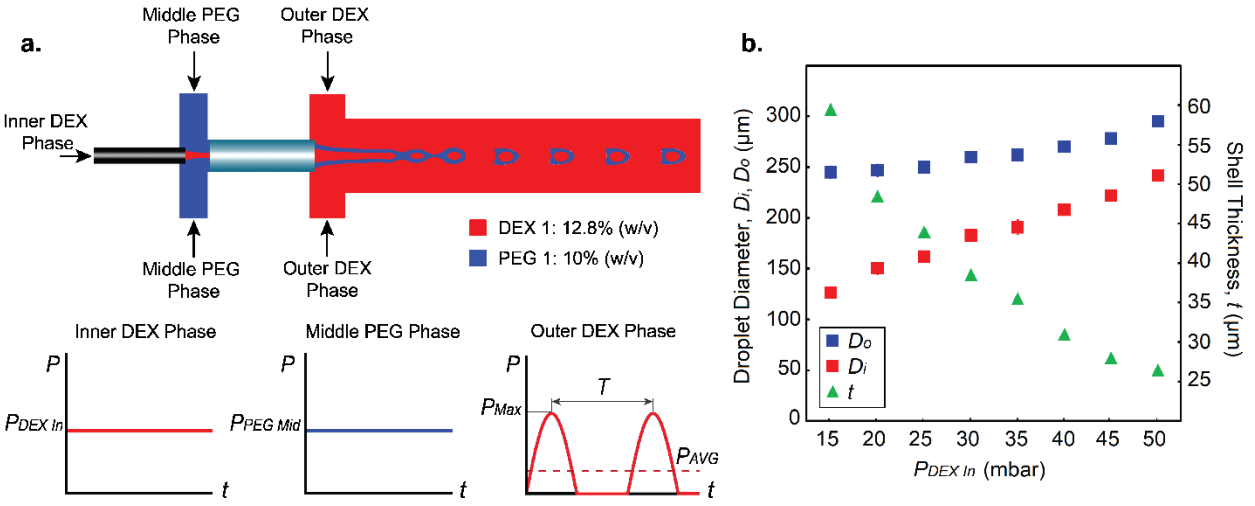

Figure 4.3: Inner and outer droplet diameters, D_i, and D_o, respectively, and shell thickness, t, versus the inner DEX phase pressure, $P_{DEX\ In}$. Here, the outer DEX phase pressure follows a half-wave rectified sinusoidal waveform with amplitude, P_{Max} = 300 mbar and period T = 500 ms. All error bars corresponded to ±1 standard deviations in a sample size of ten emulsions (some statistical errors are smaller than the symbol size). See Table III.2, Appendix III for statistical analysis.

The shell thickness of double emulsions is an important parameter for many applications, for example in drug delivery, where it is important to tune the shell thickness to control the release profiles of encapsulated drugs efficiently [199], [207]. To control the shell thickness, we vary the inner DEX phase pressure, $P_{DEX\ In}$ = 15 – 50 mbar, while maintaining a constant middle PEG phase pressure, $P_{PEG\ Mid}$ = 10 mbar. We then apply a sinusoidal wave function for the outer phase pressure $P_{DEX\ Out}$, where we adjust the amplitude, P_{Max}, and the period, T, of the generated pressure waves. Specifically, we use a half-wave rectified sinusoidal waveform for the pressure $P_{DEX\ Out}$. We set the wave amplitude P_{Max} = 300 mbar and the period T = 500 ms (Figure 4.3a), and Figure 4.3b shows the resulting plot of droplet diameters D_i, and D_o, and shell thickness t versus constant values of $P_{DEX\ In}$. The applied sinusoidal waveform perturbs the dispersed phase at the second flow focusing junction, resulting in the formation of double emulsions based on the set period, T, of the waveform. Since the period of the sinusoidal waveform is constant, increasing the pressure of the inner DEX phase leads to an increase in the volume of the dispensed inner DEX phase and thus

the size of the inner droplet increases for each breakup (see Figure 4.3b). The inner and outer droplet diameters increase approximately linearly with $P_{DEX\ in}$, and the shell thickness t decreases. As shown in Figure 4.3b, increasing $P_{DEX\ In}$ from 15 to 50 mbar results in almost doubling of the inner diameter D_i = 26 – 242 µm, while D_o changes only about 20 %, D_o = 245 – 295 µm.

4.3.3 Controlling the distance between double emulsions

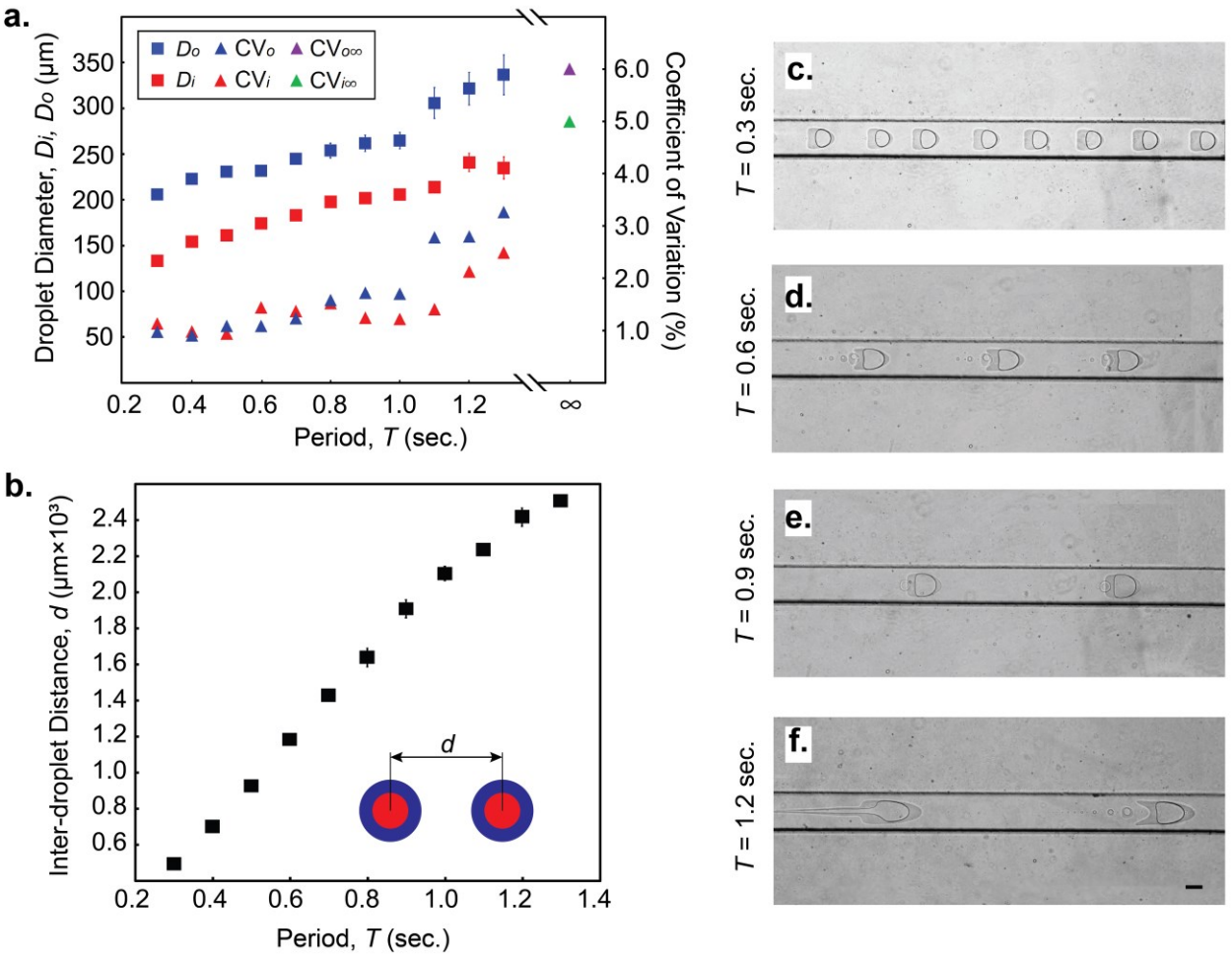

Figure 4.4: a) Plot of inner and outer droplet diameter, D_i and D_o, and coefficients of variation of the inner and outer droplet diameters, CV_i and CV_o, versus the period T. Here, inner DEX and middle PEG pressures $P_{DEX\ In}$ = 25 mbar and $P_{PEG\ Mid}$ = 10 mbar, respectively; and the outer DEX phase pressure, $P_{DEX\ Out}$, follows a half-wave rectified sinusoidal waveform with amplitude, P_{Max} = 300 mbar and a range of periods, T = 0.3 – 1.3 seconds. b) Changes of inter-droplet distance, d, versus a range of periods. c-f) Experimental images illustrating the increase of the inter-droplet distance for T = 0.3, 0.6, 0.9, and 1.2 seconds. All error bars corresponded to ±1 standard deviations in a sample size of ten emulsions (some statistical errors are smaller than the symbol size). See Tables III.3 and III.4, Appendix III for statistical analysis. Scale bar represents 150 µm.

The control of inter-emulsion distance is also important [208], because this distance can prevent or promote the coalescence of consecutive emulsions [209]. To control the distance between the double emulsions, we use the previous configuration—constant pressures for the inner and middle phase inlets, and a half-wave rectified sinusoidal wave function for the outer phase inlet. We fix $P_{DEX\ In}$ = 25 mbar, $P_{PEG\ Mid}$ = 10 mbar, and a half-wave rectified sinusoidal wave function for $P_{DEX\ Out}$ with an amplitude P_{Max} = 300 mbar, and a range of periods, T = 300 – 1,300 ms (Figure 4.4).

Figure 4.4a is a plot of the inner and outer phase droplet diameters, D_i and D_o, respectively, and the associated coefficients of variation, CV_i and CV_o, versus changing period T. Increasing the period T, of the sinusoidal pressure $P_{DEX\ Out}$, results in higher volumes of the middle PEG phase, dispensed, before the breakup happens, which leads to approximately 63 % increase in D_o. Moreover, the increase in period of the sinusoidal function induces a higher inner DEX phase flowrate, increasing D_i by 80 %.

Importantly, we also observe that decreasing the period T results in significantly lowering CV for both inner and outer phases diameters, CV_i and CV_o, respectively. Within the tested range of periods T, we obtain values of CV_i and CV_o down to approximately 1 % (Figure 4.4a), which is comparable to the CV reported in water-oil double emulsion systems [210]. Conversely, as the period $T \rightarrow \infty$ —that is, at constant pressures—the CV increases to more than 5 %.

Figure 4.4b represents the inter-droplet distance, d, versus the wave period, T, imposed on the outer DEX phase. Increasing the period of the sinusoidal wave, from T = 300 – 1,300 ms, increases the size of the generated double emulsions by 60 – 80 %. However, same changes of period T result in a much more significant changes in the inter-droplet distance, d. d increases by about 430 % (from d = 460 – 2,470 μm) when the period is increased from T = 300 - 1,300 ms. Increasing the period of the sinusoidal wave for the outer DEX phase allows a longer time for the inner DEX and middle PEG phase to dispense and enter the second junction. This effectively allows for a larger volume of the inner DEX and middle PEG phases to enter the second junction. As a result, larger emulsions are produced. Since the breakup of the jet is controlled by the period of the wave, increasing the period results in an increase of the distance, d, between two consecutive emulsions (see Figure 4.4b). Figures 4.4c-4.4f show experimental images of double emulsions inside the microchannel for T = 300 – 1300 ms.

4.3.4 Formation of triple emulsions

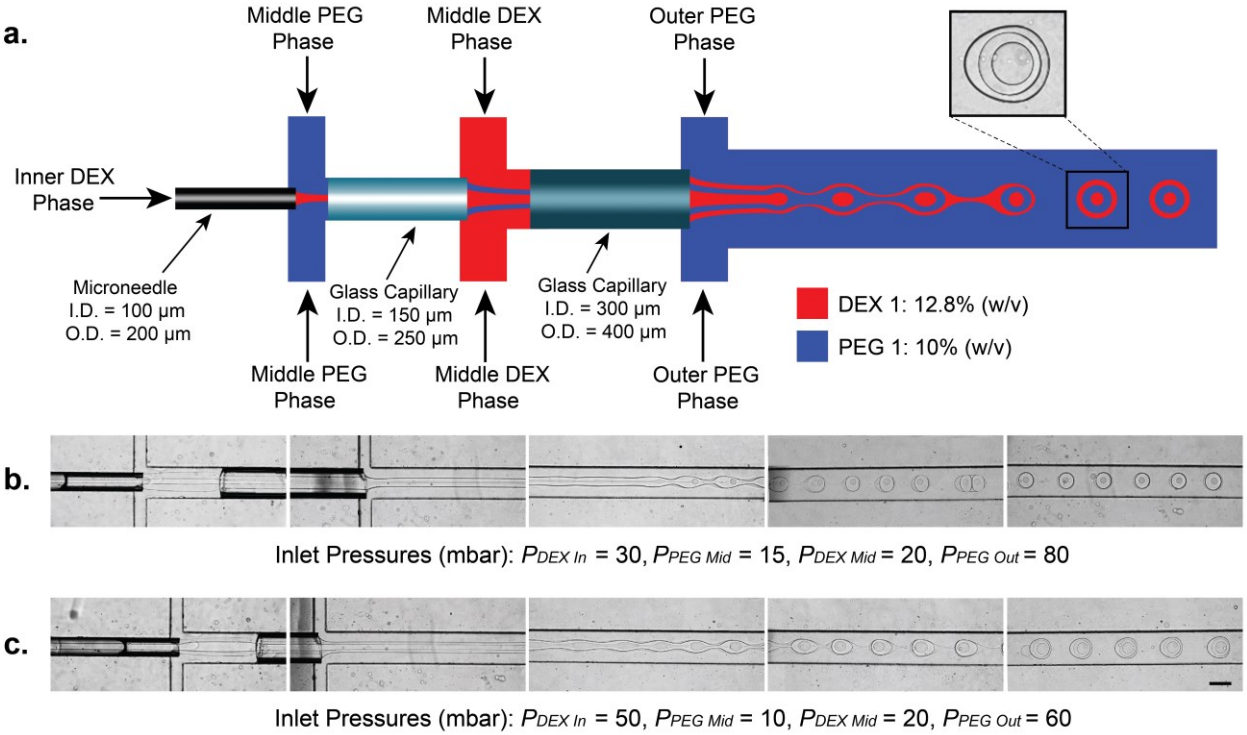

Figure 4.5: a) Schematic diagram of the hybrid device for generating triple emulsions. The inner DEX phase is introduced through the microneedle, and meets the middle PEG phase at the first junction. Then both phases flow into the first glass capillary as a thread. The middle DEX phase is introduced at the second cross-junction, where the inner DEX and middle PEG phases flow into the second glass capillary as a thread. The outer PEG phase is introduced at the third cross-junction. Here, the thread formed by co-flowing inner DEX phase, middle PEG phase, and middle DEX phase breaks up into triple emulsions due to the Rayleigh-Plateau instability. b-c) Experimental images of triple emulsions formed in different locations, for two different inlet pressure conditions. Scale bar represents 300 µm.

To fabricate triple emulsions, we utilize a device with four inlets, and two glass capillaries. We use ATPS 1 for this set of experiments, and introduce the DEX-rich phase, DEX 1, to the device through the Inner DEX Phase and Middle DEX Phase inlets (Figure 4.5a). The PEG-rich phase, PEG 1, flows through the Middle PEG Phase and Outer PEG Phase inlets (Figure 4.5a).

In this set of experiments, we apply constant pressures to the inlets. Figure 4.5b shows experimental images of triple emulsion formation in different stages: at the first junction, where the inner DEX phase forms a thread; at the second junction, where a concentric cylindrical thread is formed of the inner DEX phase cladded by the middle PEG phase; at the third junction, where the inner DEX phase, middle PEG phase, and middle DEX phase form a concentric cylindrical

thread that begins to experience interfacial perturbations; downstream of the third junction, where triple water-in-water-in-water-in-water emulsions form. In contrast to the double-emulsion formation experiments, we observe triple emulsions maintaining their round shape as they flow downstream in the microchannel. In Figure 4.5b we set the inlet pressures to $P_{DEX\,In}$ = 30, $P_{PEG\,Mid}$ = 15, $P_{DEX\,Mid}$ = 20, and $P_{PEG\,Out}$ = 80 mbar. Figure 4.5c illustrates the generation of larger triple emulsions, the inlet pressures are $P_{DEX\,In}$ = 50, $P_{PEG\,Mid}$ = 10, $P_{DEX\,Mid}$ = 20, and $P_{PEG\,Out}$ = 60 mbar.

4.3.5 Shrinking and expanding emulsions

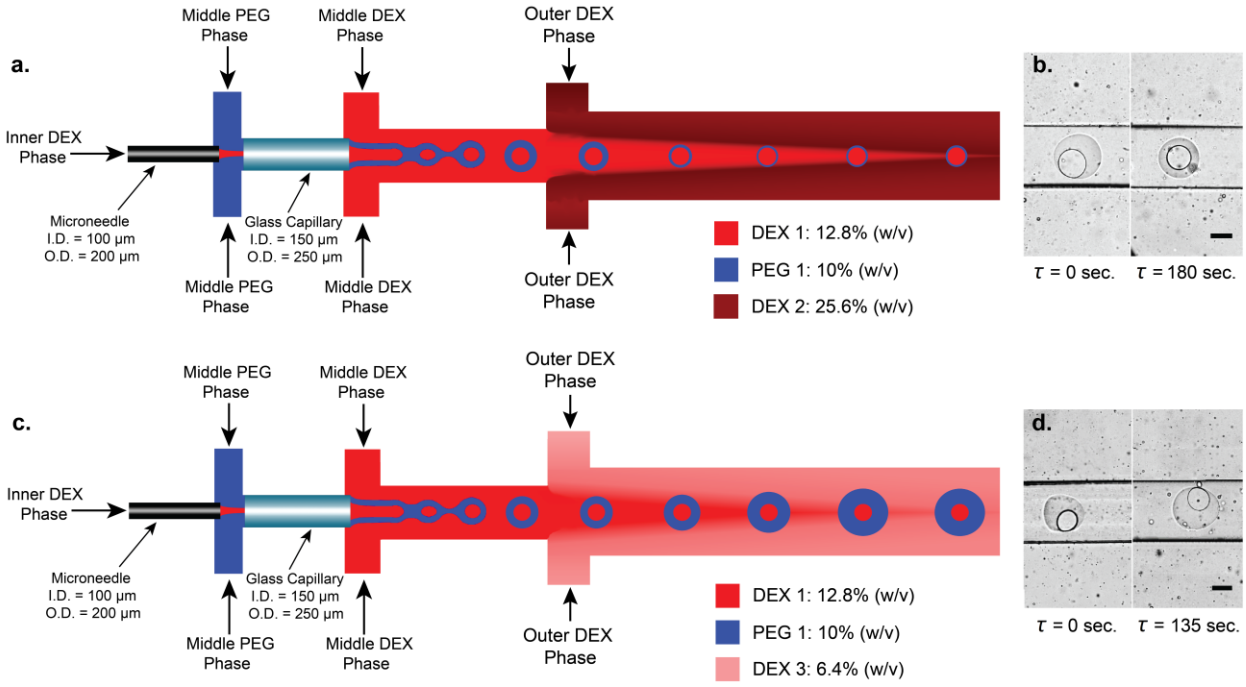

Figure 4.6: Shrinking and expanding the volume of double emulsions. a) Schematic of the hybrid device shown from the third cross-junction. Introducing a higher concentration phase, DEX 2, as the outer DEX phase triggers a non-equilibrium which ultimately, results in water transfer from the PEG phase to its surrounding phase. b) Time-series images of a double-emulsion flowing downstream in the channel and shrinking with time. c) Schematic of the setup for expanding the volume of the double emulsion. Introducing a lower concentration of the outer DEX phase, DEX 3, leads to a water exchange between the PEG phase and the surrounding DEX phase and ultimately results in water transfer from the continuous phase to the PEG phase. d) Time-series of images of a double emulsion growing downstream in the channel. Scale bars represent 150 µm.

Introducing a new aqueous phase that is out-of-equilibrium with the other aqueous phases in the microchannel, triggers a re-equilibrium process inside the microchannel. During the re-equilibrium process, there is an exchange of water molecules, alongside the polymer molecules, between the

phases. Recently, our group demonstrated the dynamic control of ATPS-based droplets by shrinking and growing DEX-in-PEG droplets [157]. Here, we demonstrate the proof-of-concept shrinking and growing of double emulsions using the same method. In order to shrink or expand the volume of the double emulsions, we modify triple emulsion generation microfluidic device, to include a long serpentine channel downstream of the third cross-junction. We embed one glass capillary (I.D. = 150 μm, O.D. = 250 μm) between the first and the second cross-junctions to form double emulsions, and we do not embed a capillary between the second and third cross-junctions.

We use ATPS 1 to form double emulsions by introducing DEX 1 through the Inner DEX Phase and Middle DEX Phase inlets, and PEG 1 through the Middle PEG Phase inlet (Figure 4.6a). Through the Outer DEX Phase inlet, we introduce another DEX phase which has a different polymer concentration than DEX 1 (Figure 4.6a). Specifically, at the Outer DEX Phase inlet, we introduce a DEX phase that is different from DEX 1, so that the entire fluid system goes out-of-equilibrium at the third cross-junction. The re-equilibrium process downstream of the third cross-junction forces the double emulsion to exchange water content with the continuous phase until a new equilibrium is achieved [157]. To shrink the fabricated double emulsions, we use a 29.943 % (w/w) DEX-rich phase, called DEX 2 of ATPS 2 in Table 4.1, as the Outer DEX Phase. This higher concentration DEX phase causes a re-equilibrium of the double emulsion that shrinks the double emulsion (Figure 4.6a). Figure 4.6b shows experimental images of a double-emulsion before entering the third cross-junction (τ = 0 sec.), and after it travels downstream inside the serpentine channel (τ = 180 sec.). We measure 34 % and 37 % decreases in droplet volume, for the outer and inner droplets, respectively, during the re-equilibrium process.

We also perform a reverse process to increase the size of the double emulsions. Here, we use a 7.139 % (w/w) DEX-rich phase, called DEX 3 of ATPS 3 in Table 4.1, as the Outer DEX Phase (Figure 4.6c). DEX 3 has a lower polymer concentration than DEX 1. Figure 4.6c shows the schematic diagram of double emulsion expansion during re-equilibrium. Figure 4.6d shows images of a double-emulsion that experiences 40 % and 31 % increases in outer and inner droplet volume as the system re-equilibriates.

4.4 Conclusions

In this work, we describe a microfluidic platform for the generation of all-aqueous double and triple emulsions based on ATPS. Our platform consists of a conventional multi cross-junction flow-focusing device, with a microneedle inserted into the first inlet [34] followed by the embedding of one or two glass capillaries inside the microchannel between different cross-junctions. The glass capillaries help to prevent wetting of the microchannel walls by the disperse phases.

This hybrid device setup enables the controlled generation of double and triple emulsions, based on equilibrated ATPS, which is differentiated from previously reported ATPS double emulsion microfluidic systems [76], [155]. We demonstrate the potential of this platform to control the diameter of the inner and outer droplets, the shell thickness, and the inter-droplet distances. Furthermore, we demonstrate the capability of this hybrid device to form triple emulsions with different sizes, using all-aqueous solutions which have ultralow interfacial tension. Finally, we conduct a proof-of-concept demonstration of "on the fly" shrinkage and growth of double emulsions through triggering re-equilibrium processes, by introducing a continuous phase which is out-of-equilibrium with the rest of the emulsion system [157].

This platform has advantages of both lithography-based microfluidic devices and glass capillary systems. Using this hybrid device circumvents wettability issues observed in typical microfluidic devices, and allows for complex designs of lab-on-a-chip systems. This technology could be used for a variety of different applications, such as for the generation of high-order emulsions with various combination of incompatible phases, the generation of microbubbles, and making microfibers with multiple layers.

Chapter 5: Conclusions and future work

5.1 Summary of findings

Soft biomaterials play an essential role in biomedicine and biological applications. These materials are used for biomedicine applications to enhance healing of damaged tissues, deliver biomolecules, drugs, and in biological applications for making cell colony-supporting matrices, single-cell isolation for further analysis, and cell culturing. Hydrogels and droplets are subcategories of these materials that have been extensively studied.

Typically, the fabrication of emulsions is facilitated by the use of an organic solvent phase, because of the higher interfacial tension at the phase boundary. Since soft materials are used in biological and biomedical applications, the presence of any organic solvent such as oils could be harmful to the system and compromise cell viability. Conventionally, post-processing organic phase removal requires tedious and labour-consuming washing steps. The work described in this dissertation provides novel oil-free techniques to make non-spherical hydrogels and emulsions using all-aqueous phases as alternatives to organic solvent based techniques, and limit their harmful effects.

Chapter 2 presented a method based on electrohydrodynamic atomization to fabricate non-spherical alginate-calcium hydrogels. Based on the literature review, the morphology of the particles affects the release profile of drug delivery systems. Therefore, the presented technique provides the fabrication of particles with tunable shapes. These particles could be functionalized for more advanced applications, for example, encapsulating magnetic particles inside the hydrogels to make magnetizable hydrogels. To demonstrate cellular encapsulation functionality, we captured breast cancer cells. Using electrohydrodynamic atomization also gives increased throughput, which is of vital importance for scaling up production.

Chapter 3 introduced a microfluidic platform to generate water-in-water droplets with a wide range of diameters and in a high production rate. We use PEG and DEX to form droplets inside a microchannel. Even though both phases are hydrophilic, PEG shows more hydrophobic behaviour compared to DEX, so it has historically been challenging to creat PEG-in-DEX droplets. Using a microneedle to introduce the dispersed phase inside the microchannel facilitates the production of droplets, either PEG or DEX, by isolating the disperse phase from having any interaction with the channel walls, and boosting the throughput of the system. Since we used a microneedle, we were able to show the fabrication of PEG-in-DEX droplets for the first time.

Chapter 4 utilized the technique described in Chapter 3 to fabricate higher order all-aqueous emulsions, like double and triple emulsions. We used conventional flow focusing geometries with two cross junctions to fabricate double emulsions, and then three cross junctions for triple emulsions. This is the first reported platform that generates already phase separated ATPS to form higher order emulsions. Utilizing pressure pumps and applying sinusoidal waveforms for the inlets, we presented a method to control the shell thickness of the double emulsions and inter-droplet distances. Moreover, by introducing an out-of-equilibrium aqueous phase, we triggered a re-equilibrium process inside the microchannel to induce the exchange of water molecules. This exchange causes a double emulsion system to shrink or expand based on the concentration of the out-of-equilibrium phase.

5.2 Contributions

The research presented in this dissertation demonstrates novel oil-free approaches to make hydrogels, droplets, and higher order emulsions by utilizing microfluidic methods. We used all-aqueous fluid systems to overcome the many shortcomings of organic solvent based systems in biological environments. To accomplish the development of these systems, the following goals were fulfilled:

(i) The electrohydrodynamic atomization based fabrication of non-spherical hydrogels in a high throughput manner. We demonstrated effective parameters to control the morphology of the particles and also functionalized the hydrogels.

(ii) Development of a microfluidic platform to generate a wide diameter range of DEX-in-PEG droplets with a high production rate by isolating the disperse phase from the

microchannel walls. This platform is also capable of producing PEG-in-DEX droplets, for the first time.

(iii) Fabrication of higher order of all-aqueous emulsions using a novel design, and integration of a glass capillary system with the lithography-based microfluidic system. We presented a straightforward technique to generate double and triple emulsions using already phase separated ATPS. The presented platform is capable of controlling the shell thickness and inter-droplet distances of double emulsions by utilizing a sinusoidal wave function applied on the third inlet. We demonstrated the shrinkage and expansion of the fabricated double emulsions by introducing out-of-equilibrium phases, which then trigger a re-equilibrium process and water molecules exchange between the phases.

Finally, this research provides practical steps to replace traditional systems of making hydrogels and emulsions in which organic solvents are used, with oil-free techniques using all-aqueous approaches.

5.3 Future work

All-aqueous fluid systems circumvent the drawbacks of organic solvent based systems. Developing these systems is inevitable due to their beneficial mechanical and biocompatibility properties. In droplet formation, for example, using water-organic solvent two-phase systems relies on the high interfacial tension between the phases to spontaneously make the dispersions. However, the organic solvent phase is not biocompatible and could be harmful to biological environment. The results presented in this dissertation, using the developed platforms and techniques, provide a pathway for using oil-free systems for the fabrication of soft materials. ATPSs, for instance, provide a biocompatible environment that not only helps to maximize the viability of biological samples, but the polymers used as the phases could also have a stabilizing influence on biocatalysts [42].

The technology presented in Chapter 2 could be extended to study the modelling of drug release behaviour for hydrogels with different morphologies. Controlling the porosity of the hydrogels presented in this dissertation could be beneficial for delivery of different sizes of drug molecules or bioactive materials.

The platforms presented in Chapters 3 and 4, can be utilized to further investigation of ATPS in microfluidics. ATPS is conventionally used to partition biomolecules in one phase and increase the concentration of target molecules such as protein for purification and extraction [139], [143]. Since microfluidics offers exclusive advantages in the control and manipulation the small volumes of fluids, from microliter to femtoliter, the presented platforms in Chapters 3 and 4 could be used for cell partitioning purposes in one, two, or more layers of ATPS.

The platform presented in Chapter 4 could be used to generate microfibers. We are able to generate fibres with a solid core, or as core-shell fibres (hollow fibres) for different biomedical applications such as for regenerative medicine and vaccine encapsulation. Moreover, these microfibers could be used in biological applications such as for cryopreservation, the process of freezing cells for long term storage.

Appendix I: Supplementary information for Chapter 2

This section is published as the supplementary information for the following paper:

Jeyhani, M., Mak, S. Y., Sammut, S., Shum, H. C., Hwang, D. K. and Tsai, S., "Controlled electrospray generation of non-spherical alginate microparticles." *ChemPhysChem*. 2018, 1-7. https://doi.org/10.1002/cphc.201701094

Our hypothesis of the formation mechanism of hemispherical particles:

Droplets dispense out of the glass capillary emitter under the effect of the electric field. The electric field generated by the power supply polarizes the liquid. The positively charged droplets are induced to migrate away from the emitter, towards the negatively charged ring electrode, and to the bath. The droplets experience a swift migration from the emitter to the bath that leads to increasing the impacting energy of the droplets to the bath surface (Figure I.1a).

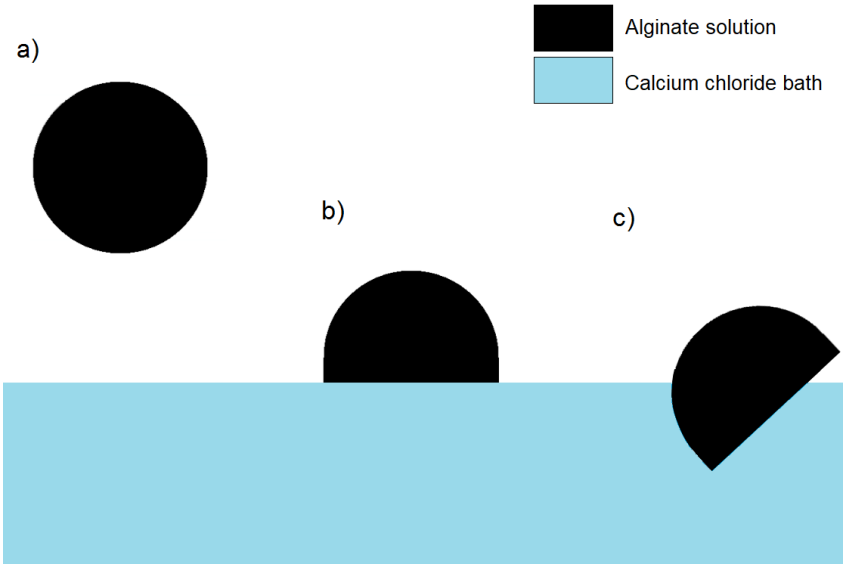

Figure I.1: Formation of hemispherical particles.

The timescale associated with droplet impact is very short, so the bath's free surface remains relatively undeformed. The droplets therefore partially rebound from the free surface, before spreading on the free surface (Figure I.1b). Then, the droplets sediment and immerse in the bath, and solidify, fixing their shape (Figure I.1c).

The calcium chloride concentration C and ring-to-bath distance L_b are important factors in determining the aspect ratio Ω. According to Figure 2.5, particles with lower aspect ratio Ω are formed for higher values of calcium chloride concentration C and/or ring-to-bath distance L_b. Increasing the ring-to-bath distance L_b causes the droplets to impact with more kinetic energy, and leads to more droplet spread, and therefore, lower aspect ratio Ω. Increasing the calcium chloride concentration C increases the polymerization rate, so there is less time for the droplet rebound and cause the droplet to lose its spread shape.

Characteristics of particles:

According to Figure I.2, we define parameters *h*, the height of each particle, *d*, the effective diameter of each particle, and *w*, as the width of tails for cupcake-like and tadpole-like particles. The width, *w*, of the tail is the base length of the tail, measured from the two curvature inflection points that define the base of the tail. The Shape Index and Normalized Tail-Length in Chapter 2 are defined based on the aforementioned variables.

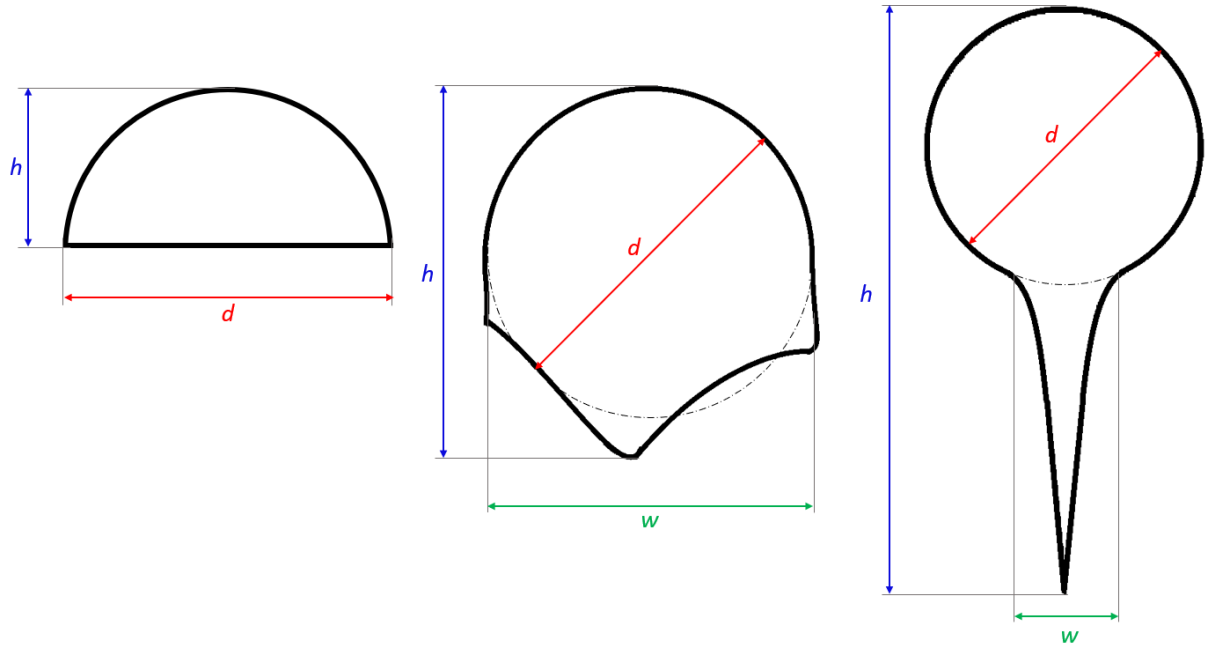

Figure I.2: This figure shows the height h, effective diameter d, and width w of the tail for three types of microparticles.

In order to identify different microparticles, first, we consider the Shape Index $SI = h - d / h + d$. When $SI < 0$, the generated microparticle is of a hemispherical shape. When $SI > 0$, the particle is either cupcake-like or tadpole-like. So, when $SI > 0$, we also consider the Normalized Tail-Length $TL = w/d$. Here, when $TL < 0.5$ we define the particles to be tadpole-like microparticles, and when $TL > 0.5$ we define the particles are cupcake-like.

Physical properties of the solutions:

Table I.1: Physical properties of 2 wt% alginate at room temperature.

Dynamic Viscosity (kg/m.s)	Surface Tension (mN/m)	Density (kg/m^3)
2×10^{-3}	66.5	978.6

Table I.2: Density of the $CaCl_2$ solution at room temperature

Concentration (wt%)	Density (kg/m^3)
1	1,006
2.5	1,018
5	1,042
7.5	1,065
10	1,087

Supplementary Information Video Legend:

Video 1: Video shows the effect of a magnetic field on a magnetized microparticle. The hemispherical magnetic particle rotates as an external permanent magnet is moved around the microparticle. The alginate concentration in this experiment is 2 wt% and calcium chloride concentration C = 5 wt%. The ring-to-bath distance L_b = 20 mm.

See this video at:

https://onlinelibrary.wiley.com/action/downloadSupplement?doi=10.1002%2Fcphc.201701094&file=cphc201701094-sup-0001-Movie_1.avi

Video 2: Here, an external permanent magnet is moved around the magnetic microparticle, causing the microparticle to rotate and reveal its hemispherical shape. The alginate concentration in this experiment is 2 wt% and calcium chloride concentration C = 10 wt%. The ring-to-bath distance L_b = 20 mm.

See this video at:

https://onlinelibrary.wiley.com/action/downloadSupplement?doi=10.1002%2Fcphc.201701094&file=cphc201701094-sup-0001-Movie_2.avi

Appendix II: Supplementary information for Chapter 3

This section is published as the supplementary information for the following paper:

Jeyhani, M., Gnyawali, V., Abbasi, N., Kun Hwang, D. & Tsai, S. S. H. "Microneedle-assisted microfluidic flow focusing for versatile and high throughput water-in-water droplet generation." *J. Colloid Interface Sci.* **553**, 382–389 (2019). https://doi.org/10.1016/j.jcis.2019.05.100

Microdroplet size sensitivity to microneedle position

During the fabrication of our needle-assisted microfluidic devices, we manually fix the position of the needle. Since this is a manual process done under a microscope, it is difficult to ensure that the location of the needle relative to the microfluidic cross junction is always constant. Therefore, we perform experiments where we place the needle at different positions, relative to the microfluidic cross junction, and measure the sensitivity of the resulting droplet sizes to the needle position.

We use our designed geometry as the baseline geometry, to compare with two other geometries that have different microneedle locations, to evaluate the sensitivity of the resulting droplet size to the microneedle location. Figure II.1 represents the position of the microneedle in the original design, where the microneedle tip protrusion, L = 120 µm, measured from the entrance of the cross junction. The other two devices have tip protrusions, L = 60 and 180 µm.

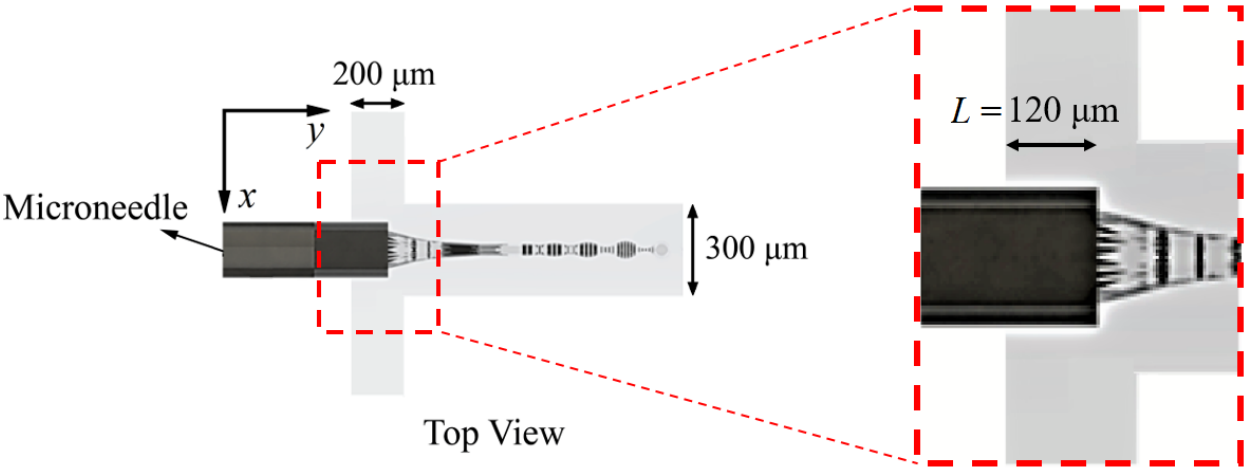

Figure II.1: This figure illustrates the location of the microneedle in the original design, from the top view. In this design, the microneedle tip protrudes, L = 120 µm, out of the microfluidic cross junction. L = 120 µm is the baseline for studying the microdroplets' size sensitivity to the microneedle's location.

We run a set of experiments for each device separately to generate droplets using DEX pressures, P_D = 1.5 - 3.3 kPa and PEG pressure, P_P = 2.0 kPa. We select P_P = 2.0 kPa from the data shown in Figure 3.4 to have a wider range of droplet sizes generated. Figure 7.2 shows the effect of variation of the dispersed DEX phase liquid pressure, P_D, on the resulting droplet diameter for different positions of the microneedle in the microfluidic device. Blue diamonds represent the baseline where L = 120 µm, green diamonds indicate tip protrusion, L = 60 µm, and red diamonds show data from L = 180 µm. The percentage difference is ~100%, between the highest and lowest

values if L. Despite this difference, all of the droplet diameter data lies approximately on the same line. This result suggests that the droplet diameter is relatively insensitive to the microneedle's tip protrusion L, and thus, also insensitive to the precision of the placement of the microneedle relative to the microfluidic cross junction.

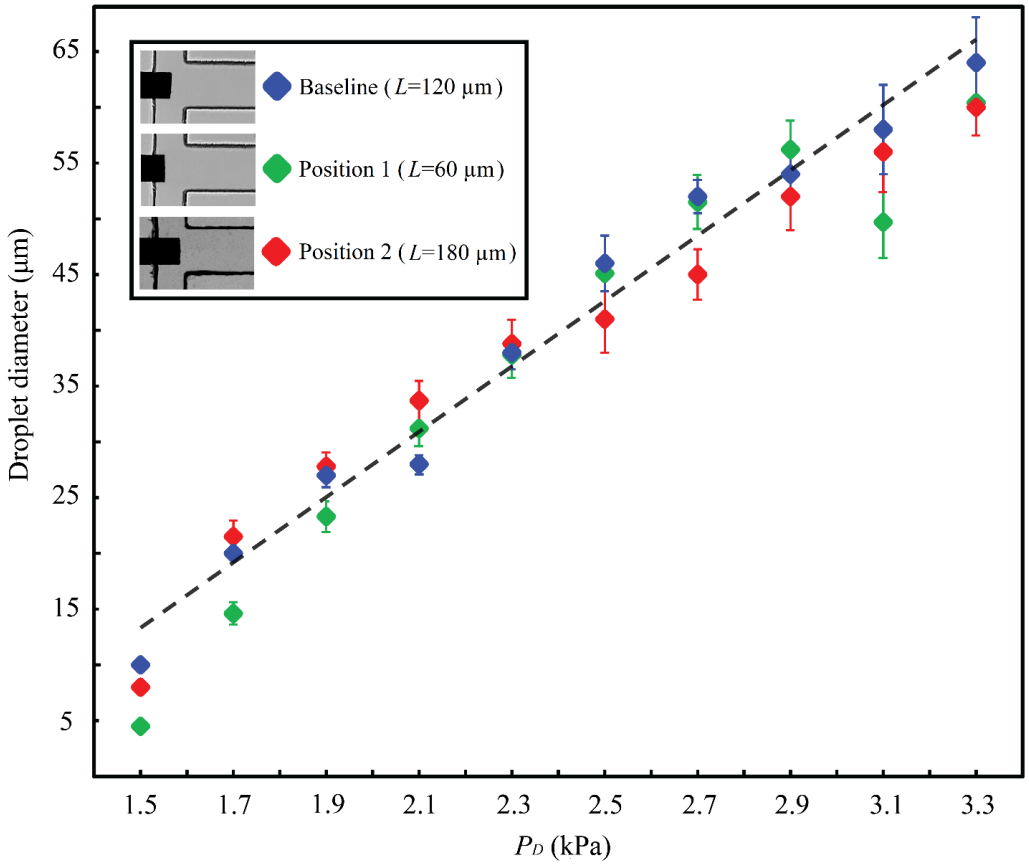

Figure II.2: This figure shows the measured droplet diameter, versus the DEX phase liquid pressure, P_D. Here, the PEG pressure P_P = 2.0 kPa. The data from the baseline microneedle tip protrusion, L = 120 µm, is shown in blue diamonds. Green diamonds show data where L = 60 µm, and red diamonds show data from L = 180 µm.

Device Fabrication

To make the photomask, we design the layout of microchannels using computer-aided-design (CAD) software (AutoCAD 2016, Autodesk, Inc., San Rafael, CA, USA) and print the design on a transparency sheet (25,400 dpi, CAD/Art Services Inc., Bandon, OR, USA). Then, we use a 4-inch diameter silicon wafer (UniversityWafer Inc., Boston, MA, USA) as the substrate for channel feature construction. We spin-coat SU-8 2150 photoresist (MicroChem, Newton, MA, USA) on the wafer and expose the wafer to UV light through the photomask. In the end, we remove the unexposed photoresist by dissolving the wafer in a developer solution (MicroChem, Newton, MA, USA), and only microchannel features remain on the silicon wafer.

To prepare the microfluidic chip, we pour a 10:1 ratio mixture of PDMS resin to curing agent (Sylgard 184, Dow Corning, Midland, MI, USA) onto the silicon master and cured in an oven for 2 hours. Then, we remove the cured PDMS slab from the wafer and use a 1-mm diameter biopsy punch (Integra Miltex, Inc., Rietheim-Weilheim, Germany) to make inlet and outlet holes. After cleaning the PDMS slab and a glass slide, we use oxygen plasma treatment (Harrick Plasma, Ithaca, NY, USA) to bond the PDMS slab and the glass slide irreversibly.

Active Droplet Generation in Microfluidics [211]

Table II.1 shows a list of active microfluidic platforms that mechanically perturb the flow to induce droplet formation. The methods have shown all generate water-in-oil or oil-in-water droplets, as opposed to ATPS droplets, in flow focusing geometries. This table helps to compare existing techniques used to form non-ATPS droplets with our proposed platform.

Table II.1: List of water-in-oil or oil-in-water active droplet microfluidics platforms for droplet generation in a flow focusing geometry.

Method	Mechanism	Diameter range (µm)	Production rate (Hz)	Solutions	
Piezoelectric Control	Mechanical vibration [212]	110 to 150	250-750	D	DI water
				C	mineral Oil M5904, paraffin Oil 76235, mineral Oil 330760
	Surface acoustic waves [213]	88-236	161-171	D	water + bromophenol blue
				C	HFE-7500 fluorocarbon oil + 1.8% DuPont Krytox 157
Pneumatic	Mechanical chopping [214], [215]	6-120	<17	D	DI Water + 0.1% Vitamin C
				C	trioctanoin + polyglyceryl-2 sesquiisostearate + PEG-10 polyglyceryl-2 Laurate
	Periodic mechanical channel compression [216]	31-146	<24	D	olive oil
				C	DI water + 5% Triton X-100
	Periodic mechanical channel compression [217]	5.5-55	<96	D	DI water + 5% Triton X-100
				C	olive oil
Hydraulic	Periodic mechanical channel compression [218]	24-40	<3000	D	water
				C	HFE-7500 fluorocarbon + 5% 1H,1H,2H,2H-perfluoro-1-octanol + 1.8% fluoro-surfactant ammonium carboxylate

C – continuous phase, D – dispersed phase

Appendix III: Supplementary information for Chapter 4

This section is published as the supplementary information for the following paper:

Jeyhani, M., Theyakumaran, R., Abbasi, N., Hwang, D. K. and Tsai, S., "Microfluidic generation of all-aqueous double and triple emulsions." *Small* (2020).

Rheological behaviour of the ATPS solutions

Based on the rheological measurements, the values of elastic modulus *G'*, for all the phase separated DEX and PEG solutions were orders of magnitude lower than the viscous modulus *G"*. Therefore, the solutions did not showcase any elastic behaviour and we only report values of the viscosity. Figure III.1, shows the changes of viscosity η, as a function of shear rate $\dot{\gamma}$, for each phase separated solution.

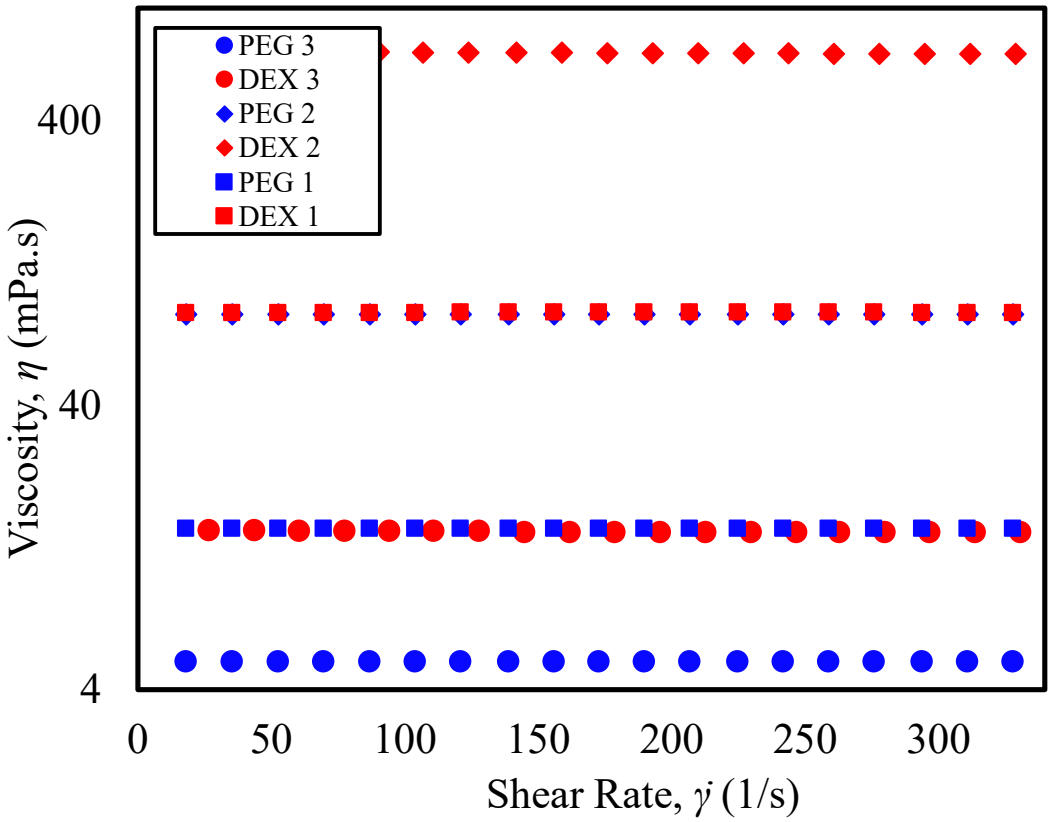

Figure III.1: A plot of viscosity η, versus the shear rate $\dot{\gamma}$. Here, there is no change for the viscosity for the applied shear rates indicating the solutions are Newtonian.

Table III.1: Statistical analysis of data in Figure 4.2h:

$P_{DEX\ Out}$ (mbar)	Droplet Diameter (µm)				Number of samples
	Average D_i	Standard deviation	Average D_o	Standard deviation	
70	110	6	223	10	10
80	108	5	205	4	10
90	100	2	189	5	10
100	93	6	175	9	10
110	88	8	151	11	10
120	78	3	136	8	10
130	63	1	107	5	10
140	61	2	90	2	10
150	51	3	68	5	10

Table III.2: Statistical analysis of data in Figure 4.3b:

$P_{DEX\ In}$ (mbar)	Droplet Diameter (µm)				Number of samples
	Average D_i	Standard deviation	Average D_o	Standard deviation	
15	126	4	245	6	10
20	150	6	247	6	10
25	162	2	250	3	10
30	183	5	260	5	10
35	191	7	262	5	10
40	208	2	270	2	10
45	222	3	278	0	10
50	242	5	295	5	10

Table III.3: Statistical analysis of data in Figure 4.4a:

Period (ms)	Droplet Diameter (µm)				Number of samples
	Average D_i	Standard deviation	Average D_o	Standard deviation	
300	133	3	206	4	10
400	154	3	223	4	10
500	161	3	231	5	10
600	174	5	232	5	10
700	183	5	245	6	10
800	198	6	254	8	10
900	202	5	262	9	10
1000	206	5	265	9	10
1100	220	5	306	17	10
1200	235	10	322	18	10
1300	241	12	337	22	10

Table III.4: Statistical analysis of data in Figure 4.4b:

Period (ms)	Inter-droplet distance (µm)	Standard deviation	Number of samples
300	465	17	10
400	670	17	10
500	896	17	10
600	1153	17	10
700	1395	24	10
800	1604	50	10
900	1871	50	10
1000	2069	40	10
1100	2202	20	10
1200	2380	50	10
1300	2470	30	10

Relationship between pressure and velocity of the liquid inside the microfluidic device.

Considering a steady pressure driven flow (Poiseuille flow), the flow speed could be scaled as:

$$u \sim \frac{a^2}{\mu}\frac{dp}{dz},$$

where a is the height of the channel, μ is the fluid viscosity, and $\frac{dp}{dz}$ is the gradient of pressure in the flow direction, z. A constant flow rate infusion system can also be used for these double and triple emulsions generation experiments.

Different regimes of the phase diagram.

Based on Figure 4.2g, different flow conditions lead to the formation of different emulsion regimes on-chip. Backflow can be observed for the cases that the outer DEX phase pressure is high enough to prevent the dispersed phase flow through the channel after the second cross-junction. Figure III.2a shows collected droplets from the generation regime in which the applied pressure from the outer DEX phase on the intermediate PEG and the inner DEX phase induce a regular breakup and formation of double emulsions. Figure III.2b shows collected droplets that are double emulsions with multiple DEX inner emulsions (Figure III.2b).

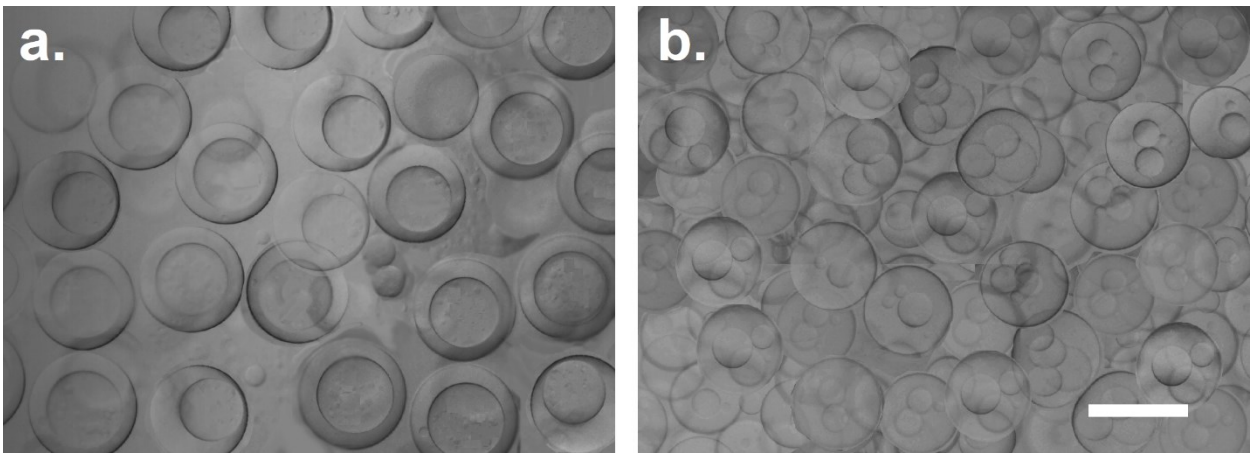

Figure III.2: Different flow conditions results in different types of collected emulsions. a) Collected double emulsions, which are generated using experimental pressures, $P_{DEX\ In}$ = 60 mbar, $P_{PEG\ Mid}$ = 30 mbar, and $P_{DEX\ Out}$ = 400 mbar. b) Collected emulsions that have multiple inner droplets, generated using experimental pressures, $P_{DEX\ In}$ = 80 mbar, $P_{PEG\ Mid}$ = 40 mbar, and $P_{DEX\ Out}$ = 480 mbar. The scale bar represents 150 µm.

Appendix IV: Error analysis

Error analysis [219]

After each experiment, to analyze the results, we measured the size of different particles and droplets at the same experimental data point. Then we reported the arithmetic mean of the measured size to show the central tendancy of our observation. The mean value, $\bar{x}$, is sum of the *i*-th measured values of *x* divided by the number of measurments, *N*.

$$\bar{x} = \frac{1}{N}\left(\sum_{i=1}^{N} x_i\right)$$

And then to show the amount of variation of the mean value we calculated and reported the standard deviation, *S*, using the given formula:

$$S = \sqrt{\frac{1}{N-1}\sum_{i=1}^{N}(x_i - \bar{x})^2}$$

Coefficient of variation (*CV*)

The coefficient of variation (*CV*) is a statistical measurement that shows the dispersion of data around the mean value. The coefficient of variation is the ratio of the standard deviation, *S*, to the mean, $\bar{x}$, and mainly expressed as a percentage.

$$CV = \frac{S}{\bar{x}} \times 100\%$$

Bibliography

[1] Z. Ahmad, E. Stride, and M. Edirisinghe, "Novel preparation of transdermal drug-delivery patches and functional wound healing materials.," *J. Drug Target.*, vol. 17, no. 9, pp. 724–9, 2009.

[2] J. Wu *et al.*, "Fabrication and characterization of monodisperse PLGA-alginate core-shell microspheres with monodisperse size and homogeneous shells for controlled drug release," *Acta Biomater.*, vol. 9, no. 7, pp. 7410–7419, 2013.

[3] S. Köster *et al.*, "Drop-based microfluidic devices for encapsulation of single cells.," *Lab Chip*, vol. 8, no. 7, pp. 1110–1115, 2008.

[4] A. Kang, J. Park, J. Ju, G. S. Jeong, and S. H. Lee, "Cell encapsulation via microtechnologies," *Biomaterials*, vol. 35, no. 9, pp. 2651–2663, 2014.

[5] L. Mazutis, J. Gilbert, W. L. Ung, D. A. Weitz, A. D. Griffiths, and J. A. Heyman, "Single-cell analysis and sorting using droplet-based microfluidics," *Nat. Protoc.*, vol. 8, no. 5, pp. 870–891, 2013.

[6] C. H. Fan, C. Y. Lin, H. L. Liu, and C. K. Yeh, "Ultrasound targeted CNS gene delivery for Parkinson's disease treatment," *J. Control. Release*, vol. 261, no. July, pp. 246–262, 2017.

[7] C. A. García-González, M. Jin, J. Gerth, C. Alvarez-Lorenzo, and I. Smirnova, "Polysaccharide-based aerogel microspheres for oral drug delivery," *Carbohydr. Polym.*, vol. 117, pp. 797–806, 2015.

[8] C. U. Yurteri, R. P. A. Hartman, and J. C. M. Marijnissen, "Producing Pharmaceutical particles via Electrospraying with an emphasis on nano and nano structured particles - A review," *KONA Powder Part. J.*, vol. 28, no. 28, pp. 91–115, 2010.

[9] N. S. Satarkar and J. Z. Hilt, "Magnetic hydrogel nanocomposites for remote controlled pulsatile drug release," *J. Control. Release*, vol. 130, no. 3, pp. 246–251, 2008.

[10] N. S. Satarkar and J. Zach Hilt, "Hydrogel nanocomposites as remote-controlled biomaterials," *Acta Biomater.*, vol. 4, no. 1, pp. 11–16, 2008.

[11] S. Li, L. Xiao, H. Deng, X. Shi, and Q. Cao, "Remote controlled drug release from multi-functional Fe3O4/GO/Chitosan microspheres fabricated by an electrospray method," *Colloids Surfaces B Biointerfaces*, vol. 151, pp. 354–362, 2017.

[12] J. Yu *et al.*, "Multistimuli-regulated photochemothermal cancer therapy remotely controlled via Fe5C2 nanoparticles," *ACS Nano*, vol. 10, no. 1, pp. 159–169, 2016.

[13] M. Lin *et al.*, "Near-infrared light activated delivery platform for cancer therapy," *Adv. Colloid Interface Sci.*, vol. 226, pp. 123–137, 2015.

[14] G. Qin *et al.*, "Partially polymerized liposomes: stable against leakage yet capable of instantaneous release for remote controlled drug delivery," *Nanotechnology*, vol. 22, no. 15, p. 155605, 2011.

[15] Gangaraju Vamsi K. Lin Haifan, "Remote Optical Switch for Localized and Selective Control of Gene Interference," *Nat Rev Mol Cell Biol.*, vol. 10 (2), no. 1, pp. 116–125, 2009.

[16] E. Kasner, C. A. Hunter, D. Ph, K. Kariko, and D. Ph, "NIR-Activated Content Release from Plasmon Resonant Liposomes for Probing Single-Cell Responses," vol. 70, no. 4, pp. 646–656, 2013.

[17] Q. Q. Dou, C. P. Teng, E. Ye, and X. J. Loh, "Effective near-infrared photodynamic therapy assisted by upconversion nanoparticles conjugated with photosensitizers," *Int. J. Nanomedicine*, vol. 10, pp. 419–432, 2015.

[18] R. Huschka, J. Zuloaga, M. W. Knight, L. V. Brown, P. Nordlander, and N. J. Halas, "Light-induced release of DNA from gold nanoparticles: Nanoshells and nanorods," *J. Am. Chem. Soc.*, vol. 133, no. 31, pp. 12247–12255, 2011.

[19] A. Schroeder, J. Kost, and Y. Barenholz, "Ultrasound, liposomes, and drug delivery: principles for using ultrasound to control the release of drugs from liposomes," *Chem. Phys. Lipids*, vol. 162, no. 1–2, pp. 1–16, 2009.

[20] J. A. Champion, Y. K. Katare, and S. Mitragotri, "Particle shape: a new design parameter for micro- and nanoscale drug delivery carriers.," *J. Control. Release*, vol. 121, no. 1–2, pp. 3–9, Aug. 2007.

[21] E. A. Simone, T. D. Dziubla, and V. R. Muzykantov, "Polymeric carriers: role of geometry in drug delivery.," *Expert Opin. Drug Deliv.*, vol. 5, no. 12, pp. 1283–1300, 2008.

[22] Y. Geng *et al.*, "Shape effects of filaments versus spherical particles in flow and drug delivery," *Nat Nano*, vol. 2, no. 4, pp. 249–255, Apr. 2007.

[23] E. A. Simone, T. D. Dziubla, D. E. Discher, and V. R. Muzykantov, "Filamentous polymer nanocarriers of tunable stiffness that encapsulate the therapeutic enzyme catalase," *Biomacromolecules*, vol. 10, no. 6, pp. 1324–1330, 2009.

[24] D. S. T. Hsieh, W. D. Rhine, and R. Langer, "Zero-Order Controlled-Release Polymer Matrices for Micro- and Macromolecules," *J. Pharm. Sci.*, vol. 72, no. 1, pp. 17–22, Feb. 1983.

[25] C. Zhou, P. Zhu, Y. Tian, X. Tang, R. Shi, and L. Wang, "Microfluidic generation of aqueous two-phase-system (ATPS) droplets by oil-droplet choppers," *Lab Chip*, vol. 17, no. 19, pp. 3310–3317, 2017.

[26] L. Zhang *et al.*, "Microfluidic Templated Multicompartment Microgels for 3D Encapsulation and Pairing of Single Cells," *Small*, vol. 14, no. 9, pp. 1–8, 2018.

[27] R. Xie *et al.*, "Necklace-Like Microfibers with Variable Knots and Perfusable Channels Fabricated by an Oil-Free Microfluidic Spinning Process," *Adv. Mater.*, vol. 30, no. 14, pp. 1–6, 2018.

[28] L. Shui, J. C. T. Eijkel, and A. van den Berg, “Multiphase flow in microfluidic systems - Control and applications of droplets and interfaces,” *Adv. Colloid Interface Sci.*, vol. 133, no. 1, pp. 35–49, 2007.

[29] S. L. Anna, N. Bontoux, and H. a. Stone, “Formation of dispersions using ‘flow focusing’ in microchannels,” *Appl. Phys. Lett.*, vol. 82, no. 3, pp. 364–366, 2003.

[30] S. J. Shin, J. S. Hong, K. H. Lee, and S. H. Lee, “Oil-free generation of small polymeric particles using a coaxial microfluidic channel,” *Langmuir*, vol. 25, no. 20, pp. 12361–12366, 2009.

[31] A. L. Grilo, M. R. Aires-barros, and A. M. Azevedo, “Partitioning in Aqueous Two-Phase Systems : Fundamentals , Applications and Trends,” *Sep. Purif. Rev.*, vol. 45, no. 1, pp. 68–80, 2016.

[32] P. Å. Albertsson, *Partition of Cell Particles and Macromolecules*, 3rd ed. New York: Wiley, 1986.

[33] P. a Albertsson, “Partition of cell particles and macromolecules in polymer two-phase systems,” *Adv. Protein Chem.*, vol. 24, no. 43, pp. 309–341, 1970.

[34] M. Jeyhani, V. Gnyawali, N. Abbasi, D. Kun Hwang, and S. S. H. Tsai, “Microneedle-assisted microfluidic flow focusing for versatile and high throughput water-in-water droplet generation,” *J. Colloid Interface Sci.*, pp. 382–389, May 2019.

[35] D. F. C. Silva, A. M. Azevedo, P. Fernandes, V. Chu, J. P. Conde, and M. R. Aires-Barros, “Determination of aqueous two phase system binodal curves using a microfluidic device,” *J. Chromatogr. A*, vol. 1370, pp. 115–120, 2014.

[36] R. D. Rogers and M. A. Eiteman, *Aqueous Biphasic Separations*. Boston, MA: Springer US, 1995.

[37] H. Walter, D. E. Brooks, and D. Fisher, *Partitioning in aqueous two-phase system: theory, methods, uses, and applications to biotechnology*. Academic Press Orlando, 1985.

[38] E. Atefi, J. A. Mann, and H. Tavana, “Ultralow Interfacial Tensions of Aqueous Two-Phase Systems Measured Using Drop Shape.,” *Langmuir*, 2014.

[39] M. H. Salamanca, J. C. Merchuk, B. A. Andrews, and J. A. Asenjo, “On the kinetics of phase separation in aqueous two-phase systems,” *J. Chromatogr. B Biomed. Appl.*, vol. 711, no. 1–2, pp. 319–329, 1998.

[40] J. A. Asenjo and B. A. Andrews, “Aqueous two-phase systems for protein separation: A perspective,” *J. Chromatogr. A*, vol. 1218, no. 49, pp. 8826–8835, 2011.

[41] P. Å. Albertsson, A. Cajarville, D. E. Brooks, and F. Tjerneld, “Partition of proteins in aqueous polymer two-phase systems and the effect of molecular weight of the polymer,” *BBA - Gen. Subj.*, vol. 926, no. 1, pp. 87–93, 1987.

[42] R. Hatti-Kaul, *Aqueous two-phase systems*, vol. 19. 2000.

[43] H. Shin *et al.*, “High-yield isolation of extracellular vesicles using aqueous two-phase system,” *Sci. Rep.*, vol. 5, pp. 1–11, 2015.

[44] J. Herbst and R. W. M. Pott, “The Effect of Temperature on Different Aqueous Two-Phase Diagrams of Polyethylene Glycol (PEG 6000, PEG 8000, and PEG 10000) + Potassium Sodium Tartrate + Water,” *J. Chem. Eng. Data*, vol. 64, no. 7, pp. 3036–3043, 2019.

[45] F. H. B. Sosa, D. de Araujo Sampaio, F. O. Farias, A. B. G. Bonassoli, L. Igarashi-Mafra, and M. R. Mafra, “Measurement and correlation of phase equilibria in aqueous two-phase systems containing polyethyleneglycol (2 000, 4 000, and 6 000) and sulfate salts (manganese sulfate and copper sulfate) at different temperatures (298.15, 318.15, and 338.15 K),” *Fluid Phase Equilib.*, vol. 449, pp. 68–75, 2017.

[46] G. F. Murari *et al.*, “Phase diagrams of aqueous two-phase systems formed by polyethylene glycol+ammonium sulfate+water: Equilibrium data and thermodynamic modeling,” *Fluid Phase Equilib.*, vol. 406, pp. 61–69, 2015.

[47] H. Hartounian, E. Floeter, E. W. Kaler, and S. I. Sandler, “Effect of temperature on the phase equilibrium of aqueous two-phase polymer systems,” *AIChE J.*, vol. 39, no. 12, pp. 1976–1984, 1993.

[48] G. Walter, H. and Johansson, *Aqueous Two-Phase Systems*. Berlin: Elsevier, 1994.

[49] M. Iqbal *et al.*, “Aqueous two-phase system (ATPS): an overview and advances in its applications,” *Biol. Proced. Online*, vol. 18, no. 1, pp. 1–18, 2016.

[50] F. E. Bailey and R. W. Callard, “Some properties of poly(ethylene oxide) in aqueous solution,” *J. Appl. Polym. Sci.*, vol. 1, no. 1, pp. 56–62, 1959.

[51] G. Karlström, “A new model for upper and lower critical solution temperatures in poly(ethylene oxide) solutions,” *J. Phys. Chem.*, vol. 89, no. 23, pp. 4962–4964, 1985.

[52] R. Danielsson and P. Å. Albertsson, “Aqueous polymer two-phase systems and their use in fragmentation and separation of biological membranes for the purpose of mapping the membrane structure,” *Prep. Biochem. Biotechnol.*, vol. 43, no. 5, pp. 512–525, 2013.

[53] K. Nam, W. Chang, and H. Hong, “Continuous-Flow Fractionation of Animal Cells in Microfluidic Device Using Aqueous Two-Phase Extraction,” pp. 189–195, 2005.

[54] M. J. Boland, “Extraction of proteins from animal tissue using multiphase aqueous systems,” *Bioseparation*, vol. 1, no. 3–4, pp. 293–304, 1989.

[55] H. Tavana *et al.*, “Nanolitre liquid patterning in aqueous environments for spatially defined reagent delivery to mammalian cells.,” *Nat. Mater.*, vol. 8, no. 9, pp. 736–41, 2009.

[56] Y. Liu, R. Lipowsky, and R. Dimova, “Concentration dependence of the interfacial tension for aqueous two-phase polymer solutions of dextran and polyethylene glycol,” *Langmuir*, vol. 28, no. 8, pp. 3831–3839, 2012.

[57] C. D. Hendricks and S. Babil, “Generation of uniform, 0.5-10μm, solid particles,” *J. Phys. E.*, vol. 5, no. 9, pp. 905–910, 1972.

[58] P. Kebarle and L. Tang, “From Ions in Solution to Ions in the Gas Phase: The Mechanism of Electrospray Mass Spectrometry,” *Anal. Chem.*, vol. 65, no. 22, 1993.

[59] A. Dahlin, “Common Ionization.” [Online]. Available:

http://www.waters.com/waters/en_CA/Common-Ionization/nav.htm?cid=10073251&locale=en_CA.

[60] K. Hiraoka, *Fundamentals of Mass Spectrometry -Fundamentals of Electrospray-*, vol. 58, no. 4. 2010.

[61] G. I. Taylor, "The Formation of Emulsions in Definable Fields of Flow," *Proc. R. Soc. A Math. Phys. Eng. Sci.*, vol. 146, no. 858, pp. 501–523, 1934.

[62] M. S. Wilm and M. Mann, "Electrospray and Taylor-Cone theory, Dole's beam of macromolecules at last?," *Int. J. Mass Spectrom. Ion Process.*, vol. 136, no. 2–3, pp. 167–180, 1994.

[63] S. Labbaf, H. Ghanbar, E. Stride, and M. Edirisinghe, "Preparation of multilayered polymeric structures using a novel four-needle coaxial electrohydrodynamic device," *Macromol. Rapid Commun.*, vol. 35, no. 6, pp. 618–623, 2014.

[64] M. Nyström, M. Murtomaa, J. Roine, N. Sandler, and J. Salonen, "Processing of pharmaceutical materials by electrospraying under reduced pressure.," *Drug Dev. Ind. Pharm.*, vol. 41, no. 1, pp. 116–23, 2015.

[65] P. Davoodi *et al.*, "Coaxial electrohydrodynamic atomization: Microparticles for drug delivery applications," *J. Control. Release*, vol. 205, pp. 70–82, 2015.

[66] M. Parhizkar *et al.*, "Electrohydrodynamic encapsulation of cisplatin in poly (lactic-co-glycolic acid) nanoparticles for controlled drug delivery," *Nanomedicine Nanotechnology, Biol. Med.*, vol. 12, no. 7, pp. 1919–1929, 2016.

[67] M. Eltayeb, E. Stride, M. Edirisinghe, and A. Harker, "Electrosprayed nanoparticle delivery system for controlled release," *Mater. Sci. Eng. C*, vol. 66, pp. 138–146, 2016.

[68] U. Farook, H. B. Zhang, M. J. Edirisinghe, E. Stride, and N. Saffari, "Preparation of microbubble suspensions by co-axial electrohydrodynamic atomization," *Med. Eng. Phys.*, vol. 29, no. 7, pp. 749–754, 2007.

[69] W. C. Yan, Q. W. Chua, X. J. Ong, V. K. Sharma, Y. W. Tong, and C. H. Wang, "Fabrication of ultrasound-responsive microbubbles via coaxial electrohydrodynamic atomization for triggered release of tPA," *J. Colloid Interface Sci.*, vol. 501, pp. 282–293, 2017.

[70] M. Parhizkar, E. Stride, and M. Edirisinghe, "Preparation of monodisperse microbubbles using an integrated embedded capillary T-junction with electrohydrodynamic focusing," *Lab Chip*, vol. 14, no. 14, pp. 2437–2446, 2014.

[71] J. Anu Bhushani and C. Anandharamakrishnan, "Electrospinning and electrospraying techniques: Potential food based applications," *Trends Food Sci. Technol.*, vol. 38, no. 1, pp. 21–33, 2014.

[72] B. E. Rapp and B. E. Rapp, "Introduction," *Microfluid. Model. Mech. Math.*, pp. 3–7, Jan. 2017.

[73] S.-Y. Teh, R. Lin, L.-H. Hung, and A. P. Lee, "Droplet microfluidics.," *Lab Chip*, vol. 8,

no. 2, pp. 198–220, 2008.

[74] P. Garstecki, M. J. Fuerstman, H. a Stone, and G. M. Whitesides, "Formation of droplets and bubbles in a microfluidic T-junction-scaling and mechanism of break-up.," *Lab Chip*, vol. 6, no. 3, pp. 437–446, 2006.

[75] J. K. Nunes, S. S. H. Tsai, J. Wan, and H. A. Stone, "Dripping and jetting in microfluidic multiphase flows applied to particle and fibre synthesis," *J. Phys. D. Appl. Phys.*, vol. 46, no. 11, 2013.

[76] Y. Chao, S. Y. Mak, S. Rahman, S. Zhu, and H. C. Shum, "Generation of High-Order All-Aqueous Emulsion Drops by Osmosis-Driven Phase Separation," vol. 1802107, pp. 1–7, 2018.

[77] M. Das, H. Zhang, and E. Kumacheva, "Microgels: Old Materials with New Applications," *Annu. Rev. Mater. Res.*, vol. 36, no. 1, pp. 117–142, 2006.

[78] P. Panda *et al.*, "Stop-flow lithography to generate cell-laden microgel particles," *Lab Chip*, vol. 8, no. 7, p. 1056, 2008.

[79] L. K. Fiddes, E. W. K. Young, E. Kumacheva, and A. R. Wheeler, "Flow of microgel capsules through topographically patterned microchannels.," *Lab Chip*, vol. 7, no. 7, pp. 863–7, 2007.

[80] H. Zhang, E. Tumarkin, R. M. A. Sullan, G. C. Walker, and E. Kumacheva, "Exploring microfluidic routes to microgels of biological polymers," *Macromol. Rapid Commun.*, vol. 28, no. 5, pp. 527–538, 2007.

[81] J. A. Champion, Y. K. Katare, and S. Mitragotri, "Particle shape: A new design parameter for micro- and nanoscale drug delivery carriers," *J. Control. Release*, vol. 121, no. 1–2, pp. 3–9, 2007.

[82] O. Pillai and R. Panchagnula, "Polymers in Drug Delivery Omathanu Pillai and Ramesh Panchagnula," *Curr. Opin. Chem. Biol.*, vol. 5, pp. 447–451, 2001.

[83] S. Martins, B. Sarmento, E. B. Souto, and D. C. Ferreira, "Insulin-loaded alginate microspheres for oral delivery - Effect of polysaccharide reinforcement on physicochemical properties and release profile," *Carbohydr. Polym.*, vol. 69, no. 4, pp. 725–731, 2007.

[84] J. Panyam *et al.*, "Polymer degradation and in vitro release of a model protein from poly(D,L-lactide-co-glycolide) nano- and microparticles," *J. Control. Release*, vol. 92, no. 1–2, pp. 173–187, 2003.

[85] J. Sun and H. Tan, "Alginate-based biomaterials for regenerative medicine applications," *Materials (Basel).*, vol. 6, no. 4, pp. 1285–1309, 2013.

[86] S. Utech, R. Prodanovic, A. S. Mao, R. Ostafe, D. J. Mooney, and D. a. Weitz, "Microfluidic Generation of Monodisperse, Structurally Homogeneous Alginate Microgels for Cell Encapsulation and 3D Cell Culture," *Adv. Healthc. Mater.*, vol. 4, pp. 1628–1633, 2015.

[87] A. G. Håti, D. C. Bassett, J. M. Ribe, P. Sikorski, D. A. Weitz, and B. T. Stokke, "Versatile, cell and chip friendly method to gel alginate in microfluidic devices.," *Lab Chip*, vol. 16,

no. 19, pp. 3718–3727, 2016.

[88] W. H. Tan and S. Takeuchi, "Monodisperse alginate hydrogel microbeads for cell encapsulation," *Adv. Mater.*, vol. 19, no. 18, pp. 2696–2701, 2007.

[89] S. Hua, H. Yang, Q. Li, J. Zhang, and A. Wang, "pH-sensitive sodium alginate/calcined hydrotalcite hybrid beads for controlled release of diclofenac sodium.," *Drug Dev. Ind. Pharm.*, vol. 38, no. 6, pp. 728–34, 2012.

[90] T. Andersen, B. L. Strand, K. Formo, E. Alsberg, and B. E. Christensen, "Alginates as biomaterials in tissue engineering," *Carbohydr. Chem. Chem. Biol. Approaches, Vol. 37*, pp. 227–258, 2012.

[91] Y. Tabata, S. Gutta, and R. Langer, "Controlled Delivery Systems for Proteins Using Polyanhydride Microspheres," *Pharmaceutical Research: An Official Journal of the American Association of Pharmaceutical Scientists*, vol. 10, no. 4. pp. 487–496, 1993.

[92] M. Dunne, O. I. Corrigan, and Z. Ramtoola, "Influence of particle size and dissolution conditions on the degradation properties of polylactide-co-glycolide particles," *Biomaterials*, vol. 21, no. 16, pp. 1659–1668, 2000.

[93] C. Berkland, K. Kim, and D. W. Pack, "Fabrication of PLG microspheres with precisely controlled and monodisperse size distributions," *J. Control. Release*, vol. 73, no. 1, pp. 59–74, 2001.

[94] S. Xu *et al.*, "Generation of monodisperse particles by using microfluidics: Control over size, shape, and composition," *Angew. Chemie - Int. Ed.*, vol. 44, no. 5, pp. 724–728, 2005.

[95] D. Dendukuri, K. Tsoi, T. A. Hatton, and P. S. Doyle, "Controlled synthesis of nonspherical microparticles using microfluidics," *Langmuir*, vol. 21, no. 6, pp. 2113–2116, 2005.

[96] D. Dendukuri, D. C. Pregibon, J. Collins, T. A. Hatton, and P. S. Doyle, "Continuous-flow lithography for high-throughput microparticle synthesis.," *Nat. Mater.*, vol. 5, no. 5, pp. 365–369, 2006.

[97] J. P. Rolland, B. W. Maynor, L. E. Euliss, A. E. Exner, G. M. Denison, and J. M. DeSimone, "Direct fabrication and harvesting of monodisperse, shape-specific nanobiomaterials," *J. Am. Chem. Soc.*, vol. 127, no. 28, pp. 10096–10100, 2005.

[98] T. S. Shim, S.-M. Yang, and S.-H. Kim, "Dynamic designing of microstructures by chemical gradient-mediated growth," *Nat. Commun.*, vol. 6, p. 6584, 2015.

[99] D. K. Hwang *et al.*, "Stop-Flow lithography for the production of shape-evolving degradable microgel particles," *J. Am. Chem. Soc.*, vol. 131, no. 12, pp. 4499–4504, 2009.

[100] D. K. Hwang, D. Dendukuri, and P. S. Doyle, "Microfluidic-based synthesis of non-spherical magnetic hydrogel microparticles.," *Lab Chip*, vol. 8, no. 10, pp. 1640–1647, 2008.

[101] O. Jeon, K. H. Bouhadir, J. M. Mansour, and E. Alsberg, "Photocrosslinked alginate hydrogels with tunable biodegradation rates and mechanical properties," *Biomaterials*, vol. 30, no. 14, pp. 2724–2734, 2009.

[102] E. S. Chan, B. B. Lee, P. Ravindra, and D. Poncelet, "Prediction models for shape and size of ca-alginate macrobeads produced through extrusion-dripping method," *J. Colloid Interface Sci.*, vol. 338, no. 1, pp. 63–72, 2009.

[103] F. Davarci, D. Turan, B. Ozcelik, and D. Poncelet, "The influence of solution viscosities and surface tension on calcium-alginate microbead formation using dripping technique," *Food Hydrocoll.*, vol. 62, pp. 119–127, 2017.

[104] D. An *et al.*, "Mass production of shaped particles through vortex ring freezing," *Nat. Commun.*, vol. 7, p. 12401, 2016.

[105] Q. Gao, Y. He, J. zhong Fu, J. jiang Qiu, and Y. an Jin, "Fabrication of shape controllable alginate microparticles based on drop-on-demand jetting," *J. Sol-Gel Sci. Technol.*, vol. 77, no. 3, pp. 610–619, 2016.

[106] Y. Hu, Q. Wang, J. Wang, J. Zhu, H. Wang, and Y. Yang, "Shape controllable microgel particles prepared by microfluidic combining external ionic crosslinking," *Biomicrofluidics*, vol. 6, no. 2, pp. 1–9, 2012.

[107] R. Zhou, F. Bai, and C. Wang, "Magnetic separation of microparticles by shape," *Lab Chip*, vol. 17, no. November 2016, pp. 401–406, 2017.

[108] G. Orive *et al.*, "History, challenges and perspectives of cell microencapsulation," *Trends Biotechnol.*, vol. 22, no. 2, pp. 87–92, 2004.

[109] R. H. Li, "Materials for immunoisolated cell transplantation," *Adv. Drug Deliv. Rev.*, vol. 33, no. 1–2, pp. 87–109, 1998.

[110] L. M. Weber, J. He, B. Bradley, K. Haskins, and K. S. Anseth, "PEG-based hydrogels as an in vitro encapsulation platform for testing controlled β-cell microenvironments," *Acta Biomater.*, vol. 2, no. 1, pp. 1–8, 2006.

[111] S. M. Naqvi, S. Vedicherla, J. Gansau, T. McIntyre, M. Doherty, and C. T. Buckley, "Living Cell Factories - Electrosprayed Microcapsules and Microcarriers for Minimally Invasive Delivery," *Adv. Mater.*, pp. 5662–5671, 2016.

[112] Y. Zhao *et al.*, "Lab-on-a-chip technologies for single-molecule studies," *Lab Chip*, vol. 13, no. 12, pp. 2183–2198, 2013.

[113] C. H. Yang *et al.*, "Microfluidic assisted synthesis of multi-functional polycaprolactone microcapsules: Incorporation of CdTe quantum dots, Fe3O4superparamagnetic nanoparticles and tamoxifen anticancer drugs," *Lab Chip*, vol. 9, no. 7, pp. 961–965, 2009.

[114] Y. Zhan, J. Wang, N. Bao, and C. Lu, "Electroporation of cells in microfluidic droplets," *Anal. Chem.*, vol. 81, no. 5, pp. 2027–2031, 2009.

[115] Q. Wang, D. Zhang, X. Yang, H. Xu, A. Q. Shen, and Y. Yang, "Atom-economical in situ synthesis of BaSO4 as imaging contrast agents within poly(N-isopropylacrylamide) microgels using one-step droplet microfluidics," *Green Chem.*, vol. 15, no. 8, pp. 2222–2229, 2013.

[116] A. Golberg *et al.*, "Cloud-enabled microscopy and droplet microfluidic platform for specific

detection of Escherichia coli in water," *PLoS One*, vol. 9, no. 1, pp. 4–12, 2014.

[117] V. Srinivasan, V. K. Pamula, and R. B. Fair, "An integrated digital microfluidic lab-on-a-chip for clinical diagnostics on human physiological fluids," *Lab Chip*, vol. 4, no. 4, pp. 310–315, 2004.

[118] L. Mazutis, J. Gilbert, W. L. Ung, D. A. Weitz, A. D. Griffiths, and J. A. Heyman, "Single-cell analysis and sorting using droplet-based microfluidics," *Nat. Protoc.*, vol. 8, no. 5, pp. 870–891, 2013.

[119] B. T. Kelly, J.-C. Baret, V. Taly, and A. D. Griffiths, "Miniaturizing chemistry and biology in microdroplets," *Chem. Commun.*, no. 18, pp. 1773–1788, 2007.

[120] E. Brouzes *et al.*, "Droplet microfluidic technology for single-cell high-throughput screening.," *Proc. Natl. Acad. Sci. U. S. A.*, vol. 106, no. 34, pp. 14195–200, 2009.

[121] H. N. Joensson and H. Andersson Svahn, "Droplet microfluidics-A tool for single-cell analysis," *Angew. Chemie - Int. Ed.*, vol. 51, no. 49, pp. 12176–12192, 2012.

[122] M. Fischlechner, Y. Schaerli, M. F. Mohamed, S. Patil, C. Abell, and F. Hollfelder, "Evolution of enzyme catalysts caged in biomimetic gel-shell beads," *Nat. Chem.*, vol. 6, no. 9, pp. 791–796, 2014.

[123] S. Köster *et al.*, "Drop-based microfluidic devices for encapsulation of single cells," *Lab Chip*, vol. 8, no. 7, pp. 1110–1115, 2008.

[124] B. L. Wang *et al.*, "Microfluidic high-throughput culturing of single cells for selection based on extracellular metabolite production or consumption," *Nat. Biotechnol.*, vol. 32, no. 5, pp. 473–478, 2014.

[125] I. Barbulovic-Nad, S. H. Au, and A. R. Wheeler, "A microfluidic platform for complete mammalian cell culture," *Lab Chip*, vol. 10, no. 12, pp. 1536–1542, 2010.

[126] J. Clausell-Tormos *et al.*, "Droplet-Based Microfluidic Platforms for the Encapsulation and Screening of Mammalian Cells and Multicellular Organisms," *Chem. Biol.*, vol. 15, no. 5, pp. 427–437, 2008.

[127] J. Schemberg, A. Grodrian, R. Römer, B. P. Cahill, G. Gastrock, and K. Lemke, "Application of segmented flow for quality control of food using microfluidic tools," *Phys. Status Solidi Appl. Mater. Sci.*, vol. 207, no. 4, pp. 904–912, 2010.

[128] B.-U. Moon, S. G. Jones, D. K. Hwang, and S. S. H. Tsai, "Microfluidic generation of aqueous two-phase system (ATPS) droplets by controlled pulsating inlet pressures," *Lab Chip*, vol. 15, no. 11, pp. 2437–2444, 2015.

[129] B.-U. Moon, N. Abbasi, S. G. Jones, D. K. Hwang, and S. S. H. Tsai, "Water-in-water droplets by passive microfluidic flow focusing," *Anal. Chem.*, vol. 88, no. 7, pp. 3982–3989, 2016.

[130] R. Hatti-kaul, "Aqueous Two-Phase Systems," *Mol. Biotechnol.*, vol. 19, no. 3, pp. 697–713, 2001.

[131] H. Walter, G. Johansson, and D. E. Brooks, "Partitioning in aqueous two-phase systems:

recent results.," *Anal. Biochem.*, vol. 197, no. 1, pp. 1–18, 1991.

[132] G. Walter, H. and Johansson, *Methods in Enzymology: Aqueous Two- Phase Systems*. San Diego, CA: Academic Press, 1994.

[133] H. Walter, E. J. Krob, and D. E. Brooks, "Membrane surface properties other than charge involved in cell separation by partition in polymer, aqueous two-phase systems," *Biochemistry*, vol. 15, no. 14, pp. 2959–2964, 1975.

[134] H. Walter, C. H. Tamblyn, E. M. Levy, D. E. Brooks, and G. V. F. Seaman, "Electrophoretic mobilities of human peripheral blood lymphocytes subfractionated by partitioning in two-polymer aqueous phase system," *Biochim. Biophys. Acta*, vol. 598, pp. 193–199, 1980.

[135] H. Michalski, J. P., Zanki, S., Anderson, J. L., & Walter, "Subfractionation of human peripheral blood lymphocytes by partitioning in two-polymer aqueous phase systems. Characteristics of a small subpopulation of cells with high partition coefficient.," *J. Clin. Lab. Immunol.*, vol. 21(1), pp. 43–48, 1986.

[136] K. Nam, W. Chang, and H. Hong, "Continuous-Flow Fractionation of Animal Cells in Microfluidic Device Using Aqueous Two-Phase Extraction," *Biomed. Microdevices*, vol. 7, no. 3, pp. 189–195, 2005.

[137] J. R. SooHoo and G. M. Walker, "Microfluidic aqueous two phase system for leukocyte concentration from whole blood," *Biomed. Microdevices*, vol. 11, pp. 323–329, 2009.

[138] M. Yamada, V. Kasim, M. Nakashima, J. Edahiro, and M. Seki, "Continuous cell partitioning using an aqueous two-phase flow system in microfluidic devices," *Biotechnol. Bioeng.*, vol. 88, no. 4, pp. 489–494, 2004.

[139] M. Pinilla, J. De Fuente, A. I. Garcia-perez, P. Sancho, J. Luque, and P. Jimeno, "Biochemical characterization of human erythrocytes fractionated by counter-current distribution in aqueous polymer two-phase systems," *J. Chromatogr. A*, vol. 668, pp. 165–171, 1994.

[140] D. Johansson, G., Walter, H., Brooks, D. E., & Fisher, *Partitioning in Aqueous Two Phase Systems. Theory, Methods, Uses, and Applications to Biotechnology*. Orlando, FL: Academic Press Orlando, 1985.

[141] K. D. Cole, "Preparation of plasmid and high molecular weight DNA by the use of salt-polymer two-phase extraction," *Biotechniques*, vol. 11, pp. 18–24, 1991.

[142] B. H. Tavana, B. Mosadegh, and S. Takayama, "Polymeric Aqueous Biphasic Systems for Non-Contact Cell Printing on Cells : Engineering Heterocellular Embryonic Stem Cell Niches," *Adv. Mater.*, vol. 22, pp. 2628–2631, 2010.

[143] P. Jordan and H. Vilter, "Extraction of proteins from material rich in anionic mucilages : Partition and fractionation of vanadate-dependent bromoperoxidases from the brown algae Laminaria digitata and L. saccharina in aqueous polymer two-phase systems," *Biochem. Biophys.*, vol. 1073, pp. 98–106, 1991.

[144] R. February, "A Polymer Two Phase System Adapted to Virus Detection," *Arch. Gesamte. Virusforsch*, vol. 372, pp. 365–372, 1970.

[145] P. Mathiazakan *et al.*, "Pilot Scale Aqueous Two-Phase Floatation for Direct Recovery of Lipase Derived from Burkholderia cepacia strain ST8," *Sep. Purif. Technol.*, vol. 171, pp. 206–213, 2016.

[146] H. Sikdar, S. K., Cole, K. D., Stewart, R. M., Szlag, D. C., Todd, P., and Cabezas and Jr., "Aqueous two-phase extractions in bioseparations: an assessment," *Bio/Technology*, vol. 9, pp. 253–256, 1991.

[147] J. K. Nunes, S. S. H. Tsai, J. Wan, and H. A. Stone, "Dripping and jetting in microfluidic multiphase flows applied to particle and fiber synthesis.," *J. Phys. D. Appl. Phys.*, vol. 46, no. 11, p. 114002, 2013.

[148] C. N. Baroud, F. Gallaire, and R. Dangla, "Dynamics of microfluidic droplets," *Lab Chip*, vol. 10, no. 16, pp. 2032–2045, 2010.

[149] H. Gu, M. H. G. Duits, and F. Mugele, "Droplets formation and merging in two-phase flow microfluidics," *Int. J. Mol. Sci.*, vol. 12, no. 4, pp. 2572–2597, 2011.

[150] S. D. Geschiere, I. Ziemecka, V. Van Steijn, G. J. M. Koper, and J. H. Van Esch, "Slow growth of the Rayleigh-Plateau instability in aqueous two phase systems Slow growth of the Rayleigh-Plateau instability in aqueous two phase systems," vol. 6, no. 2, pp. 220071–2200712, 2012.

[151] I. Ziemecka *et al.*, "Monodisperse hydrogel microspheres by forced droplet formation in aqueous two-phase systems," *Lab Chip*, vol. 11, no. 4, pp. 620–624, 2011.

[152] I. Ziemecka, V. Van Steijn, G. J. M. Koper, M. T. Kreutzer, and J. H. Van Esch, "All-aqueous core-shell droplets produced in a microfluidic device," *Soft Matter*, vol. 7, no. 21, pp. 9878–9880, 2011.

[153] S. Y. Mak, Y. Chao, S. Rahman, and H. C. Shum, "Droplet Formation by Rupture of Vibration-Induced Interfacial Fingers," *Langmuir*, vol. 34, no. 3, pp. 926–932, 2018.

[154] A. Sauret and H. C. Shum, "Forced generation of simple and double emulsions in all-aqueous systems," *Appl. Phys. Lett.*, vol. 100, no. 15, pp. 2–5, 2012.

[155] Y. Song and H. C. Shum, "Monodisperse w/w/w double emulsion induced by phase separation," *Langmuir*, vol. 28, no. 33, pp. 12054–12059, 2012.

[156] N. Abbasi, M. Navi, and S. S. H. Tsai, "Microfluidic Generation of Particle-Stabilized Water-in-Water Emulsions," *Langmuir*, vol. 34, no. 1, pp. 213–218, 2018.

[157] B. U. Moon, D. K. Hwang, and S. S. H. Tsai, "Shrinking, growing, and bursting: Microfluidic equilibrium control of water-in-water droplets," *Lab Chip*, vol. 16, no. 14, pp. 2601–2608, 2016.

[158] H. Cheung Shum, J. Varnell, and D. A. Weitz, "Microfluidic fabrication of water-in-water (w/w) jets and emulsions," *Biomicrofluidics*, vol. 6, pp. 128081–128089, 2012.

[159] J. F. Boyce, B. A. Hovanes, J. M. Harris, J. M. Van Alstine, and D. E. Brooks, "The wetting behavior of aqueous two-phase polymer test systems on dextran coated glass surfaces: Effect of molecular weight," *J. Colloid Interface Sci.*, vol. 149, no. 1, pp. 153–161, 1992.

[160] S. H. Kim, J. W. Kim, D. H. Kim, S. H. Han, and D. A. Weitz, "Enhanced-throughput production of polymersomes using a parallelized capillary microfluidic device," *Microfluid. Nanofluidics*, vol. 14, no. 3–4, pp. 509–514, 2013.

[161] K. Xu, J. H. Xu, Y. C. Lu, and G. S. Luo, "A novel method of fabricating, adjusting, and optimizing polystyrene colloidal crystal nonspherical microparticles from gas-water janus droplets in a double Coaxial Microfluidic Device," *Cryst. Growth Des.*, vol. 14, no. 2, pp. 401–405, 2014.

[162] T. Brugarolas, F. Tu, and D. Lee, "Directed assembly of particles using microfluidic droplets and bubbles," *Soft Matter*, vol. 9, no. 38, pp. 9046–9058, 2013.

[163] L. Yobas, S. Martens, W. L. Ong, and N. Ranganathan, "High-performance flow-focusing geometry for spontaneous generation of monodispersed droplets," *Lab Chip*, vol. 6, no. 8, pp. 1073–1079, 2006.

[164] Y. Xia and G. M. Whitesides, "Soft lithography," *Annu. Rev. Mater. Sci.*, vol. 28, no. 12, pp. 153–184, 1998.

[165] X. Xu *et al.*, "Microfluidic production of nanoscale perfluorocarbon droplets as liquid contrast agents for ultrasound imaging," *Lab Chip*, vol. 17, no. 20, pp. 3504–3513, 2017.

[166] V. Gnyawali, M. Saremi, M. C. Kolios, and S. S. H. Tsai, "Stable microfluidic flow focusing using hydrostatics," *Biomicrofluidics*, vol. 11, no. 3, pp. 1–7, 2017.

[167] T. Ward, M. Faivre, M. Abkarian, and H. A. Stone, "Microfluidic flow focusing: Drop size and scaling in pressure versus flow-rate-driven pumping," *Electrophoresis*, vol. 26, no. 19, pp. 3716–3724, 2005.

[168] J. Li, N. Mittal, S. Y. Mak, Y. Song, and H. C. Shum, "Perturbation-induced droplets for manipulating droplet structure and configuration in microfluidics," *J. Micromechanics Microengineering*, vol. 25, no. 8, pp. 1–12, 2015.

[169] H.-T. Liu, H. Wang, W.-B. Wei, H. Liu, L. Jiang, and J.-H. Qin, "A Microfluidic Strategy for Controllable Generation of Water-in-Water Droplets as Biocompatible Microcarriers," *Small*, vol. 1801095, p. 1801095, 2018.

[170] M. Mastiani, S. Seo, B. Mosavati, and M. Kim, "High-Throughput Aqueous Two-Phase System Droplet Generation by Oil-Free Passive Microfluidics," *ACS Omega*, vol. 3, no. 8, pp. 9296–9302, 2018.

[171] M. González-González and M. Rito-Palomares, "Aqueous two-phase systems strategies to establish novel bioprocesses for stem cells recovery," *Crit. Rev. Biotechnol.*, vol. 34, no. 4, pp. 318–327, 2014.

[172] S. Mytnyk *et al.*, "Microcapsules with a permeable hydrogel shell and an aqueous core continuously produced in a 3D microdevice by all-aqueous microfluidics," *RSC Adv.*, vol. 7, no. 19, pp. 11331–11337, 2017.

[173] W. J. Duncanson, T. Lin, A. R. Abate, S. Seiffert, R. K. Shah, and D. a Weitz, "Microfluidic synthesis of advanced microparticles for encapsulation and controlled release.," *Lab Chip*, vol. 12, no. 12, pp. 2135–45, 2012.

[174] K. P. Yuet, D. K. Hwang, R. Haghgooie, and P. S. Doyle, "Multifunctional superparamagnetic janus particles," *Langmuir*, vol. 26, no. 6, pp. 4281–4287, 2010.

[175] Z. Nie, S. Xu, M. Seo, P. C. Lewis, and E. Kumacheva, "Polymer particles with various shapes and morphologies produced in continuous microfluidic reactors," *J. Am. Chem. Soc.*, vol. 127, no. 22, pp. 8058–8063, 2005.

[176] C. H. Chen, A. R. Abate, D. Lee, E. M. Terentjev, and D. A. Weitz, "Microfluidic assembly of magnetic hydrogel particles with uniformly anisotropic structure," *Adv. Mater.*, vol. 21, no. 31, pp. 3201–3204, 2009.

[177] W. Wang *et al.*, "A novel thermo-induced self-bursting microcapsule with magnetictargeting property," *ChemPhysChem*, vol. 10, no. 14, pp. 2405–2409, 2009.

[178] S. W. Choi, Y. Zhang, and Y. Xia, "Fabrication of microbeads with a controllable hollow interior and porous wall using a capillary fluidic device," *Adv. Funct. Mater.*, vol. 19, no. 18, pp. 2943–2949, 2009.

[179] C. H. Choi *et al.*, "Triple Emulsion Drops with An Ultrathin Water Layer: High Encapsulation Efficiency and Enhanced Cargo Retention in Microcapsules," *Adv. Mater.*, vol. 28, no. 17, pp. 3340–3344, 2016.

[180] Y. Zhu *et al.*, "Stimuli-responsive controlled drug release from a hollow mesoporous silica sphere/polyelectrolyte multilayer core-shell structure," *Angew. Chemie - Int. Ed.*, vol. 44, no. 32, pp. 5083–5087, 2005.

[181] S. H. Im, U. Jeong, and Y. Xia, "Polymer hollow particles with controllable holes in their surfaces," *Nat. Mater.*, vol. 4, no. 9, pp. 671–675, 2005.

[182] E. Amstad, S. H. Kim, and D. A. Weitz, "Photo- and thermoresponsive polymersomes for triggered release," *Angew. Chemie - Int. Ed.*, vol. 51, no. 50, pp. 12499–12503, 2012.

[183] S. Higashi and T. Setoguchi, "Hepatic arterial injection chemotherapy for hepatocellular carcinoma with epirubicin aqueous solution as numerous vesicles in iodinated poppy-seed oil microdroplets: clinical application of water-in-oil-in-water emulsion prepared using a membrane emulsifi," *Adv. Drug Deliv. Rev.*, vol. 45, pp. 57–64, 2000.

[184] T. G. Park, H. Y. Lee, and Y. S. Nam, "A new preparation method for protein loaded poly(D,L-lactic-co-glycolic acid) microspheres and protein release mechanism study," *J. Control. Release*, vol. 55, no. 2–3, pp. 181–191, 1998.

[185] M. H. Lee, S. G. Oh, S. K. Moon, and S. Y. Bae, "Preparation of silica particles encapsulating retinol using o/w/o multiple emulsions," *J. Colloid Interface Sci.*, vol. 240, no. 1, pp. 83–89, 2001.

[186] D. J. McClements and Y. Li, "Structured emulsion-based delivery systems: Controlling the digestion and release of lipophilic food components," *Adv. Colloid Interface Sci.*, vol. 159, no. 2, pp. 213–228, 2010.

[187] R. Wegmüller, M. B. Zimmermann, V. G. Bühr, E. J. Windhab, and R. F. Hurrell, "Development, stability, and sensory testing of microcapsules containing iron, iodine, and vitamin A for use in food fortification," *J. Food Sci.*, vol. 71, no. 2, 2006.

[188] A. Benichou, A. Aserin, and N. Garti, "W/O/W double emulsions stabilized with WPI-polysaccharide complexes," *Colloids Surfaces A Physicochem. Eng. Asp.*, vol. 294, no. 1–3, pp. 20–32, 2007.

[189] S. Van Der Graaf, C. G. P. H. Schroën, and R. M. Boom, "Preparation of double emulsions by membrane emulsification - A review," *J. Memb. Sci.*, vol. 251, no. 1–2, pp. 7–15, 2005.

[190] J. Lu, J. D. Litster, and Z. K. Nagy, "Nucleation Studies of Active Pharmaceutical Ingredients in an Air-Segmented Microfluidic Drop-Based Crystallizer," *Cryst. Growth Des.*, vol. 15, no. 8, pp. 3645–3651, 2015.

[191] R. D. Braatz, "Advanced Control of Crystallization Processes," *Annu. Rev. Control*, vol. 26, pp. 87–99, 2002.

[192] X. Zhao, F. Bian, L. Sun, L. Cai, L. Li, and Y. Zhao, "Microfluidic Generation of Nanomaterials for Biomedical Applications," *Small*, vol. 1901943, pp. 1–19, 2019.

[193] S. Okushima, T. Nisisako, T. Torii, and T. Higuchi, "Controlled production of monodisperse double emulsions by two-step droplet breakup in microfluidic devices," *Langmuir*, vol. 20, no. 23, pp. 9905–9908, 2004.

[194] H. Tavana *et al.*, "Nanolitre liquid patterning in aqueous environments for spatially defined reagent delivery to mammalian cells," *Nat. Mater.*, vol. 8, no. 9, pp. 736–741, 2009.

[195] S. S. Datta *et al.*, "25th anniversary article: Double emulsion templated solid microcapsules: Mechanics and controlled release," *Adv. Mater.*, vol. 26, no. 14, pp. 2205–2218, 2014.

[196] J. Yan, W. A. C. Bauer, M. Fischlechner, F. Hollfelder, C. F. Kaminski, and W. T. S. Huck, "Monodisperse water-in-oil-in-water (W/O/W) Double emulsion droplets as uniform compartments for high-throughput analysis via flow cytometry," *Micromachines*, vol. 4, no. 4, pp. 402–413, 2013.

[197] S. S. Lee, A. Abbaspourrad, and S. H. Kim, "Nonspherical double emulsions with multiple distinct cores enveloped by ultrathin shells," *ACS Appl. Mater. Interfaces*, vol. 6, no. 2, pp. 1294–1300, 2014.

[198] S. H. Kim and D. A. Weitz, "One-step emulsification of multiple concentric shells with capillary microfluidic devices," *Angew. Chemie - Int. Ed.*, vol. 50, no. 37, pp. 8731–8734, 2011.

[199] M. L. Eggersdorfer *et al.*, "Tandem emulsification for high-throughput production of double emulsions," *Lab Chip*, vol. 17, no. 5, pp. 936–942, 2017.

[200] A. Y. N. Hui, G. Wang, B. Lin, and W. T. Chan, "Microwave plasma treatment of polymer surface for irreversible sealing of microfluidic devices," *Lab Chip*, vol. 5, no. 10, pp. 1173–1177, 2005.

[201] L. Yu, C. M. Li, Y. Liu, J. Gao, W. Wang, and Y. Gan, "Flow-through functionalized PDMS microfluidic channels with dextran derivative for ELISAs," *Lab Chip*, vol. 9, no. 9, pp. 1243–1247, 2009.

[202] H. Lamba, K. Sathish, and L. Sabikhi, "Double Emulsions: Emerging Delivery System for

Plant Bioactives," *Food Bioprocess Technol.*, vol. 8, no. 4, pp. 709–728, 2015.

[203] A. C. Jen, M. C. Wake, and A. G. Mikos, "Review: Hydrogels for cell immobilization," *Biotechnol. Bioeng.*, vol. 50, no. 4, pp. 357–364, 1996.

[204] H. Walter and D. E. Brooks, "Phase separation in cytoplasm, due to macromolecular crowding, is the basis for microcompartmentation," *FEBS Lett.*, vol. 361, no. 2–3, pp. 135–139, 1995.

[205] C. D. Keating, "Aqueous phase separation as a possible route to compartmentalization of biological molecules," *Acc. Chem. Res.*, vol. 45, no. 12, pp. 2114–2124, 2012.

[206] Y. Song *et al.*, "Fabrication of fibrillosomes from droplets stabilized by protein nanofibrils at all-aqueous interfaces," *Nat. Commun.*, vol. 7, pp. 1–8, 2016.

[207] Y. H. Lee, M. Y. Bai, and D. R. Chen, "Multidrug encapsulation by coaxial tri-capillary electrospray," *Colloids Surfaces B Biointerfaces*, vol. 82, no. 1, pp. 104–110, 2011.

[208] S. P. Damodaran *et al.*, "A millifluidic study of cell-to-cell heterogeneity in growth-rate and cell-division capability in populations of isogenic cells of Chlamydomonas reinhardtii," *PLoS One*, vol. 10, no. 3, pp. 1–28, 2015.

[209] D. Ferraro *et al.*, "Controlling the distance of highly confined droplets in a capillary by interfacial tension for merging on-demand," *Lab Chip*, vol. 19, no. 1, pp. 136–146, 2019.

[210] A. R. Abate and D. A. Weitz, "Faster multiple emulsification with drop splitting," *Lab Chip*, vol. 11, no. 11, pp. 1911–1915, 2011.

[211] Z. Z. Chong, S. H. Tan, A. M. Gañán-Calvo, S. B. Tor, N. H. Loh, and N. T. Nguyen, "Active droplet generation in microfluidics," *Lab Chip*, vol. 16, no. 1, pp. 35–58, 2016.

[212] Y. N. Cheung and H. Qiu, "Characterization of acoustic droplet formation in a microfluidic flow-focusing device," *Phys. Rev. E - Stat. Nonlinear, Soft Matter Phys.*, vol. 84, no. 6, 2011.

[213] L. Schmid and T. Franke, "SAW-controlled drop size for flow focusing," *Lab Chip*, vol. 13, no. 9, p. 1691, 2013.

[214] C. T. Chen and G. B. Lee, "Formation of microdroplets in liquids utilizing active pneumatic choppers on a microfluidic chip," *J. Microelectromechanical Syst.*, vol. 15, no. 6, pp. 1492–1498, 2006.

[215] S. K. Hsiung, C. T. Chen, and G. Bin Lee, "Micro-droplet formation utilizing microfluidic flow focusing and controllable moving-wall chopping techniques," *J. Micromechanics Microengineering*, vol. 16, no. 11, pp. 2403–2410, 2006.

[216] C. Y. Lee, Y. H. Lin, and G. Bin Lee, "A droplet-based microfluidic system capable of droplet formation and manipulation," *Microfluid. Nanofluidics*, vol. 6, no. 5, pp. 599–610, 2009.

[217] J. H. Wang and G. Bin Lee, "Formation of Tunable, Emulsion Micro-Droplets Utilizing Flow-Focusing Channels and a Normally-Closed Micro-Valve," *Micromachines*, vol. 4, no. 3, pp. 306–320, 2013.

[218] A. R. Abate, M. B. Romanowsky, J. J. Agresti, and D. A. Weitz, “Valve-based flow focusing for drop formation,” *Appl. Phys. Lett.*, vol. 94, no. 2, pp. 92–95, 2009.

[219] J. R. Taylor, *An Introduction to Error Analysis: The Study of Uncertainties in Physical Measurements*. University Science Books, 1997.